THE PHOTOPHYSICS AND SURFACE CHEMISTRY OF TRAPPED NANOPARTICLE IONS AS STUDIED BY ION TRAP NANOPARTICLE MASS SPECTROMETRY

by

Collin R. Howder

A dissertation submitted to the faculty of
The University of Utah
in partial fulfillment of the requirements for the degree of

Doctor of Philosophy

Department of Chemistry

The University of Utah

August 2016

The University of Utah Graduate School

STATEMENT OF DISSERTATION APPROVAL

The dissertation of **Collin R. Howder**

has been approved by the following supervisory committee members:

Scott L. Anderson	, Chair	**8/8/2015** Date Approved
Peter B. Armentrout	, Member	**8/11/2015** Date Approved
Michael David Morse	, Member	**8/10/2015** Date Approved
Marc D. Porter	, Member	**8/10/2015** Date Approved
Clayton C. Williams	, Member	**8/10/2015** Date Approved

and by **Cynthia Burrows**, Chair of

the Department of **Chemistry**

and by David B. Kieda, Dean of The Graduate School.

ABSTRACT

Ion tap nanoparticle mass spectrometry (NPMS) is employed to study the photophysics and surface chemistry of trapped nanoparticle ions. The ion trap instrument and the approaches to measure the mass, charge, and emission spectrum of trapped nanoparticles is discussed. The photophysics and thermal properties of trapped semiconductor nanocrystal 'quantum dot' ions is also discussed, as well as their suitability for use as noncontact fluorescence probes in the gas phase. Finally, a method to study the surface chemistry of nanoparticles at temperatures in excess of 2000^{o}C is described and a proof of principle example is provided.

TABLE OF CONTENTS

LIST OF FIGURES

ACKNOWLEDGEMENTS

I would like to thank Scott Anderson for serving as my advisor and mentor during my time at the University of Utah, and for all the knowledge and experience he has shared as well as the patience, kindness, and encouragement he has extended to me. I would also like to thank Peter Armentrout for the opportunity to work under him during the summer of 2007. It was this experience that inspired me to pursue a doctorate in chemistry and to attend the University of Utah.

I also wish to extend my thanks to the other members of the Anderson group, past and present, who have made this a wonderful place to work and study. I wish to specifically thank David Bell and Bryan Long, with whom I worked closely, for their guidance, encouragement, and friendship.

I also wish to thank the members of the Chemistry department's electronics and machine shops, specifically Dale Heisler, Tom Gudmundson, and Dennis Romney. Without their expertise and helpful discussions this work would not have been possible.

Finally, I wish to thank my many friends and my family for their love and support.

CHAPTER 1

INTRODUCTION

1.1 Introduction to Nanoparticle Mass Spectrometry

Mass spectrometry is incredibly useful for any scientist hoping to gain insight into the molecular world. As the interest in all things nanoscale has increased over the past few decades, it is not surprising that interest in nanoparticle mass spectrometry (NPMS) has increased as well. As the name of the technique would suggest, the goal of NPMS is to study the properties of nanoparticles (NPs) using the tools of mass spectrometry. However, most mass spectrometry methods were initially developed to study atoms and small molecules, and some are simply not useful for studying a system with too much mass, NPs included. For example, the resolution of a quadrupole mass filter is too low to distinguish between two NPs of similar mass.

Ion traps are often used as a platform for NPMS. Ion traps use electric fields to confine a particle in either two or three dimensions and are particularly attractive because anything from atoms up to micron sized particles can be confined, depending on the trapping conditions. Many types of ion traps exist, and several have been used for NPMS. Perhaps the simplest type of ion trap is the electrodynamic balance, which consists of a conductive ring, or ring electrode, with small metal plates above and below the ring opening called end cap electrodes. An AC waveform is applied to the ring, creating a quadrupolar electric field. The potential created by the ring is zero at the trap center, but increases quadratically in all directions away from the trap center. This potential exerts a force toward the trap center on any charged particle. If the AC frequency and amplitude are in the right range a charged particle will be levitated near the trap center. This quadrupole ion trap is often referred to as a Paul trap after Wolfgang Paul whose work laid the foundations for the technology.

If there is no voltage gradient between the end cap electrodes then the trapped particle will sit just below the trap center, where the centering trapping force is in balance with the force of gravity. By applying a potential to one of the end caps, the particle can be raised back into the trap center. Measuring this voltage allows the particle's mass-to-charge-ratio (*M/Q*) to be measured. While this technique has the advantage of being very simple, the primary disadvantage is the relatively low mass resolution of a few percent.

A more sophisticated and precise way of measuring the *M/Q* of particles was developed by Wuerker et al. in 1959.[1] In their work, a single aluminum microparticle is confined in a Paul trap and *M/Q* is measured by measuring the motional, or secular frequency along one of the principal trap dimensions, either in the axial (z) or radial (r) directions. The secular frequency along the trap axis relates to *M/Q* as follows:

$$\frac{M}{Q} = \frac{\sqrt{2}V_0}{\omega_z \Omega z_0^2} \tag{1.1}$$

Here, ω_z ($\omega_z / 2\pi = f_z$) is the secular frequency along the trap axis, V_0 and Ω ($\Omega / 2\pi = F$) are the trapping field amplitude and frequency, respectively, and z_0 is a trap geometric parameter. Trapped particles were illuminated by a carbon arc and were detected by eye. ω_z was measured by applying a weak alternating current drive potential near the trap center. The drive frequency (ω_{drive}) was varied until $\omega_{drive} = \omega_z$ which visibly increases the secular amplitude of the trapped particle.

1.2 Approaches to Nanoparticle Mass Spectrometry

Today, there are a variety of trap types and detection schemes in ion trap NPMS. The next significant advance in NPMS did not occur until 1995, when Hars illuminated

trapped NPs with a laser and detecting scattered photons with a CCD. ω_z was determined by tuning Ω and watching the trajectory of the trapped ions. When ω_z is an integer multiple of Ω the NP trajectory becomes a standing star shaped pattern with Ω / ω_z nodes. This method improved the precision of the NPMS method to ~1000 ppm.

Further advances have been made by Gerlich and Schlemmer, who designed a modified Paul trap where the ring electrode is split to allow for increased optical access. In such a trap they used a Fourier transform approach to measure ω_z of a trapped NP to ~ 100 ppm.[2] By repeatedly measuring ω_z for many days they observed places where ω_z stepped due to events that changed the NP change by ±e. By measuring the step height the absolute *Q* could be calculated and *M* could be measured. This approach was used to measure the rates of gas adsorption and desorption on a single isolated NP.[3] Similar work has been reported by Boo,[4] Ruhl,[5-7] Abbas,[8-10] and Bieske.[11-14]

Another scheme was developed by H.C. Chang and coworkers,[15] who use a ring electrode trap to confine NPs, then sweep a large amplitude AC drive. When $\omega_{drive} = \omega_z$ a NP is ejected onto a charge detection plate. The frequency of ejection gives *M/Q* and the charge detector measures *Q,* giving M. Charge detectors of this type cannot detect a particle unless *Q* is sufficiently large, ~1000 e or more, and even then they are only precise to about a tenth of one percent. Similar charge detection schemes are currently in use by Antoine[16] and Jarrold.[17]

Charge detection is convenient, but to date, all charge detection methods are destructive, meaning that measuring *M/Q* destroys the particle. Optical detection schemes have been used to measure *M* and *Q* repeatedly over many days. However, to date, optical detection requires that a trapped NP is large enough to scatter a measurable

amount of light (~50 nm or larger), or is fluorescent. Presented in this dissertation (Chapter 5) is a method that extends the optical detection approach to small, nonemissive, or dark NPs using semiconductor nanocrystals as non contact fluorescence probes. Our NPMS instrument and trapping techniques are discussed in Chapter 2. Chapter 3 explores our methods for measuring *M* and *Q* of trapped NPs, including both small (5-10 nm) and large (100 – 200 nm) particles. Chapter 4 focuses on the photophysical properties of trapped semiconductor nanocrystal ions, which we employ as fluorescence probes in Chapter 5. Chapter 6 focuses on a new direction for NPMS: the use of an ion trap as a platform for ultra-high temperature surface chemistry of nanoparticles.

1.3 References

1. R. F. Wuerker, H. H. Shelton and R. V. Langmuir, J. Appl. Phys. **30** (3), 342-350 (1959).
2. S. Schlemmer, J. Illemann, S. Wellert, and D. Gerlich, J. Appl. Phys. **90** (10), 5410-5418 (2001).
3. S. Schlemmer, J. Illemann, S. Wellert and D. Gerlich, AIP Conf. Proc. **457** (Trapped Charged Particles and Fundamental Physics), 80-86 (1999).
4. S. C. Seo, S. K. Hong, and D. W. Boo, Bull. Korean Chem. Soc. **24**, 552-554 (2003).
5. C. Graf, R. Lewinski, S. Dembski, B. Langer, and E. Ruehl, Phys. Status Solidi C **4** (9), 3244-3259 (2007).
6. M. Grimm, B. Langer, S. Schlemmer, T. Lischke, U. Becker, W. Widdra, D. Gerlich, R. Flesch, and E. Ruehl, Phys. Rev. Lett. **96** (6), 066801/066801-066801/066804 (2006).
7. C. Graf, B. Langer, M. Grimm, R. Lewinski, M. Grom, and E. Ruehl, J. Electron Spectrosc. Relat. Phenom. **166-167**, 74-80 (2008).

8. M. M. Abbas, D. Tankosic, P. D. Craven, J. F. Spann, and A. LeClair, Astrophys. J. **645**, 324 - 336 (2006).

9. M. M. Abbas, D. Tankosic, P. D. Craven, R. B. Hoover, L. A. Taylor, J. F. Spann, A. LeClair, and E. A. West, European Space Agency Special Report **SP-643** (Dust in Planetary Systems), 165-170 (2007).

10. M. M. Abbas, D. Tankosic, J. F. Spann, M. J. Dube, and J. A. Gaskin, AIP Conference Proceedings **969**, 942-948 (2008).

11. A. J. Trevitt, P. J. Wearne, and E. J. Bieske, Int. J. Mass Spectrom. **262** (3), 241-246 (2007).

12. A. J. Trevitt, P. J. Wearne, E. J. Bieske, and M. D. Schuder, Opt. Lett. **31** (14), 2211-2213 (2006).

13. T. A. Smith, A. J. Trevitt, P. J. Wearne, E. J. Bieske, L. J. McKimmie, and D. K. Bird, Springer Ser. Fluoresc. **4** (Fluorescence of Supermolecules, Polymers, and Nanosystems), 415-429 (2008).

14. A. J. Trevitt, P. J. Wearne, and E. J. Bieske, J. Aerosol Sci. **40** (5), 431-438 (2009).

15. W.-P. Peng, H.-C. Lin, M.-L. Chu, H.-C. Chang, H.-H. Lin, A. L. Yu, and C.-H. Chen, Anal. Chem. **80**, 2524-2530 (2008).

16. T. Doussineau, P. Dugourd, and R. Antoine, Spectrosc. Eur. **24** (4), 16-20 (2012).

17. N. C. Contino, E. E. Pierson, D. Z. Keifer, and M. F. Jarrold, J. Am. Soc. Mass Spectrom. **24**, 101-108 (2013).

CHAPTER 2

NANOPARTICLE MASS SPECTROMETRY APPROACH AND INSTRUMENT

2.1 Introduction

Instruments based on three-dimensional quadrupole (Paul) traps have been used by several groups for nondestructive, optically-detected mass measurements on single nano- and micro-particles.[1-12] One limitation of these instruments was the use of particle injection methods such as dropping,[10] throwing, [4, 5, 8, 9] or laser desorbing particles from probes inserted next to the trap.[2, 11] These injection methods were successful for the problems of interest, but they do not lend themselves to reliable, repeatable, and convenient injection of single particles with control over the range of mass and charge.

We describe a NPMS instrument of this type, in which the quadrupole particle trap is fed by an electrospray ionization (ESI) nanoparticle source via a pair of radio-frequency ion guides. The ion guides provide collisional cooling and focusing of the nanoparticle beam from the source, and also act as prefilters, eliminating species outside the desired range of mass-to-charge (*M/Q*) ratios. The design makes it possible to inject and trap single nanoparticles on demand, thereby substantially increasing the experimental efficiency, and allowing for more complex experiments where, for example, a second particle is injected into the trap to create a trapped particle pair. The ESI source appears to be quite broadly applicable to nanoparticles. We discuss ESI and trapping of particles such as polymer spheres and ligand-capped semiconductor nanocrystals (quantum dots), which are water-soluble, and therefore expected to be compatible with electrospray. We also discuss trapping bare metal, graphite, and metal oxide-coated particles with no solubilizing ligands, where it is not obvious that ESI should work.

The coupling of NPMS to a convenient, flexible, and reliable nanoparticle source has the potential to turn NPMS into a useful, routine analytic tool, with potential

applications to high-precision mass analysis of particles ranging from viruses to quantum dots (QDs). In addition, because particle detection is nondestructive, NPMS lends itself to studies of the kinetics of surface adsorption,[8, 9] reactions, and sublimation, and to studies of how optical properties change as chemical properties are varied. This chapter focuses on coupling an ESI source to the NPMS particle trap and gives parameters suitable for spraying and trapping a wide range of particle types and sizes, ranging from 200 kiloDalton (kDa) (~5 nm) to >3 GDa (>200 nm).

2.2 The Nanoparticle Mass Spectrometry Method

The NPMS technique uses a 3D quadrupole (Paul) trap driven by two sinusoidal radio-frequency (RF) voltages of opposite phase, with amplitude V_0 and angular frequency Ω, with one phase applied to the ring electrode and the other to the pair of end cap electrodes. In our instrument, the RF voltages are generated by one of three generators. The first is a home-made bipolar RF generator, similar to ones described previously.[13] For nanoparticle operation, we modified the original design in two ways. The original tetrode tubes were replaced with high-voltage triodes (811A), allowing operation at V_0 up to 1.2 kV, and coil and load capacitors were adjusted to give operating frequencies in the 100 to 1000 kHz range. This 'tube amp' generator is suitable for experiments with NPs with $M/Q < 10^6$ Da / e, provided the Ω does not need to be changed during an experiment. However, there are times when Ω must be changed during an experiment, such as when the charge of a trapped NP changes by a large amount. It is also convenient to have a readily tunable source for the purposes of optimizing trapping conditions. To meet these challenges, we have designed a tunable solid state linear RF

amplifier, which uses two high voltage operational amplifiers which are tunable from the 1 to 1000 kHz range with a maximum V_0 = 200 V. The amplifier requires an external frequency source, for which we use a digital function generator (Agilent 33220A). In addition, we have another generator (~0.1 to ~40 kHz), which uses transformers to convert the output of an audio frequency generator into the kV range. This 'transformer' generator is tunable over a range of ~ 10 kHz when powered on, but components, in this case, toroidal inductors, must be switched in and out to access a different frequency range.

The physics of ion (and particle) motion in inhomogeneous AC fields has been discussed by a number of authors[14,15] and the brief description here follows that given by Schlemmer and Gerlich.[8, 16] Under appropriate conditions, the motion of a charged particle in such a trap consists of slow, large amplitude secular motion, with superimposed micro-motion at frequency Ω. The secular motion can be described as motion in the time independent effective potentials:

$$V_{eff\_z}(z) = \frac{(Q \cdot V_0)^2}{M \cdot \Omega^2 \cdot z_0^2}\left(\frac{z}{z_0}\right)^2 \tag{2.1}$$

$$V_{eff\_r}(r) = \frac{(Q \cdot V_0)^2}{M \cdot \Omega^2 \cdot r_0^2}\left(\frac{r}{r_0}\right)^2 \tag{2.2}$$

for motion in the axial and radial directions, respectively. Here, *M* and *Q* are the particle mass and charge, and z_0 and r_0 are characteristic axial and radial trap dimensions (2.96 mm and 5.92 mm, respectively, for our trap). Because both axial and radial effective potentials are quadratic from the trap center, the secular motion is harmonic with secular frequencies that are proportional to Q/M. In the following equation, we will focus on

measurements of the secular frequency for motion in the axial direction, ω_z, which is related to *M* and *Q* as follows:

$$\frac{M}{Q} = \frac{\sqrt{2}V_0}{\omega_z \Omega z_0^2} \tag{2.3}$$

Therefore, measurement of ω_z gives *M/Q* and *M*, provided that *Q* is known. As shown below, the exact value of *Q* is determined by observing the quantized steps in ω_z that occur when the particle gains or loses an electron due to collisions with background electrons or ions.

A number of methods have been demonstrated for measuring secular frequencies, all involving use of a laser to illuminate the particle, allowing some signature of the secular motion to be recorded optically. Several groups have used imaging of Lissajous orbits to obtain the ratio of the secular frequency to the RF drive frequency, Ω.[6, 8, 11, 17] Schlemmer and Gerlich[8, 16] recorded fluctuations in light scattering signal caused by secular motion of single particles relative to the focused detection laser, and Fourier transformed the I(t) record to obtain the secular frequency to precision of ~100 ppm in a single experiment, improved to ~10 ppm by averaging measurements for an hour. We have experimented[1] with several approaches for measuring including ω_z, which are discussed below.

2.3 The NPMS Instrument

A cross section through the instrument is shown in Figure 2.1. The entire instrument is mounted on a pneumatically isolated laser table, which is surrounded by a light-tight acoustic enclosure to minimize vibrational perturbations. All pumps are

isolated from the chamber by bellows sections, and the fore-lines, as well as all electrical cables and gas lines, pass through optically opaque baffles.

The ESI source, hexapole guide, and quadrupole guide were all taken from an old triple quadrupole mass spectrometer (Micromass, now Waters, Quattro II). The ESI source, a commercial "Z-spray" source, mates directly to the hexapole guide, which collects nanoparticles from the source. The linear quadrupole guide was originally one of the mass-selecting quadrupoles from the old instrument and has been fitted into a new housing. The source operates at atmospheric pressure and is differentially pumped by a large mechanical pump. The vacuum system consists of a chamber which houses the hexapole guide, pumped by a 300 l/s turbomolecular pump, and a trap chamber, also pumped by a 300 l/s turbomolecular pump. To minimize contamination of the trap chamber and its components by the large flow of gases from the ESI source, the instrument includes an isolation valve between the hexapole and quadrupole guides. The valve assembly consists of a thin sliding plate that seals to an o-ring surrounding the aperture in the differential pumping wall which separates the hexapole and trap chambers. Because this differential wall and the valve assembly are isolated from ground, they serve as an electrostatic lens to focus particles from the hexapole guide into the quadrupole guide. The valve is pneumatically operated so that it can be opened briefly to allow particle injection, and then closed to protect the trap chamber vacuum (10^{-8} Torr, unbaked). After passing through the isolation valve, particles are guided by the linear quadrupole up to the trap entrance, where they can be injected for NPMS experiments.

Figure 2.2 shows a cross section through the particle trap in more detail. The trap

is based on a design reported by Gerlich and Decker[18] in which the ring electrode is split into two sections so as to allow optical access to the trap center around the equator of the trap. The "end cap" electrodes are truncated cones with relatively large holes allowing optical detection, or as in our instrument, injection and extraction of nanoparticles. Obviously, the electrode surfaces in this trap are far from the ideal hyperbolic geometry, however, the geometry is such that the fields are near-ideal in a small volume near the trap center. The key to high precision mass determination in NPMS is, therefore, to measure the secular frequency for small amplitude motion.

Detection of both the particle and its secular frequency is done optically. Particles with diameters greater than ~100 nm are easily detected by light scattering, and smaller particles can be detected by laser-induced fluorescence (LIF) or thermal emission if they are heated. Because detection is nondestructive, signal from a single particle can be averaged to improve sensitivity. In addition, because single particles can be studied for days if desired, it is possible to monitor changes in particle mass and charge as the particle is heated or reacted with gaseous reactants, allowing studies of surface reaction kinetics or of the effects of heating or chemical state on optical properties.

Our trap is modified by the addition of two pairs of channels cut through the end cap electrode support flanges (i.e., not affecting the trapping fields) to allow lasers to be passed through the trap center along the indicated diagonals. The trap is mounted inside a Thorlabs "cube," also modified to allow diagonal laser passage. The cube provides convenient coaxial mounting surfaces for the trap and associated ion lens assemblies in addition to four orthogonal ports along the trap equator which are threaded to take standard optics mounts. In the experiments described below, one diagonal channel is

used to focus a quasi-continuous wave (CW) CO_2 laser through the trap for particle heating via a pair of confocal off-axis paraboloidal mirrors. The other diagonal path is unused. This laser (Synrad, 10 W) can be run CW or the average power can be varied by modulating the duty cycle. We typically modulate the laser at 30 kHz - well above the normal 5 kHz modulation frequency - in order to obtain a quasi-CW beam. For particle detection, a CW visible laser (532 nm, $\leq$ 500 mW, or 405 nm, $\leq$ 5 W) is focused through the trap horizontally (into the plane of the figure). The optical ports on top and bottom are used for light detection by an avalanche photodiode module (Laser Components COUNT) and an inexpensive CCD camera designed for use on amateur telescopes. The visible laser is typically run between 300 – 500 mW power when detecting particles by light scattering and 100 – 200 mW when detecting by laser induced fluorescence.

A typical experiment might consist of electrospraying a dilute nanoparticle solution of interest, using the hexapole guide for differential pumping/desolvation. Most of our work to date has been with positively charged particles, but the source can be run in negative mode as well. In initial experiments, we would typically trap an ensemble of particles and then selectively eject particles until only one remained.[1] With experience, it is much easier to simply gate a single particle into the trap by manually opening the isolation valve for ~1s. It is easy to tell if there is only one particle and, if there are more than one, the trap is simply dumped and filled again. In some experiments, the CO_2 laser is left on at low-to-medium duty cycle to heat the particles as they enter the trap to ensure complete desolvation, and in some cases desorption of ligands on the particle surface.

Gating the ion beam with the isolation valve is convenient for long, single particle experiments. If higher throughput is desired, it would be possible to accumulate ions in

the quadrupole prefilter, blocking them from entering the trap by potentials applied to a lens electrode at the end of the quadrupole. The trap could be filled with either small ensembles of particles or a single particle by gating the lens electrode for appropriate length of time.

2.4 Prefiltering the *M/Q* Distribution

Because the ESI source produces a high current of atomic and molecular ions, as well as particles and particle aggregates with a broad range of *M/Q*, it is useful to pre-filter the particle beam to narrow the range of *M/Q* before attempting single particle injection. For any given frequency and voltage only particles in a range of *M/Q* will be guided by the guides and trapped by the trap. As discussed by Gerlich,[16] inhomogeneous AC fields trap ions/particles with a limited range of *M/Q*. The upper limit is given by the strength of the effective potential confining the particles. For both the quadrupole trap and linear quadrupole guide, the effective potential has the form given above (only V_{eff_r} is relevant for the linear guide). V_{eff_r} for the hexapole guide is similar, but with $(r/r_0)^4$ radial dependence. Because the effective potentials vary like Q^2/M, there is a high *M/Q* limit above which particles are no longer efficiently guided. The low *M/Q* limit is set by the requirement that the RF-driven micro-motion of the particles must remain out of phase with the driving force, otherwise they gain kinetic energy from the RF field and are rapidly ejected. Gerlich[16] has suggested that the adiabaticity parameter, $\eta \left(= \frac{4QV_{RF}}{Mz_0^2\Omega^2}\right)$ should be less than 0.3 for stable confinement, which defines the low *M/Q* limit for guiding or trapping. In our instrument, the r_0 geometric parameters of the guides and trap are similar, thus for given operating conditions, they tend to select the same range of

M/Q. This makes it possible to use a single RF generator to drive all three.

2.5 Electrospray and Trapping Conditions for Different Particle Types

To date, we have trapped several different kinds of particles: polystyrene and silica spheres (and large aggregates of these spheres), ligand-capped CdSe/ZnS core shell nanocrystals (quantum dots), silica-encapsulated quantum dots, bare graphite, and bare tungsten carbide nanoparticles. The polystyrene spheres (25 nm), silica spheres (80 and 200 nm), and ligand coated quantum dots (5 nm core, 1 nm shell) are highly dispersible in aqueous solutions, and thus good candidates for ESI. Indeed, Kawazoe[19] and Pease[20] have previously reported ESI of quantum dot solutions, although not for trapping or high-precision mass spectrometry. The silica-encapsulated quantum dots were synthesized at Los Alamos National Lab and are also dispersible in water. The graphite and tungsten carbide nanoparticles, however, were uncoated and therefore not compatible with typical ESI solvent combinations, i.e., they were not expected to electrospray well.

The parameters used to spray and trap are summarized in Table 2.1. The important parameters include the trap RF frequency (Ω) and voltage (V_0), the RF frequency, and voltage applied to the hexapole and quadrupole guides, the ESI solution and capillary voltage, and the pressure in the trap region. As particles are injected into the trap, they must be accelerated enough to pass over the effective potential barrier created by the RF potential on the end cap electrode, and they must lose some of this kinetic energy in order to become trapped. To aid trapping, the vacuum chamber housing the trap is filled with argon buffer gas to a pressure (P_{trap}) in the 10 to 30 mTorr range. In principle, trapping could be enhanced by biasing the lens electrodes on the far side of the

trap to reflect particles that would otherwise simply fly straight through, however, we find trapping to be quite efficient without such potentials. The pressure in the hexapole guide is mostly determined by the balance between gas flow from the ESI source and the 300 l/s pumping speed on the chamber, and is typically 10 – 13 mTorr. The linear quadrupole has no independent pumping, and therefore its pressure is presumably roughly the average of the pressures in the trap and hexapole chambers.

Most of the particles we have experimented with are water soluble and obtained in the form of aqueous stock solutions. For single particle experiments, we want a rather low-intensity particle beam, and because water is relatively viscous and has a high boiling point, we dilute the aqueous stock solutions in methanol before electrospraying. Polystyrene spheres (25 nm) were obtained from Invirtogen as 2 mM sodium azide solutions containing 2% nanoparticles by mass. The stock solution was diluted 10:1 in methanol and sprayed at 3.5 kV capillary voltage. Under these conditions, a wide range of particle sizes is electrosprayed, ranging from single 25 nm particles to large aggregates which are either present in the ESI solution, or formed during the ESI process. As the table shows, we experimented with varying the RF frequency driving the trap and guides, and also the trap pressure, to select different *M/Q* ranges from the distribution. For example, with both trap and guide running at 143.3 kHz, and 400 – 600 V amplitude, use of P_{trap} in the 10 - 20 mTorr range resulted in trapping of aggregates with *M/Q* in the 150 to 300 kDa/e range, and thousands of charges/aggregate. If P_{trap} is between 20 and 30 mTorr, then aggregates are trapped with higher *M/Q*, with masses ranging up to 3.6 GDa in the 250 to 1500 kDa/e range, presumably because these require more momentum transfer to be become trapped. If the guides and trap are run at higher frequency (280

kHz), this optimizes guiding and trapping conditions for particles with smaller *M/Q*, ranging from 65 to 80 kDa/e.

As a demonstration of the effect of prefiltering, the table also summarizes an experiment where the trap and guides were run at very different frequencies, 13 kHz via the transformer generator and 143.3 kHz via the tube amp generator, respectively. The 13 kHz frequency used for the trap is optimal for trapping particles with low *M/Q* values in the 1000 – 10 000 kDa/e range. The guides were kept at 143.3 kHz (*M/Q* = 150 to 1500 kDa/e), i.e., there is little overlap between the *M/Q* distribution prefiltered by the guides, and the range of *M/Q* the trap is able to trap. As expected, therefore, under these conditions, trapping was very inefficient, and resulted in only occasional injection of particles with large *M/Q*.

Our tunable solid-state RF amplifier does not have a sufficient output power to drive the guides and the trap simultaneously. In an attempt to trap high *M/Q* NPs we modified our tube amp generator to operate at 104 kHz, with which we drove the guides, and used the tunable solid-state amplifier to drive the trap. Using both silica and polystyrene NPs whose stock diameters ranged from 80 – 200 nm, we were able to trap with V_0 = 200 V with Ω ranging from 20 – 50 kHz. *M/Q* for the trapped ions ranged from 30 to 1000 kDa / e. Both types of NPs were obtained at 1 mg/ml concentration and were diluted ~ 10:1 in methanol and sprayed with a capillary voltage of 3 kV.

Water-soluble mercaptoundecenoic acid-capped CdSe/ZnS quantum dots were obtained as stock solutions with 1 mg/ml concentration in aqueous solutions (NN Labs). These stock solutions were diluted 100:1 in methanol, and electrosprayed at 3.5 kV capillary voltage. For trapping and guiding frequency of 143.3 kHz, we are able to trap

both single quantum dots $M \approx 400$ kDa, $M/Q = 50$ to 100 kDa/e, and small aggregates containing a few QDs with similar M/Q. At 280 kHz, we observe mostly single QDs, with few aggregates.

Quantum dots capped with ligands that render them hydrophobic are available commercially with a wider range of sizes, composition, and other properties, but hydrophobic materials are generally more difficult to electrospray. As a test, quantum dots in toluene solution (NN labs, ~7 nm) were successfully electrosprayed and trapped by diluting the toluene solution 100:1 in acetonitrile (ACN) with 2% formic acid added to provide a source of charge. Using ESI and trapping conditions identical to those used for the aqueous quantum dot solutions, we were easily able to trap and detect the hydrophobic quantum dots.

Silica-coated quantum dots, without any stabilizing ligands, were obtained from Los Alamos National Laboratory, as 1 mg/ml in aqueous solution. The stock solution was diluted 100:1 in methanol, electrosprayed, trapped, and detected by light scattering, again, under the same conditions.

To prepare a sample of graphite NPs for ESI, a few milligrams of the graphite powder were suspended in methanol by ultrasonication. The resulting suspension is stable for a few days. Graphite particles could not be trapped from the methanol suspension, presumably due to the absence of ions in the solution that would act as charge carriers in ESI. The suspension was diluted by a factor of three in an ammonium acetate in methanol solution, resulting in a final ammonium acetate concentration of ~50 μM. The guides were set to 104 kHz with an amplitude of 300 V, and the trap was driven at $\Omega = 60$ kHz and $V_0 = 200$ V, with the argon pressure in the trap chamber set to 15 mTorr and the ESI

capillary set to +3 kV. Graphite is very refractory and strongly absorbs in the visible and the IR. This made it possible to heat graphite and detect by thermal photon emission. Graphite NPs in the 100 MDa mass range, consistent with a spherical diameter of ~ 40 nm, have been observed. A discussion of surface chemistry experiments performed on trapped graphite can be found in Chapter 6.

When adding salts for charging by ESI it is important that the concentration be kept below ~ 1 mM. We have found that at this concentration and higher it is possible to generate and trap salt NPs, which in the case of ammonium acetate are only trapped for a few s before they are ejected, presumably because they rapidly lose mass due to sublimation. It is also possible to trap NaCl NPs in the same way, which are stable in the trap.

Finally, we also tested ESI and trapping of tungsten carbide nanoparticles (US Research Nanomaterials, 30-100 nm dry powder). These were simply suspended in methanol by ultrasonication/shaking and electrosprayed as quickly as possible (<5 m from solution preparation) to minimize reprecipitation. Somewhat surprisingly, we were able to trap particles at 143.3 kHz with V_0=600V, and using 30 mTorr of argon. ESI and trapping were relatively inefficient (i.e., the particle flux was low), but this probably reflects the fact that the suspensions were not very stable or concentrated, and that no salt or other ionic compound was added, thus, the only ions available to charge the particles were from contaminants. Nonetheless, for single particle experiments, low, but nonzero intensity particle beams are quite adequate, so it really is not necessary to optimize the ESI source conditions.

While all trapping procedures described above produce positive NP ions, it is

possible to trap negative NPs by switching the voltage of every component in the source and beamline to the opposite polarity. Polystyrene and silica NPs trap very efficiently in negative ion mode. Trapping of other NP types in negative ion mode has not been explored, but is not expected to be significantly different.

2.6 References

1. D. M. Bell, C. R. Howder, D. Gerlich, D. K. Lewis, and S. L. Anderson, Int. J. Mass Spectrom. **(submitted)** (2014).

2. Y. Cai, W. P. Peng and H. C. Chang, Anal. Chem. **75** (8), 1805-1811 (2003).

3. Y. Cai, W. P. Peng, S. J. Kuo, Y. T. Lee, and H. C. Chang, Anal. Chem. **74** (1), 232-238 (2002).

4. C. Graf, R. Lewinski, S. Dembski, B. Langer, and E. Ruehl, Phys. Status Solidi C **4** (9), 3244-3259 (2007).

5. M. Grimm, B. Langer, S. Schlemmer, T. Lischke, U. Becker, W. Widdra, D. Gerlich, R. Flesch, and E. Ruehl, Phys. Rev. Lett. **96** (6), 066801/066801-066801/066804 (2006).

6. G. Hars, and Z. Tass, J. Appl. Phys. **77** (9), 4245-4250 (1995).

7. W. P. Peng, Y. Cai, Y. T. Lee, and H. C. Chang, Int. J. Mass Spectrom. **229** (1-2), 67-76 (2003).

8. S. Schlemmer, J. Illemann, S. Wellert, and D. Gerlich, J. Appl. Phys. **90** (10), 5410-5418 (2001).

9. S. Schlemmer, S. Wellert, F. Windisch, M. Grimm, S. Barth, and D. Gerlich, Appl. Phys. A: Mater. Sci. Process. **78** (5), 629-636 (2004).

10. S. C. Seo, S. K. Hong, and D. W. Boo, Bull. Korean Chem. Soc. **24**, 552-554 (2003).

11. A. J. Trevitt, P. J. Wearne, and E. J. Bieske, Int. J. Mass Spectrom. **262** (3), 241-246 (2007).

12. A. J. Trevitt, P. J. Wearne, E. J. Bieske, and M. D. Schuder, Opt. Lett. **31** (14), 2211-2213 (2006).

13. R. M. Jones, and S. L. Anderson, Review of Scientific Instruments **71**, 4335-4338

(2000).

14. P. H. Dawson, *Quadrupole Mass Spectrometry*. (Elsevier Scientific Pub., Amsterdam, 1976).

15. D. Gerlich, in *Advances in Chemical Physics: State-Selected and State-To-State Ion-Molecule Reaction Dynamics, Part 1*, edited by C. Y. Ng and M. Baer (J. Wiley & Sons, 1992), Vol. 82, pp. 1-176.

16. S. Schlemmer, J. Illemann, S. Wellert, and D. Gerlich, AIP Conf. Proc. **457** (Trapped Charged Particles and Fundamental Physics), 80-86 (1999).

17. R. F. Wuerker, H. H. Shelton, and R. V. Langmuir, J. Appl. Phys. **30** (3), 342-350 (1959).

18. D. Gerlich, and S. Decker, Appl. Phys. B: Lasers Opt. **114**, 257-266 (2014).

19. Y. Tani, S. Kobayashi, and H. Kawazoe, J. Vac. Sci. Technol. A **26** (4), 1058-1061 (2008).

20. L. F. P. III, J. I. Feldblyum, S. H. D. Lacaerda, Y. Liu, A. R. H. Walker, R. Anumolu, P. B. Kim, M. L. Clarke, H. G. Kang, and J. Hwang, ACS Nano **4**, 6982-6988 (2010).

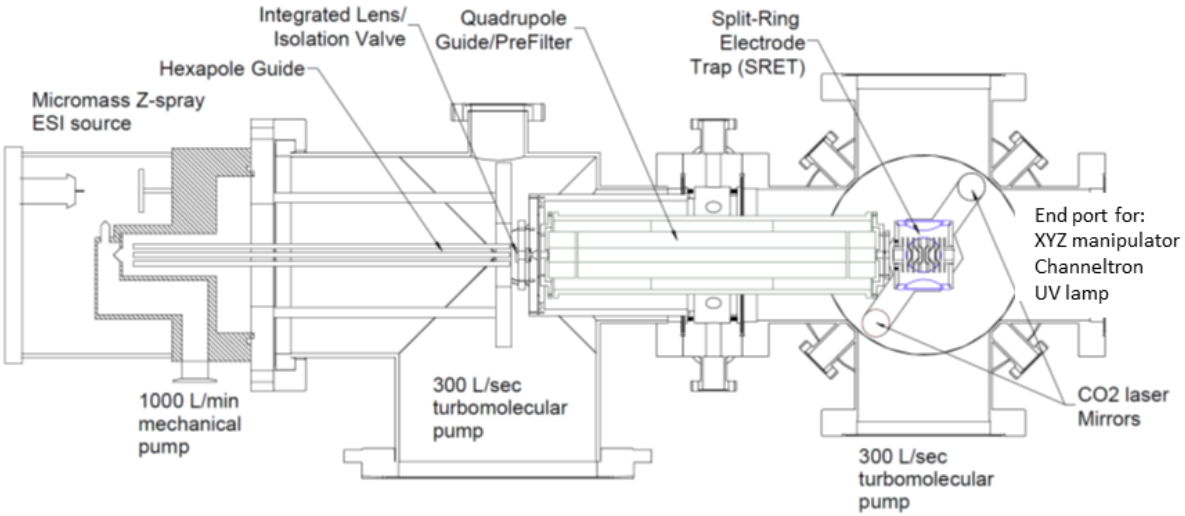

Figure 2.1. NPMS Instrument. Instrument is equipped with ESI source and linear quadrupole guide prefilter. For scale, note that the top and bottom of the trap chamber are capped with CF 100 (6" OD) flanges.

Table 2.1: Trapping conditions for various nanoparticles. All particles were electrosprayed with a capillary voltage =3.5kV and trapped at a pressure between 10 – 30 mTorr. 1) Ligand = Mercaptoundecanoic acid 2) Ligand = Octadecyl amine

Particle	**RF frequency (Ω) /kHz**	**RF voltage (V_0) /V**	**Solution**	**Trap P /mTorr**	***M/Q* /kDa e^{-1}**
Polystyrene (25nm stock)	143.3	400-600	10:1 MeOH	10 - 20	150-300
Polystyrene (25nm stock)	143.3	400-600	10:1 MeOH	20-30	250-1500
Polystyrene (25nm stock)	Guides 143.3 Trap 14	400-600	10:1 MeOH	10-30	65-80
Polystyrene (25nm stock)	Guides 104 Trap 25 – 50	Guides 500 Trap 200	10:1 MeOH	20-30	30 – 1000
Silica (80 – 200nm stock)	Guides 104 Trap 25 - 50	Guides 500 Trap 200	10:1 MeOH	20-30	30 – 1000
Quantum dots (5-10nm, MUA[1], H_2O)	143.3, 280	400-600	100:1 MeOH	10-30	50-100
Quantum dots (5-10nm, ODA[2], Toluene)	143.3	400-600	100:1 MeOH	10-30	50-100
Quantum Dots (5-10nm, silica coated, H_2O)	143.3	400-600	100:1 MeOH	10-30	-
Graphite (~40nm)	Guides 104 Trap 60	Guides 300 Trap 200	50 μM ammonium acetate	15	~2000
NaCl	Guides 104 Trap 60 - 25	Guides 300 Trap 200	1 – 1000 mM NaCl/ MeOH	10-30	-
Tungsten Carbide (30-100nm)	143.3	400-600	100:1 MeOH	20-30	-

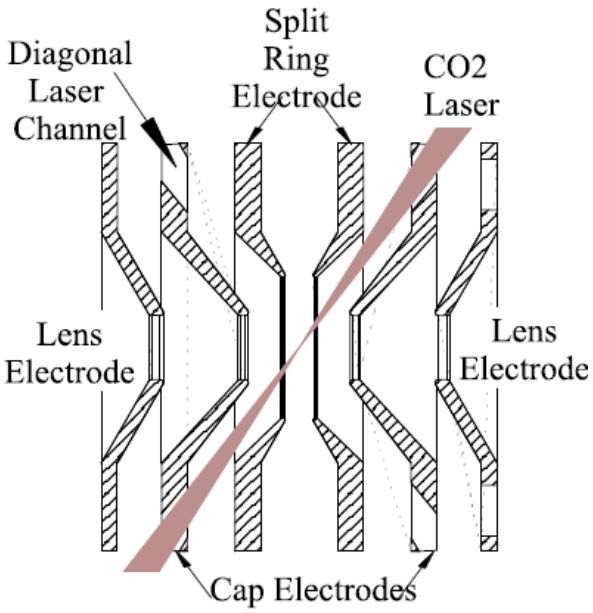

Figure 2.2. Detail Cross Section of Split Ring Electrode Trap. Trap has diagonal channels for laser passage, and lens electrodes used for particle gating and driving secular motion.

CHAPTER 3

MEASURING THE MASS OF NANOPARTICLES BY NANOPARTICLE MASS SPECTROMETRY

3.1 Introduction

No matter what the ultimate scientific aim of a nanoparticle mass spectrometry experiment might be mass measurement is always part of the experiment. The goal of this chapter is to present one method of measuring *M* by NPMS. *M* cannot be measured directly, but can be calculated by independently measuring *M/Q* and *Q*. As discussed in the previous chapter, *M/Q* for ions in a quadrupole trap is proportional to the secular frequency along one of the trap axes:

$$\frac{M}{Q} = \frac{\sqrt{2}V_0}{\omega_z \Omega z_0^2} \tag{3.1}$$

Provided *Q* is known exactly, *M* is known to the precision of the measurement of ω_z. Several groups use charge detection schemes to measure *Q* independently.[1-3] While this method has the advantage of speed and convenience, measurements are inherently destructive and are only precise to about 0.1%. Our method is to intentionally change *Q* while continuously monitoring ω_z. *Q* changes by multiples of e and, by measuring the size of the 'charge step' ($\Delta\omega_z$), *Q* can be determined by the following relation:

$$\frac{Q}{\Delta Q} = \frac{\omega_z}{\Delta\omega_z} \tag{3.2}$$

where ΔQ, an integer multiple of e, is the charge gained or lost during the step. Variations on this method have been used since at least 1983, when Philip et al. used UV photons to eject electrons from an aerosol particle in an electrodynamic balance and extract *Q*, and therefore *M*, from the change in the observed *M/Q*.[4]

An example of the charge stepping procedure is shown in Figure 3.1. The main frame of the figure shows how both the LIF intensity and ω_z of a trapped nanocrystal quantum dot (QD) changed over the course of ~2 h. The sharp steps in ω_z reflect changes

in Q due to collisions with electrons, Ar^+, or Ar^* metastables created by a discharge (the cold cathode gauge used to measure the argon pressure). Measurement of Δf_z (~1250 Hz/e) allows us to determine Q at each step, as indicated in Figure 3.1. Once Q is known, Equation 3.1 is used to convert ω_z to M, which is plotted against the far right hand scale. It can be seen that the particle mass slowly decreased over the course of the measurement, presumably because the LIF laser heats the particles, resulting in evaporation from the particle. The figure also shows how LIF intensity varies with time as the particle is undergoing charge steps and slow mass loss. During the first few minutes (while $Q = 16$), there is a rapid ~50% decrease in LIF intensity, but the intensity stabilizes when the transition to $Q = 15$ occurs. Thereafter, the LIF intensity slowly increases again without much obvious correlation with charge stepping. A detailed discussion of the photophysics of trapped QDs can be found in Chapters 4 and 5.

3.2 Measuring ω_z

Our methods for measuring ω_z have been discussed in detail elsewhere[5] and will only be discussed in brief except where significant advances have been made. If the scattered light intensity (I) is high enough, approximately 10^5 counts / s or greater, it is possible to observe modulation of I due to secular motion of the particle. From a long record of I(t) it is possible to obtain a frequency spectrum by Fourier transform, as first demonstrated by Gerlich.[6] This method requires I to be sufficiently large (~ 100 000 photon counts / s). It is also possible to measure ω_z by resonantly exciting the secular motion of the particle by applying a weak sinusoidal drive voltage at frequency ω_{drive} to an electrode just outside the trap. ω_{drive} is then swept over the range where ω_z is expected

to lie. Due to field penetration, axial oscillation of the trapped NP is excited when ω_z and ω_{drive} are in resonance, leading to a dip in the PL signal because the NP spends less time in the ~50 μm wide detection volume. When the argon pressure is high, e.g. 10^{-3} Torr, the oscillation is quickly damped as ω_{drive} moves out of resonance with the NP. This creates a sharp negative peak in I(t). This resonant excitation or 'frequency sweep' method has the advantage that it does not require a large I. Indeed, it works quire well when I is on the order of a few tens of counts / s.

The inset to Figure 3.1 shows an example data set for a single quantum dot trapped at 280 kHz and V_0 = 500 V. For this measurement, we applied a variable frequency AC signal of amplitude 5 V to one of the electrodes labeled "lens electrode" in Figure 2.2. The inset to the figure shows the LIF intensity over a single sweep of AC drive frequency. Note that there is significant response only when the AC frequency is resonant with ω_z. On resonance, there is a sharp dip because the driven resonant motion causes the particle to spend less time in the detection volume defined by the overlap of the laser focus and APD viewing area (~50 μm x 50 μm x 100 μm). The width of the resonance, hence, the precision of the ω_z measurement, can be varied to suit the experiment. Decreasing P_{trap} reduces broadening from collisional damping, and reducing the AC amplitude also sharpens the resonance, however, recording under these conditions requires slow sweep speeds. For Figure. 3.1, the conditions were optimized for fast sweep recording, because we wanted to be able to follow rapid changes in *M/Q* (AC amplitude = 5 V, P_{trap} = 1 mTorr, sweep speed = 0.67 kHz/s). The uncertainty of the measurement of f_z is expected to be better than the full width at half maximum (FWHM) of the response peak, which is about 125 Hz, or 0.7%. Indeed, when the NP was not

significantly losing mass, between 5 and 23 min, the standard deviation of the points is 47.6 Hz, an uncertainty of about 0.25%.

However, it is not the uncertainty in f_z, but in Δf_z, that determines if *Q* can be determined unambiguously. The absolute uncertainty for Δf_z is the same as that for f_z, ~ 48 Hz, but since Δf_z is only ~ 1250 Hz the relative uncertainty is now 3.8%, or ~1/26. With this level of uncertainty, we expect to be able to determine *Q* exactly only if $Q < 26$. While the resolution is sufficiently high in this case, this brings up the important point that if *Q* is large Δf_z is small, and even if f_z is known to be very high precision, the absolute uncertainty of Δf_z may be too large to determine Q.

3.3 Changing *Q* Using an Ultraviolet Lamp

Since precision cannot be increased arbitrarily it is convenient to have control of Q. While it is possible to alter the conditions of the ESI source to produce ions of desired *Q*, we have found that it is more convenient to change *Q* of a trapped NP using an argon discharge UV photon source[7] mounted on the end of the trap chamber (Figure 2.1). The source consists of a glass discharge capillary, a waveguide capillary that extends to within ~6 in of the trap, a pneumatically actuated flag separating the two which is used to gate the UV beam, and a tilt manipulator that allows the angle of the UV beam to be controlled. The UV photon flux can be controlled by changing the argon flux into the discharge capillary, and the fraction of photons that enter the trap can be controlled by changing the length of the waveguide capillary and by changing the angle of the UV beam using the tilt manipulator.

Operation of the UV lamp depends on the charge polarity of the trapped NP. To

date, we have experimented with silica and polystyrene particles with diameters between 80 and 200 nm, and have observed consistent behavior from both materials across that size range. In the case of both positive and negative particles the goal is to reduce the magnitude of the charge by either removing electrons or adding electrons. The UV beam diverges as it leaves the waveguide and, in the current configuration, photons pass through the trap center and strike the stainless steel trap electrodes, causing electrons to be emitted near the trap center by the photoelectric effect. Removing electrons from a negative particle is straightforward – exposure to UV photons excite electrons, ejecting them from the NP, reducing the magnitude of the charge. In our current configuration hundreds of electrons can be ejected per s of exposure to the UV beam if the beam is directed directly into the trap. In order to reduce the charge in a more controlled manner the beam is angled off center by a few degrees, resulting in charge loss rate of ~ 1e / s.

An example of controlled charge reduction is shown in Figure 3.2. The figure shows a Fourier transform of a 15 s record of the scattered light intensity from a negatively charged silica particle. The f_z ($f_z = \omega_z / 2\pi$) region is shown. The particle was exposed to the UV lamp for the duration of the data record. The eight distinct peaks represent the different values of f_z the particle had as it lost seven electrons, resulting in seven evenly spaced steps from 3025.5 to 2998.3 Hz. The individual peaks are quite broad, ~1 Hz full width at half maximum (FWHM) in some cases. It is likely the case that such a rapid change in f_z motionally excites a NP and broadens the frequency. Despite the broadness of the peaks, this set of step data can be used to make a crude, but useful estimation of M and Q using Equation 3.2. Here, $f_{z\_0} \sim 3025.5$ and $\Delta f_z \sim 4$ Hz, giving $Q_0 \sim -756e$ and $M \sim 647$ MDa. Using this method we have found that it is easy to

reduce the charge in a controlled manner from ~ -1000e to ~ -100 e in about an hour, presumably with no lower limit. For these experiments it is necessary to use a tunable RF source (see Chapter 2). To keep the effective potential high enough while the charge is decreased Ω must be adjusted several times. While it is very easy to remove electrons from a negative particle by this method, we have no way to add electrons back on.

We have had success raising and lowering the magnitude of the charge of positive NPs with a certain degree of control. For any given setting of the UV lamp there is a given flux of UV photons and electrons emitted from trap surfaces. It has been our observation that when the UV beam is pointed directly into the trap center a positive particle is likely to increase in charge (lose electrons). However, when the beam is angled away from center the particle is more likely to lose charge (gain electrons). Presumably the most photon dense portion of the UV beam directly in front of the capillary waveguide, and when beam is directed into the trap center the balance between photons and electrons at the trap center favors photons. When the beam is angled away from center fewer photons enter the trap and more photons strike the electrodes, causing more electrons to be emitted near the trapped NP.

In a typical experiment, a silica particle with a nominal diameter of 200 nm is trapped with a charge of ~ +1500 e. With the lamp tilted a few degrees from center it is easy to reduce the charge to ~ +700 e, at which point the electron affinity has decreased to the point that the NP is equally likely to capture a free electron as it is to lose an electron due to photon bombardment. By further detuning the lamp electron capture can be resumed, although much more slowly than before. It appears that further detuning lowers the flux of both photons and electrons, but tips the photon-electron equilibrium

back to favoring electron capture. As the charge decreases, equilibrium is eventually reestablished when the NP reaches a lower charge state. To date, we have not been able to lower the charge of a positive particle past ~ +200 e, presumably because some limit of the photon-electron equilibrium has been reached. Although this lower limit is a disadvantage of working with positively charged NPs, it is an advantage to be able to obtain an arbitrarily long record of charge steps.

3.4 Precision Charge Steps to Determine *Q* and *M* for GigaDalton NPs

If the *Q* of a NP is known exactly, *M* is known to the precision of the measurement of ω_z. We have shown in section 3.3 that it is relatively straightforward to determine the exact *Q* of a NP if *Q* is small, as is the case for small NPs. However, it is difficult to trap a NP in the GigaDalton range if *Q* is not at least 1000, and when *Q* is that large it is more difficult to determine it exactly. It is possible to trap a NP in this size and charge range and lower its charge using the procedure outlined above to make *Q* determination more convenient. The procedure for determining *Q* for a large NP is analogous to that outlined in Figure 3.1 – ω_z is measured repeatedly while *Q* steps and *Q* is determined from the size of $\Delta\omega_z$. However, the scattered light intensity from large particles is sufficiently large to measure ω_z by the Fourier transform approach. This allows us to work at lower pressures, where it is possible to measure the ω_z to higher precision.

Another difference is that the effect of gravity on particles with *M/Q* in the MegaDalton / e range is strong enough to pull particles away from the more electrically

ideal trap center. To counteract gravity, we have installed a 'levitation' wire that runs ~ 1 cm beneath the trap center perpendicular to the trap axis, and by applying a levitation bias (V_L) we can move a NP vertically in the trap. We have determined the approximate trap center by trapping a very low *M/Q* NP (~ 50 kDa / e) under the assumption that this gravity is negligible compared to the strong effective potential. Then our visible pump laser was optimized on this particle and was not moved. When a high *M/Q* particle is obtained it is centered in the laser, and therefore the trap, by adjusting the bias on the levitator to maximize scattered light intensity.

The effect of the levitation bias on a negatively charged silica NP with *M/Q* = 947 kDa / e is shown in Figure 3.3. The red trace is a frequency spectrum obtained by the Fourier transform method when V_L= 0 V. An ideal spectrum should feature two frequencies: f_r and $f_z = 2f_r$. It is evident from the large number of frequencies, especially below 100 Hz, near 2700 Hz, and above 4000 Hz, that the particle is in a highly nonideal field region of the trap. The f_z region (shown as inset) is complicated to the point that it is impossible to get a good measurement of *M/Q*. V_L was then slowly increased, and the particle was determined to be centered when V_L = -50 V, at which point another frequency spectrum was obtained (blue trace). The blue frequency spectrum is not perfect. There is still a high frequency peak at 4484 Hz, and f_z (2757.83 Hz) is not exactly twice f_r (1352.00 Hz). Why such nonidealities remain is not clear, but it is possible that the levitation wire is not perfectly below the trap center, and that it pushes the NP slightly off center in the horizontal as it centers the particle vertically. It could also be that the NP is not exactly centered vertically, given the rather crude method of determining the center. Still, the frequency spectrum is now easy to interpret, with one

clear f_z. In addition to eliminating spurious peaks, levitation shifts the apparent f_r and f_z peaks by - 2.17 Hz and + 1.63 Hz respectively. The fact that there is a shift is not surprising since levitation changes the potential the particle experiences. However, why f_r and f_z should shift in different directions is unclear. The frequency peaks are also much narrower after levitation. For example, the f_z peak in the centered spectrum now has a FWHM of 0.02 Hz (~7 ppm), where the apparent f_z peak in the uncentered spectrum at 2757.83 Hz has a FWHM of 0.2 Hz (~70 ppm).

Once a NP of the approximate *M* and *Q* has been prepared by charge lowering and has been centered in the trap an attempt to determine the absolute *Q* can be made. Our procedure is to induce many charge steps in a single record of f_z, and use Equation 3.2 to calculate the local value of *Q* at each step. Since the steps are obvious, it is easy to count backwards from each step and use each calculation of the local *Q* to calculate Q_0. In an ideal experiment each charge step would predict the same value of Q_0. An experiment attempting to measure *Q* and *M* of a negatively charged silica NP by conducting a series of 22 charge steps is shown in Figure 3.4. A frequency spectrum was acquired every 30 s, giving a frequency resolution of $0.0\overline{3}$ Hz. All steps involve electron loss, and although most steps are single electron loss events (Δf_z = 2.6 Hz), there are events where two, three, and four electrons were lost and one event where eight were lost.

Careful examination of the data record reveals that the secular frequency is not constant when the charge was constant. This becomes apparent if the charge steps in the data record are simply subtracted out (Figure 3.4, lower inset). f_z is drifting to lower frequency at a rate of ~ 0.1 Hz per hour, but jumps randomly in amounts up to 0.1 Hz on the 30 s timescale. The RF generator used in this experiment is a high voltage solid state

RF amplifier driven by a digital function generator (see Chapter 2). The stability of ω_z is limited by the stability of Ω and V_0, which are defined by the frequency and amplitude stability of the generator-amplifier combination. Digital function generators are frequency disciplined by an internal crystal oscillator and are expected to have frequency stability better than 1 ppm once warmed up. However, both the amplitude of the function generator output and the gain of the amplifier change as a function of temperature, since both depend on the resistance of internal components which change as a function of temperature. The amplifier is constructed with resistors that have temperature coefficients in the ppm range in order to minimize any temperature effects on the gain. Digital function generators are not designed to have this degree of amplitude stability, and it is therefore likely that any slow drift or random scatter of ω_z is due to fluctuations of the amplitude output of the generator. As a test of this hypothesis the amplifier was exposed to alternating period of warm and cool air flow, resulting in no observable change in ω_z of a trapped NP. When the experiment was repeated with the function generator ω_z was observed to increase with decreasing air temperature, suggesting the amplitude of the function generator, and thereforeV_0, increases with increasing temperature.

In an attempt to minimize the effect of time dependent changes in ω_z charge step sizes were determined by an extrapolation process (Figure 3.4, upper inset). The measurements of ω_z at each 'plateau' in the data record were fit to a line. In this experiment the trapped NP was exposed to the UV beam at the beginning of a frequency measuring scan so that if a step occurred it could be considered to have occurred at the time it appeared in the data record (vertical lines in inset). By extrapolating the fit of each level to the time of the charge step a value of Δf_z is obtained.

One method to determine Q from a series of charge steps is to simulate the experiment by fitting each step to a model that simulates each charge step height based upon an assumed Q_0. A plot can then be generated where the difference between the simulated and observed step heights is plotted against Q_0. The minimum of the resulting parabola is the predicted Q_0. Variations of this method have been used by several groups.[8-11] The problem with this method is that it is difficult to determine when the minimum value in the simulated error parabola is sufficiently different from the next best value. In other words, this method is a good way to determine what Q_0 is likely to be, but it doesn't provide insight into the error associated in the deamination of Q_0.

Our method is to use Equation 3.2 to calculate Q at each step, and by simply counting the total number of steps since the initial charge state, each step is used to calculate Q_0. Although this method requires more charge steps than the simulation discussed above, the standard deviation of the distribution of predicted Q_0 values can be used to determine whether Q_0 has been determined unambiguously. The 22 values of Q_0 calculated in the experiment shown in Figure 3.4 are plotted in Figure 3.5. The average of these values is -85.2 e with a standard deviation of 0.5 e, illustrating that Q_0 is either -85 or -86 e. Since Q is only known to a precision of 2/85, M cannot be known to any higher precision, giving $M = 2.96 \pm 0.07$ GDa, consistent with the mass of a 153 nm silica particle.

While this is a largely unsatisfying conclusion, it is useful to have a criterion that can be used to determine that we have not determined Q_0 unambiguously in this case, even though Q_0 is only about – 85 e, and that f_z can be measured to a precision of ~7 ppm using a single measurement. The problem here is almost certainly that our frequency source is not amplitude stabilized, causing scatter and drift in f_z, ultimately resulting in a

large uncertainty in the measurement in Δf_z, as evidenced by Figure 3.4. If this electronics problem could be overcome, it is likely that many measurements of f_z would result in a precision on the order of 1 ppm, and that the observed values of Δf_z would be much more consistent, allowing absolute determination of *Q* even if *Q* is on the order of a few hundred e.

3.5 References

1. W.-P. Peng, H.-C. Lin, M.-L. Chu, H.-C. Chang, H.-H. Lin, A. L. Yu, and C.-H. Chen, Anal. Chem. **80**, 2524-2530 (2008).

2. T. Doussineau, P. Dugourd, and R. Antoine, Spectrosc. Eur. **24** (4), 16-20 (2012).

3. N. C. Contino, E. E. Pierson, D. Z. Keifer, and M. F. Jarrold, J. Am. Soc. Mass Spectrom. **24**, 101-108 (2013).

4. M. A. Philip, F. Gelbard, and S. Arnold, J. Colloid Interface Sci. **91** (Copyright (C) 2015 American Chemical Society (ACS). All Rights Reserved.), 507-515 (1983).

5. D. M. Bell, C. R. Howder, D. Gerlich, D. K. Lewis, and S. L. Anderson, Int. J. Mass Spectrom. **(submitted)** (2014).

6. S. Schlemmer, J. Illemann, S. Wellert, and D. Gerlich, J. Appl. Phys. **90** (10), 5410-5418 (2001).

7. F. S. Roberts and S. L. Anderson, Rev. Sci. Instrum. **84**, 126101 (2013).

8. M. A. Tito, K. Tars, K. Valegard, J. Hajdu, and C. V. Robinson, J. Am. Chem. Soc. **122**, 3550-3551 (2000).

9. W. P. Peng, Y. C. Yang, C. W. Lin, and H. C. Chang, Anal Chem. **77** (21), 7084-7089 (2005).

10. A. J. Trevitt, P. J. Wearne, and E. J. Bieske, Int. J. Mass Spectrom. **262** (3), 241-246 (2007).

11. W.-P. Peng, Y.-C. Yang, M.-W. Kang, Y. T. Lee, and H.-C. Chang, J. Am. Chem. Soc. **126**, 11766-11767 (2004).

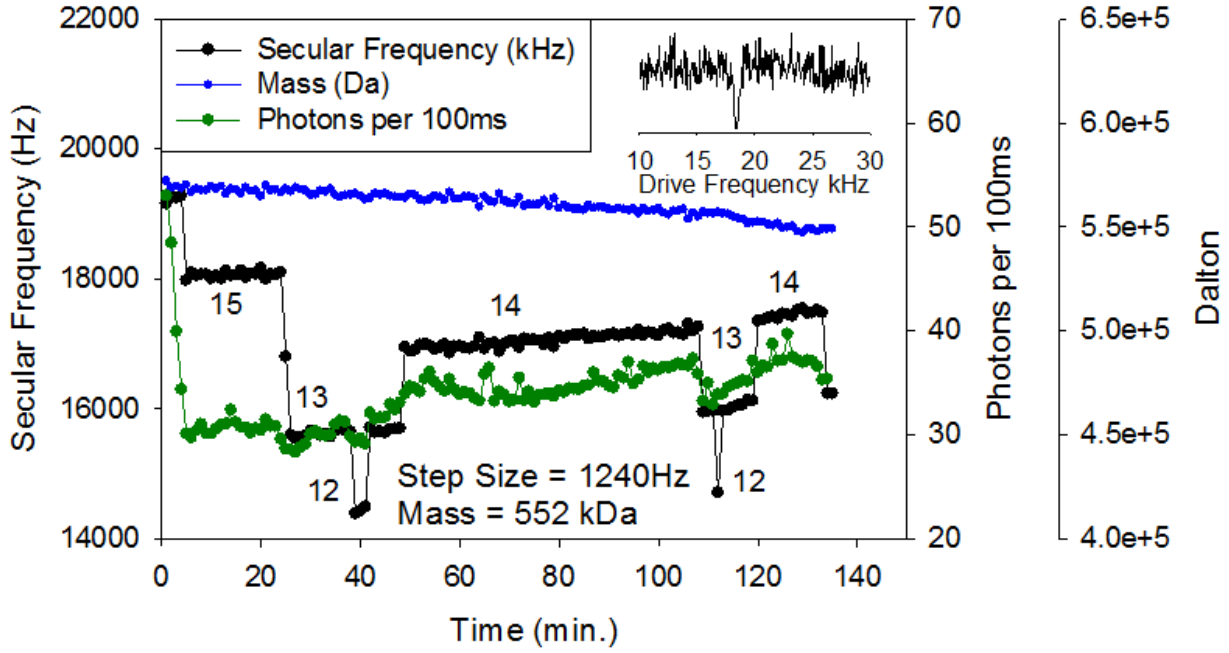

Figure 3.1. Sample of *Q* and *M* Measurement by Charge Stepping. Record of secular frequency (f_z), particle mass (M), and laser-induced fluorescence intensity as a function of time, for a single 5 nm core, 1 nm shell, CdSe/ZnS quantum dot. A single frequency spectrum is given as an inset.

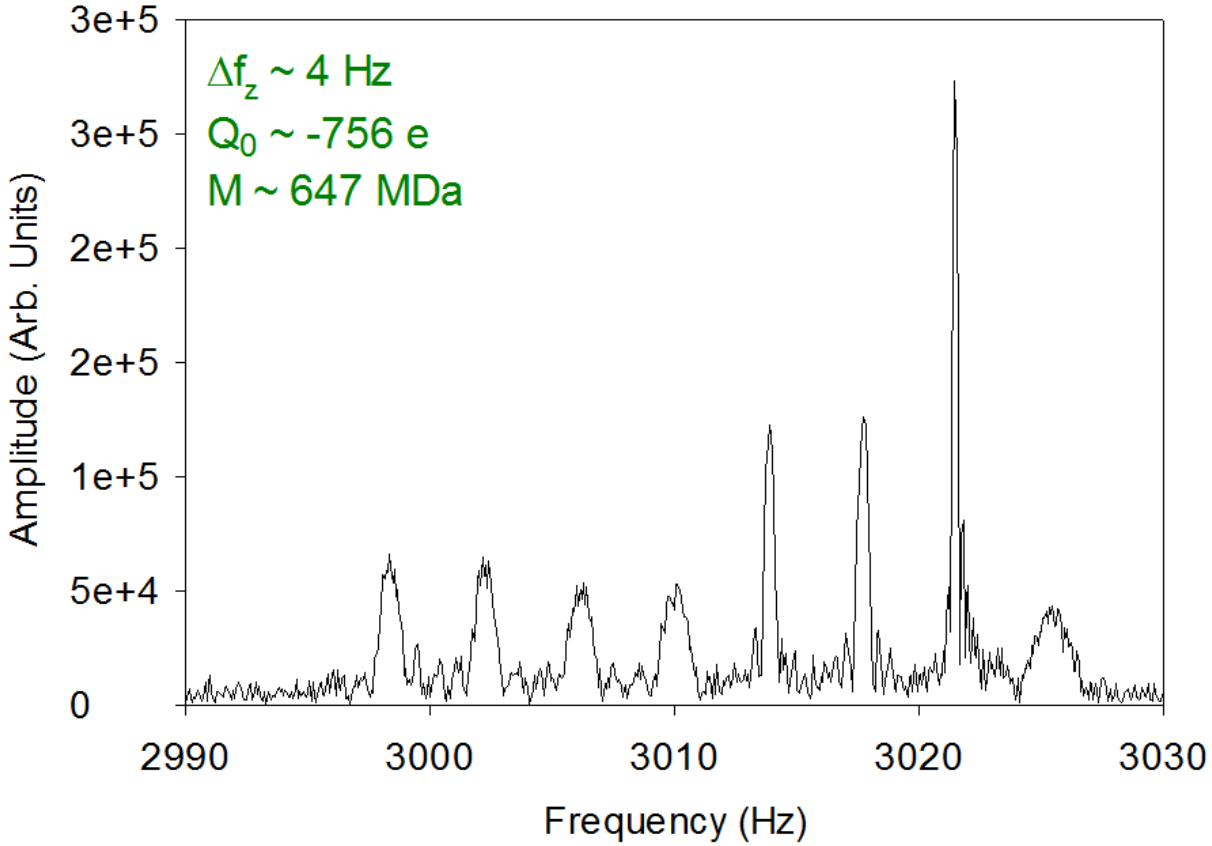

Figure 3.2. Frequency Spectrum Illustrating Charge Stepping. The axial secular frequency region of a Fourier transform acquired while electrons are ejected from a negatively charged silica NP, nominal diameter = 200 nm. The spacing of these unit charge steps, ~ 4 Hz, can be used to estimate *M* and Q.

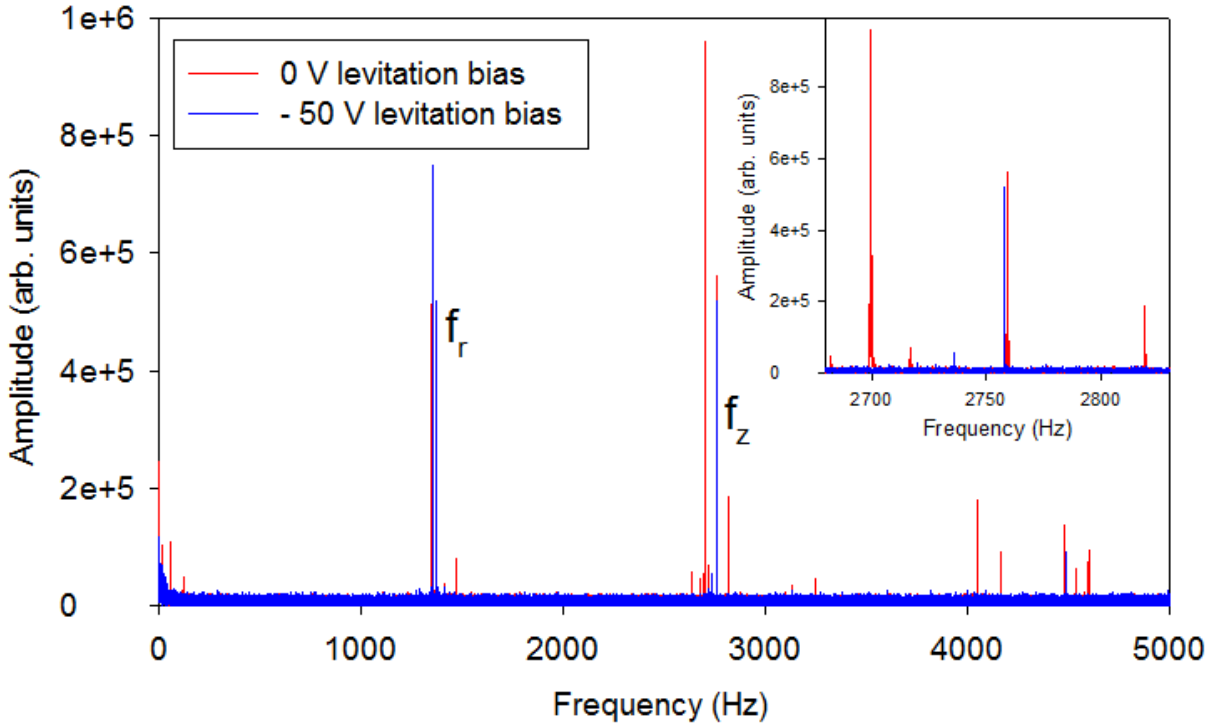

Figure 3.3. Frequency Spectrum Before and After Levitation. A Fourier transform of a 947 kDa / e negatively charged silica NP with 0 V (red trace) and – 50 V (blue trace) 'levitation' biases. The voltage was applied to a wire positioned below the trap to move the NP into the trap center. Centering removes many of the features present in the Fourier transform due to nonidealities in the trapping field away from the trap center, especially in the f_z region (shown as inset) and in the region above 4 kHz.

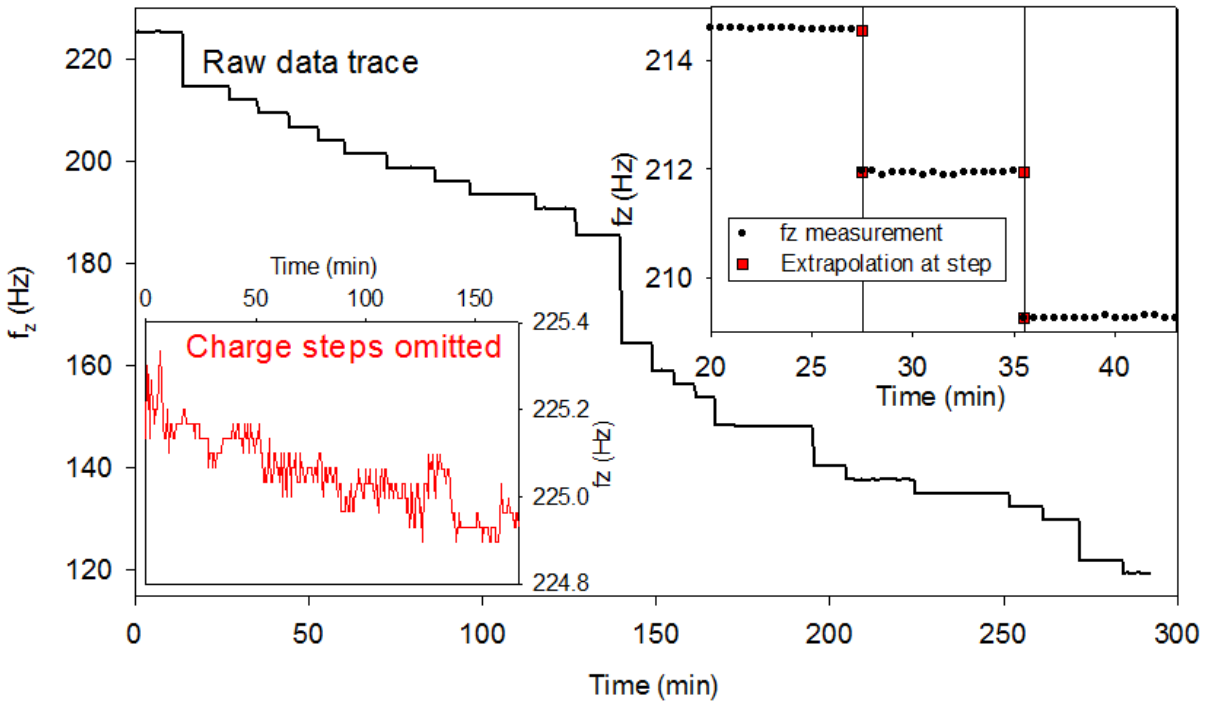

Figure 3.4. Measurement of *M* and *Q* of a GigaDalton NP by Charge Stepping. The secular frequency (f_z) of a nominally 200 nm silica particle as the charge is lowered using a UV lamp. There is a significant scatter and drift in the f_z record, which becomes apparent when the charge steps are subtracted from the raw data (lower inset). The size of the charge steps is determined by an extrapolation process (upper inset).

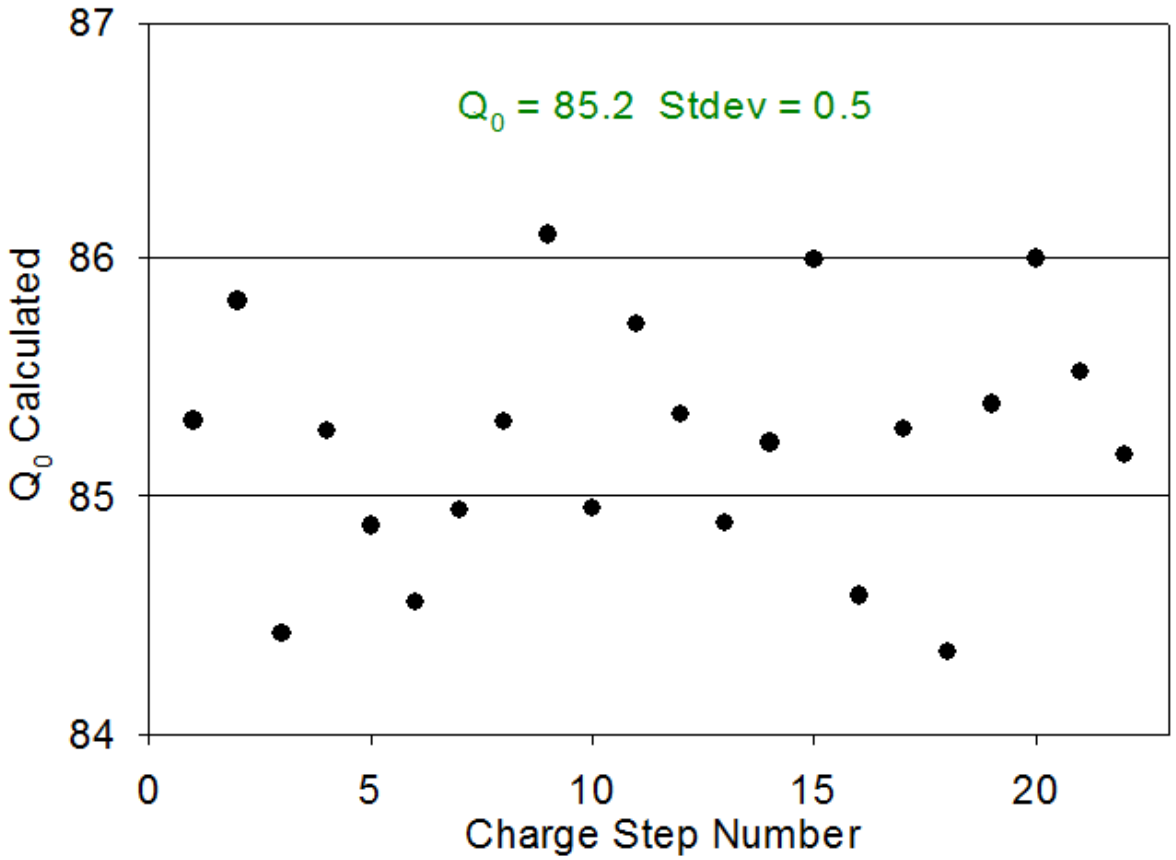

Figure 3.5. Values of Q_0 Determined by Charge Stepping Experiment. The values of Q_0 predicted from the 22 charge steps shown in Figure 3.4. The standard deviation indicates that Q_0 is most likely 85, but could possibly be 86. Since Q has not been determined absolutely, M is only known to the uncertainty in Q, 2/85.

CHAPTER 4

PHOTOLUMINESCENCE OF CHARGED CdSe/ZnS QUANTUM DOTS IN THE GAS PHASE: EFFECTS OF CHARGE AND HEATING ON ABSORPTION AND EMISSION PROBABILITIES

4.1 Introduction

Accurate, nondestructive mass determination for trapped nanoparticles (NPs) enables a number of interesting experiments, such as measuring kinetics for NP surface reactions by monitoring mass vs. time as an NP is heated or exposed to reactants,[1] or studying spectral properties of single NPs in the gas phase. Several groups have reported experiments wherein single NPs were trapped in a quadrupole (Paul) trap,[1-4] with continuous determination of the mass (M) and charge (Q) by monitoring the motional frequency of the trapped NP. For large NPs, motion is easily monitored by scattering of a low-power laser focused through the trap, and NPs that are too small for detection by light scattering (< ~50 nm) can be monitored by photoluminescence (PL), if they have significant PL quantum yields. Unfortunately, many interesting systems, such as small NPs of catalytically interesting metals, meet neither of these requirements. We are developing an approach to mass analysis of small "dark" NPs based on cotrapping with one or more small photoluminescent probe NPs, which must have reasonably strong, nonblinking PL that is stable under laser pumping for many h, even when heated.

As shown recently,[5] CdSe/ZnS core shell quantum dots (QDs) appear to meet all these requirements, but only after they have been 'brightened' by laser heating. The observation that PL intensity increases by factors of up to 1000 after intense laser heating is counter to the usual experience for QDs in the condensed phase, and the motivation for this chapter is to examine the nature of the thermal-brightening process. We report emission spectra and intensities for a variety of as-trapped and laser-heated QDs pumped at different wavelengths, explore the effects of buffer gas pressure on the brightening process, discuss thermal balance in the laser-heated QDs, and derive estimates of gas

phase QD absorption cross-sections and emission quantum yields before and after heating. In addition to our own application, the laser-brightened QDs may prove useful in other applications where a robust luminescent probe is needed, capable of functioning over a wide temperature range.

QDs are widely used as fluorescence markers in the condensed phase, and their photophysics in condensed phase has been studied in great detail.[6-8] In brief, QDs have a near continuum of electronic states in their valence and conduction bands, which are separated by a band gap. The band gap of QDs decreases with increasing diameter, such that large QDs absorb and emit lower energy photons than small QDs. Photons with energy exceeding the band gap energy are absorbed, pumping an electron into the conduction band, and creating a hole in the valence band. The exciton relaxes and then recombines, resulting in emission of a photon with energy equal to the band gap energy. Current synthetic techniques yield QDs whose fluorescence quantum yield (QY) approaches unity.

Few observations of gas phase QD photophysics have been made, with the notable exception of Xiong *et al*. who studied the photoelectron spectrum of a beam of QDs in the gas phase, directly probing the density of states.[9] Here we present a study of gas phase QD photophysics before and after QDs are heated. Before heating, as-trapped QDs are only weakly emissive, but with spectra that are superimposable on the solution phase spectrum of the same QDs. Heating, either with a CO_2 or visible laser increases the brightness of trapped QD emission by factors of up to 1800, and causes dramatic changes in the emission spectrum, which becomes independent of QD size, and has peaks to the blue of the band-gap emission, in the red, and in the near IR. The emission of QDs in the

condensed phase is also altered by heating; however, the effect is mainly a red shift in the emission and a decrease in emission quantum yield, until, at sufficiently high temperature (~520 K) PL is totally quenched.[10-12] The effect is believed to be due to creation of surface sites which act as electron traps.

In our experiment, either single NPs or small ensembles of NPs are confined in a radio-frequency quadrupole ion trap, where they can be studied nondestructively for long time periods, allowing repeated measurements of the PL emission spectrum before and after laser heating, and accurate determination of the mass of the NP, and its charge. As in Chapter 2, there is a well-defined frequency for motion of charged NPs in a quadrupole trap, which is a function of the NP's mass-to-charge ratio (*M/Q*). *M/Q* can, therefore, be determined by measuring the motional frequency of the trapped NP, using PL to detect the motion. *Q* can be exactly determined by observing steps in *M/Q* induced by charge-changing collisions with ions or electrons in the buffer gas, and once *Q* is known, *M* is also determined. The PL emission spectrum is measured by observing the emission through a series of longpass filters.

To be trapped, the QDs in our experiments must be charged. We generate positively charged QDs with charges between +5e to +20e per QD using electrospray ionization (ESI). Charging[13-15] or doping[16-18] of QDs has been shown to have a significant impact on PL because the charge (either positive or negative) interacts with the exciton. In ESI the excess charge (excess Na^+ in this case) is confined to the surface of the NP. The effect of ESI charging of CdSe/ZnS QDs was investigated by Barnes *et al.*,[19] who electrosprayed QDs, then immediately collected and dried them on a surface and analyzed the PL. For negative charging, they observed an emission blue shift of 60 meV

and a decrease in PL lifetime as a result of an average charge of -5e. For positively charged QDs they observed PL properties similar to the solution phase. In our case, the NPs are isolated in a low pressure buffer gas, allowing us to precisely determined *M* and *Q*.

In the following experiments, both QD monomers and NPs consisting of small aggregates of QDs are trapped. For particles where the mass, hence the identity, was determined, we will refer to the particle as a "monomer" or a "dimer." In experiments where the mass was not determined, we will use the term "NP," which includes both monomers and small aggregates.

4.2 Trapping and Detecting QD Ions

CdSe/ZnS core/shell QDs of various sizes were obtained from NN Labs as aqueous solutions, and were electrosprayed and trapped using the procedure described in Chapter 2. With experience using the isolation valve used to gate the ion beam, it is possible to inject single NPs with reasonably good control. It is also possible to inject a small ensemble of NPs, and then selectively reduce the ensemble to a single NP using a high amplitude AC sweep applied to an electrode near the trap center. Unless otherwise stated, for the experiments here, $F = \Omega/2\pi = 143.3$ kHz, and $V_0 = 500$ V.

Because of aggregation, either in the QD solution used for ESI, or in the ESI process itself, it is possible to examine small aggregates ($N < 10$ QDs), in addition to QD monomers. Once trapped, NPs are detected optically using either a continuous wave (cw) 532 nm laser (500 mW maximum power, Ultralasers) or a cw 445 nm laser (2W maximum). For the experiments described here, we wished to avoid heating the NPs with

the PL lasers; therefore, a loose focus was used. The beam waist diameter was estimated by moving the laser beam vertically through the trap when a single, large polystyrene particle (~100 nm) was trapped. By measuring the light scattering intensity as a function of position, we determined the beam waists to be ~500 μm and ~550 μm, respectively for the 532 and 445 nm lasers. The trap design also includes a pair of confocal off-axis parabolic mirrors that allow a quasi-cw CO_2 laser (Synrad, 10 W maximum average power) to be focused radially through the trap center for NP heating.

Fluorescence signal was detected at 90° with respect to the laser direction, by collecting light from the trap center through the gap in the split-ring electrode, and collimating it with a 25 mm focal length aspheric lens. The collimated light was passed through either a 532 nm notch filter or a 495 nm long-pass color filter, to block scattered laser light, and optionally passed through additional long-pass color filters, and then either focused onto the image plane of an inexpensive CCD camera (Imaging Source), or onto an avalanche photodiode detector (APD) (Laser Components: Count 50). From the image magnification and APD size, we estimate that light is collected from a ~50 μm x ~50 μm x 500 μm volume, which we will refer to as the detection volume. The detection solid angle is ~0.34 steradians, limited by the trap electrodes, and taking reflection losses (25-30 %) into account, we estimate that the net PL detection efficiency is ~1.5 % for wavelengths near the peak of the APD detection efficiency (85 % at 670 nm). The other issue that affects detection efficiency is the overlap of the detection volume with the NP ensemble, or the volume of thermal motion in the case of single NPs. For NPs with M and Q in the ranges of interest here, the thermal motion has root-mean-square radial amplitude ranging from ~20 to ~50 μm, with axial amplitude half the radial value.

4.3 Measuring Emission Spectra

Because the experiments described below were done at low pump laser intensity in order to minimize heating of the NPs, the emission was quite weak, however, at low laser power the emission is stable on a >1 h time scale. Therefore, to obtain spectral information we used a series of long-pass color filters. A six position filter wheel was inserted in the optical path, populated with five filters with cutoff wavelengths of 590 nm, 645 nm, 695 nm, 780 nm, and 850 nm, leaving the sixth position empty for collection of emission filtered only by either a 532 nm notch filter or 495 nm long pass filter, used to block scattered laser light from pump lasers at 532 nm or 445 nm, respectively. To collect an emission spectrum, signal was counted for 100 s for each color filter. To allow subtraction of background (APD dark counts, scattered laser light), the same procedure was used either immediately before or after the spectral measurement, but with the trap empty of NPs. Under these conditions the reproducibility of the spectra is quite good (<5 %), as shown in Figure 4.1. One issue for these measurements is that if the pump laser intensity is too high, it can heat the NPs enough to change their emission properties. To check whether this had happened during the spectral measurements, the unfiltered signal level was measured before and after each spectral measurement, and if the intensity had changed by more than 5 %, the result was discarded.

The emission spectra were obtained by a subtraction process. The raw intensities for each filter wheel position were first corrected using the background spectrum obtained with the trap empty. Next, the signal obtained with the 590 nm cutoff filter was subtracted from the intensity obtained with no color filter, the result being the intensity in the spectral range between 590 nm and either the 532 nm pump laser, or the 495 nm

cutoff filter used when pumping at 445 nm. The process was repeated for each pair of color filters in order to obtain intensities in the spectral range between their cutoff wavelengths. Finally, the intensity measured with the 850 nm filter inserted represents the intensity between 850 nm and the ~1000 nm sensitivity limit of our APD. The raw spectral intensities were then scaled using information from the APD manufacturer regarding the variation of quantum efficiency with wavelength.

For the purpose of comparison, solution phase emission spectra were measured using the same procedure and pump laser intensities, but replacing the trap with a cuvette containing solutions of the QDs prepared by diluting the commercial stock solution 1:100 in methanol.

This approach to emission spectroscopy gives poor spectral resolution compared to a spectrometer, but its high detection efficiency allows spectra to be acquired at signal levels as low as ~50 counts/s. In principle, it would be possible to generate spectra at lower signal levels by using longer integration times; however, the tradeoff is that the QDs are more likely to undergo processes (heating or reactions with background gas) that change their spectral properties during the measurement.

4.4 Emission Spectra and the Effects of Thermal Brightening

Images of an ensemble of trapped, gas-phase CdSe/ZnS QD, based NPs before and after brightening are shown in Figure 4.2. An ensemble of ~100 NPs was trapped and pumped at 532 nm with ~153 W/cm^2, with 10 mTorr of Ar buffer gas to help cool the NPs. As trapped, the emission intensity is barely detectable by the CCD even with 2 second frame rate. The NP ensemble was then heated by CO_2 laser irradiation (10.6 μm)

for 2 s at an estimated intensity of ~1 kW/cm^2, and then reimaged with the CCD after the CO_2 laser was turned off. It can be seen that 2 s of heating lead to a dramatic brightening of the QD NP emission intensity. This brightening is irreversible, *i.e.*, it does not decay if the NPs are trapped in the dark or continuously irradiated in the visible, or if the argon pressure is varied.

The primary goal of this chapter is to understand the processes leading to the initially weak PL efficiency, and the thermal-induced PL brightening. Important insights can be obtained by examining the emission spectra of different core size QDs, before and after CO_2 laser-induced brightening. In the following, we will refer to the QDs by the color of their solution-phase band-gap emission: green (λ_{max} = 540 nm, d = 2.5 nm), yellow (λ_{max} = 575 nm, d = 3.9 nm), orange (λ_{max} = 605 nm, d = 4.2 nm), and red (λ_{max} = 650 nm, d = 5.5 nm). The diameters given do not include the 1 nm thick ZnS shells, or the mercaptoundecanoic acid ligands. In the ideal experiment, we would trap and measure the mass, charge, and emission spectrum for single QD NPs, before and after CO_2 laser irradiation. Unfortunately, the emission from as-trapped, unbrightened NPs is far too weak to allow measurements on single NPs. Therefore the as-trapped spectra are all for small ensembles of NPs. The mass and charge determination method does not work for large ensembles, therefore, we cannot directly determine how many and what type of NPs are in the trap. After brightening, the intensities are sufficient to record PL spectra for both ensembles and single NPs, and for the latter, we can determine the mass and charge unambiguously.

4.4.1 532 nm Excitation

Figure 4.3 shows emission spectra for four different color QD NPs, all pumped at 532 nm. The six point emission spectra presented here were measured using a series of long pass color filters that can be inserted into our optical detection path (see Introduction). The vertical dashed lines are the cutoff wavelengths for each of the filters used, and the data points centered between the cutoffs represent the integrated emission intensities in each wavelength range, determined by subtracting intensities measured through the series of filters. In each frame, spectra are shown for the QD NPs in methanol solution, for small ensembles of as-trapped, unbrightened NPs, and for the same ensembles after CO_2 laser irradiation.

The spectra of as-trapped NPs were obtained using 532 nm pump laser intensities between 70 and 125 W/cm^2 and argon buffer pressures between 5 and 25mTorr, with conditions optimized to minimize heating, avoiding unwanted brightening. (The visible pump laser also heats the NPs, because only a fraction of the absorbed energy is re-emitted). It is important to note that the experiments were done by injecting NPs into the trap while monitoring PL emission at low pump laser intensity, continuing injection until a signal level of at least 50 counts/s was observed, typically taking less than 5 s. As a result, the size of the ensembles examined should have been roughly inversely proportional to the PL efficiency for the particular combination of QD color and pump laser intensity. For combinations where the as-trapped PL is relatively efficient, fewer than ten NPs provided sufficient intensity, but for combinations with very low PL efficiency, there may have been hundreds of NPs in the trap. Once an appropriate ensemble was trapped, the "as-trapped" emission spectrum was taken using the filter set,

and then the ensemble was exposed to the CO_2 laser at 1 kW/cm^2 for ~5 s, thereby increasing the fluorescence intensity by factors ranging from 55 to 1800. After turning off the CO_2 laser, the "CO_2 laser- heated" emission spectrum was taken, and then the NPs were ejected from the trap to allow measurement of a background spectrum for the empty trap. The background subtraction process is not perfect, resulting in occasional points with negative background-subtracted intensities. These are within the expected repeatability of the spectra (Figure 4.1), and give an idea of the uncertainty inherent to the low signal levels for the as-trapped spectra.

To obtain the as-trapped spectrum for red QD NPs (QDs with 5.5 nm core diameter) shown in panel A, the NPs were injected into the trap with argon buffer pressure of 15mTorr with the 532 nm laser blocked. The pressure was then lowered to 10mTorr, and the NPs were exposed to the 532 nm laser at ~80 W/cm^2, and the emission spectrum was recorded. The total (unfiltered) photon count rate was ~300 counts/s. Note that the spectrum of as-trapped red QD NPs in the gas phase is quite similar to the spectrum recorded using the same method for the QD NPs in methanol solution, with a peak between 645 and 695 nm consistent with the manufacturer's reported emission spectrum (nominal λ_{max}=650 nm). For the as-trapped spectrum, ~75% of the total emission is in the range expected for band-gap emission, and most of the rest comes in a feature between 532 and 590 nm that is not present in the solution spectrum. This feature suggests there are emissive states in the as-trapped NPs with energies above the band gap. Although we made every effort to minimize the temperature of the as-trapped NPs, we cannot exclude the possibility that this above-band-gap emission was the result of heating by the PL laser. Note that the solution spectra in Figure 4.2 have been scaled so

that their integrated intensities match those for the as-trapped ensembles, to allow the spectra to be compared directly. It is not possible to directly compare the absolute intensities, because even in the dilute methanol solution, the number of NPs the detection volume is ~10^5 to 10^6 times larger than in the trap, and the emission was so bright that the spectrum was collected without lenses used collect and focus emission from the trap. In principle, we could dilute the solution to obtain NP density comparable to that in the trap, however, the dilution would be so large that issues such as NPs sticking to the cuvette walls would make the comparison useless.

After exposure to the CO_2 laser, the total emission intensity increased by a factor of 55, and the spectrum changed significantly. The emission in the band-gap region between 645 and 695 nm increased by a factor of 20, as did the above-band-gap feature (532-590 nm), but the spectrum is dominated by emission in the near IR, between 780 nm and the 1000 nm APD cut-off. (Note: The spectra are weighted by count rate, rather than emitted energy). Even with our low spectral resolution, it is clear that there are *at least* three main emission features for the brightened ensemble, and the emission level is still well above background in the two spectral ranges between the three emission maxima. Clearly, IR heating of the NPs created a wide variety of emitting states. See below for higher resolution spectra of single red QD monomers.

The experiments for orange (panel B; 4.2 nm core dia.), yellow (panel C; 3.9 nm core dia.), and green QD NPs (panel D; 2.5 nm core dia.) were done similarly. For orange QD NPs a 532 nm laser intensity of 80 W/cm^2 was used with an argon pressure of 10 mTorr. The as-trapped and solution spectra are in near-perfect agreement, with a feature between 590-645 nm consistent with the expected band-gap emission (nominal λ_{max} =

605, width 20 nm). IR heating increased the total photon count rate by a factor of ~160. After heating the spectrum of the brightened orange QD NPs no longer had a maximum corresponding to band-gap emission, and instead had structure quite similar to the spectrum of the CO_2 laser-heated red QD NPs, but with intensity distribution weighted more strongly at shorter wavelengths, such as higher intensity in the 532-590 nm range, with less in the near IR. For yellow QD NPs (panel C), it was necessary to increase the 532 nm laser intensity to ~180 W/cm^2 to obtain sufficient emission signal (with 10 mTorr of argon buffer gas). Despite the higher pump laser intensity, the as-trapped spectrum is superimposable on the solution spectrum. In both cases, the emission peaks at the blue end of the spectrum, as might be expected given the fact that the solution emission maximum reported by the supplier (λ_{max} = 575 nm) is close to 532 nm pump wavelength. After CO_2 laser heating, the total emission intensity increases by a factor of ~1800, and again, the brightened spectrum has features similar to those of the brightened orange and red QD NPs, but with the intensities weighted even more toward the blue.

The situation is somewhat different for the green QD NPs (Figure 4.3D). The manufacturer indicates that the solution phase emission spectrum for these runs between 520 and 550 nm, and the first maximum in the absorption spectrum is shifted roughly 30 nm to shorter wavelength. Therefore, the 532 nm pump laser is able to excite only that fraction the population with the reddest absorption spectra. As expected, the solution spectrum has significant emission only in the 532 – 590 nm range. It proved impossible to obtain an unbrightened spectrum for these QD NPs with the 532 nm pump laser, and the dependence of emission intensity on pump laser intensity provides additional insight. As the intensity was gradually increased, the emission was undetectable (<20 counts/sec)

until the intensity reached ~100 W/cm^2, at which point the emission suddenly jumped to ~900 counts/s. We then took the "as-trapped" emission spectrum shown in Figure 4.3D, which looks nothing like the solution spectrum. Upon CO_2 laser heating, a further increase in intensity by a factor of ~50 occurred, with essentially no change in the emission spectrum, suggesting that the "as-trapped" spectrum was actually for NPs that had been heated and brightened by interaction with the 532 nm laser. Based on experiments and simulations discussed below, thermal brightening of QD emission appears to be an all-or-nothing effect. Individual NPs cannot be partially brightened. Therefore, the factor of 50 increase in emission from CO_2 laser heating suggests that ~2 % of the as-trapped ensemble were brightened by the 532 nm laser (presumably those with the reddest absorption spectra), and the rest were only brightened when CO_2 laser heated.

4.4.2 445 nm Excitation

Based on the behavior of the green QD NPs with 532 nm excitation, we would expect to be able to obtain an as-trapped, unbrightened spectrum for the green QD NPs using a bluer pump laser. As shown in panel B of Figure 4.4, this is correct. An ensemble of green QD NPs was trapped in 15mTorr of Ar with the laser blocked. The pressure was then raised to 20mTorr and V_0 was lowered from 500 to 450 V before exposing them to the 445 nm pump laser at ~125 W/cm^2 intensity. Because the photon energy and the emission Stokes shift are higher when pumping at 445 nm, the heat load on the NPs is higher. The higher argon pressure helps collisionally cool the NPs, and the lower V_0 also helps by allowing the ensemble volume to expand, such that each NP spends a smaller

fraction of the time in the laser focus. The as-trapped spectrum is in excellent agreement with the solution spectrum, with a single emission feature in the 495-590 nm range (limited by the 495 nm long-pass filter used to block scattered laser light), consistent with the nominal band gap emission (λ_{max}=540 nm). The effect of CO_2 laser heating on the NPs was qualitatively similar to that seen with the 532 nm pump laser – a new feature grew in in the 645 - 695 nm range, but the brightened spectrum was dominated by near-IR emission. The total intensity increase in this case was only a factor of ~6.

Panel A of Figure 4.4 shows 445 nm laser pumping of the red QD NPs. The as-trapped and solution phase spectra are essentially identical, and then after CO_2 heating, significant new intensity grew in both to the blue of the original peak, and in the near IR. The brightened spectrum is quite similar to that seen for the red QD NPs with 532 nm pumping, however, the intensity increase from CO_2 laser heating was only a factor of 4, compared to a factor of 55 for 532 nm pumping.

The similarity of all the brightened spectra suggests that heating, by either the CO_2 or 532 nm lasers, creates new states in the NPs, and the fact that the spectra are similar, independent of QD diameter/band-gap energy, indicates that the emission is no longer primarily from exciton recombination in the QD cores.

4.5 Single QD NP Emission Spectra

The emission spectra in Figures 4.3 and 4.4 show that small ensembles of CO_2 laser-heated QD NPs emit over a wide wavelength range, extending from the pump wavelength to at least the near IR. There are clear maxima in the spectra, independent of the QD size, suggesting that there are at least three main emission features. One obvious

question is whether the complex emission spectra simply result from heterogeneity in the ensemble of CO_2 laser-heated NPs, or if each QD supports emission from many states.

Figure 4.5 shows one approach to answering this problem. After completing the CO_2 laser brightening experiment on the small ensemble of red QD NPs (Figure 4.5A), the emission of the ensemble was studied with 445 nm excitation as NPs were selectively ejected from the ensemble. In the following, the axial component of the secular frequency is denoted f_z. Figure 4.5A shows the f_z spectrum of the ensemble, obtained by monitoring PL while applying a 250 mV sinusoidal drive potential to one of the trap endcap electrodes, sweeping the frequency from 20 kHz to 1 kHz. Dips in the PL signal are expected when f_{drive} is resonant with f_z for one or more of the NPs. In this case, the dips at 7.5, 9.5, 11, and 12 kHz indicate there were NPs with *M/Q* around ~180, ~140, ~120, and ~110 kDa/e. The breath of some of the resonances suggests that more than one NP contributes to some of these features, and based on the signal changes during the ejection experiment, we estimate that the initial ensemble contained 6 - 8 NPs. The corresponding emission spectrum, identical to that in Figure 4.4A) is shown in Figure 4.5F (A).

Frames B-E of the figure show the f_z spectra as NPs were selectively ejected from the trap, working from the high f_z (low *M/Q*) end of the spectrum. Frame B shows the f_z spectrum obtained after high drive potential was applied at 12 kHz, ejecting the NPs giving rise to both the 11 kHz and 12 kHz f_z resonances. The associated emission spectrum is shown in Panel F of the figure, labeled "B". At this point, only two features remained in the f_z spectrum, however, from the breath of the feature at ~9 kHz, we suspected that more than one NP was contributing. Frame C and the spectrum labeled

"C" in frame F, show the result of applying a 9.5 kHz drive signal for 3 s, starting with 1 V amplitude, and then increasing the amplitude in 500mV steps until an irreversible decrease in emission intensity signaled that one or more NP had been ejected. This process was then repeated to obtain the f_z spectrum in frame D and emission spectrum labeled "D," and then again to obtain the f_z spectrum in frame E and emission spectrum labeled "E." Note that as NPs were selectively ejected, the relative intensity of the 9 kHz feature progressively decreased and its width narrowed. It can be seen that the final single NP emission spectrum is, apart from intensity, almost identical to the emission spectrum of the initial ensemble, demonstrating that a single NP can support emission from many different states.

The approximate numbers of NPs remaining in the trap at each stage of the ejection process were estimated from the PL intensity changes, however, the fact that there only a single NP remained that at the end is unambiguous. The f_z spectrum (analogous to frame E) was recorded repeatedly as the NP was excited by the PL pump laser for ~16 h. Figure 4.6 in the supporting information shows how f_z for this NP changed with time, as the NP underwent a series of charge-changing collisions with Ar^+, Ar^* metastables, or electrons. The trapping conditions were changed somewhat from those used for Figure 4.5, resulting in a higher f_z and a narrower f_z resonance. If the trap had contained more than one NP, which by coincidence happened to have nearly identical f_z at the start of the experiment, this would have resulted in development of multiple resonances as the NPs changed charge. From the step sizes the absolute charge, *Q*, can be determined (integers indicated on the figure), and then the absolute mass (3.26 MDa) is easily obtained using the method described in Chapter 3. The ~10% change in apparent

mass over the 16 h is attributed mostly to slow mass loss due to heating by the PL laser, although we cannot rule out a contribution from drift in the trapping conditions, because the rf generator used in these experiments was not stabilized. Nonetheless, 10% mass accuracy is still far better than the factor of ~2 mass spread of the stock QDs, which only allows us to say that the NP was an aggregate containing 4 to 7 QDs, with a charge between +3e and +6e per QD at the beginning of the observation time.

The fact that this final NP was an aggregate is not surprising, because the ejection process selectively retained the NP with the highest *M/Q* (180kDa/e). This, however, obviously raises the question of whether the ability of this single NP to support emission from many different states is simply a function of it being an aggregate. The answer is "no," as shown by several experiments. First, by examining the differences between the spectra taken at different steps in the ejection process, it is possible to see what the spectra look like for each of the ejected NPs, as shown in panel G of Figure 4.5, which compares the emission spectrum of the final aggregate NP ('E: 1 NP') with the difference spectra, or, the spectra of the ejected NPs. It is clear that the emission spectra have hardly any dependence on *M/Q*. For example, the A-B difference spectrum, for two NPs with *M/Q* = 110 and 120 kDa/e, is quite similar to the spectrum for the final *M/Q* = 180kDa/e aggregate. While there are small variations in the relative intensities emitted in the different wavelength ranges, all the difference spectra are qualitatively similar.

A more definitive answer is provided in Figure 4.7, which shows the emission spectra for what are clearly monomeric QDs. This experiment was done using a different approach, where short pulses of red QD NPs were injected into the trap with both the CO_2 laser and 532 nm PL laser on, so that brightening would occur immediately. As soon

as emission signal was observed, the CO_2 laser was turned off, and the secular frequency spectrum was measured to verify that only a single NP was trapped. The emission spectrum was measured, and then charge stepping was monitored in order to determine the mass and charge. In addition, for these experiments, several additional filters were used to improve the spectral resolution.

Emission spectra are shown for two monomers, the first with mass of 595 kDa with +18e charge, and the second with 740 kDa mass with +14e charge. From the reported ~±10% diameter distribution of the stock red QDs used in this experiment monomers, we can estimate that the mass range for QD monomers should be ~460 kDa to ~860 kDa. The 595 kDa particle is, therefore, clearly a monomer. The 740 kDa particle could conceivably be a dimer of two monomers that both happened to be at the extreme, small end of the stock size distribution, however, it is much more likely that this, too, is a monomer. In both cases, the spectra show three clear emission features, with near-zero intensity in between. One feature is to blue of the excitonic emission (650 nm for these QD - Figure 4.3A), one peaks between 720 and 775 nm, and the final feature is in the near IR, probably peaking beyond the sensitivity range of our APD.
For reference, the bulk band gap of CdSe at 300 K is 1.74 eV,[20] corresponding to emission at 713 nm. The two spectra are quite similar, and are also similar to the ensemble spectrum (Figure 4.3A) for NPs prepared from this size QD.

We cannot rule out the possibility that NPs that are aggregates of QDs might become hot enough under laser heating to partially or completely fuse, forming a particle with larger effective diameter. Note, however, that the emission spectra after heating/brightening do not appear to depend on QD diameter (Figures 4.3 and 4.4), are

similar for aggregate NPs (Figure 4.5) and QD monomers (Figure 4.7), and all have features well to the red of even bulk CdSe bandgap emission. Therefore, we conclude that fusion to form larger particles is not responsible for the emission red shift, and conversely, the emission spectra would probably not be sensitive to fusion.

Another obvious question is whether the near IR emission observed for all the QD NPs at both pump wavelengths is really PL, or if it could be partially or entirely thermal emission due to heating of the NPs by the PL pump laser. To investigate this issue, a single NP formed by ESI of red QDs was trapped and monitored with 532 nm excitation, and the charge-stepping procedure was used to determine that its mass was 1.76 MDa, and that it had charge, Q = +23e at the beginning the series of charge steps. From the mass, this NP is an aggregate, probably a trimer. The emission spectrum was then measured repeatedly, varying both the 532 nm laser intensity and the argon pressure, looking for any increase in near IR emission under conditions where the QD aggregate would tend to be hotter (high laser power, low buffer gas intensity). As might be expected, no change was seen. The fact that the QD aggregate was stable over the course of the hour needed to measure six emission spectra implies that the particle temperature must have remained well below the sublimation temperature. The bulk sublimation temperature for ZnS is 1450 K[21] and CdSe melts and decomposes at ~1540 K,[22] however, the vaporization temperature should be significantly lower for small particles in vacuum. For example, electron microscopy experiments[23] showed sublimation of CdSe/CdS nanostructures on the hour time scale, at temperatures of only ~873K. In this temperature range, less than 10^{-4} of the radiated power is at wavelengths below 1000 nm, and a single NP would emit only ~500 photons/s in the <1000 nm range, assuming that emissivity of

1.0. In reality, subwavelength diameter particles have emissivity's well below unity,[24-28] and the thermal emission rate for $\lambda < 1000$ nm would be too small to detect, given the ~1% efficiency of our photon detection system. The NP temperature is discussed further below.

4.6 Photoluminescence Before and After Heating

The results of these experiments show that ensembles of unheated, charged NPs in the gas phase show excitonic emission spectra, similar to those for the same NPs in methanol solution, but with much lower intensity. Upon heating, the emission brightens substantially, but the spectra no longer look excitonic. One question is whether the low emission signal for as-trapped NPs results from low PL quantum yields (QY), from small absorption cross-sections, or from some combination of both factors. It is useful to consider two limiting cases.

First, consider the case where the absorption cross section (σ_{abs}) is assumed to be similar to that for the same QDs in solution. Solution phase σ_{abs} values have been reported in the literature for a variety of QDs excited over a wide range of wavelengths.[29-32] For the QDs and pump wavelengths used here, the solution phase absorption cross sections would be in the range between ~2 x 10^{-15} cm^2 (Green QDs pumped at 532 nm) and ~1 x 10^{-14} cm^2 (Red QDs pumped at 445 nm).

Consider the ensemble spectrum of red QD NPs pumped at 445 nm (Figure 4.4A). The selective ejection experiments outlined in Figure 4.5 allow us to estimate that there were ~6 to 8 NPs in the trap. From the emission measured before CO_2 laser exposure, we can estimate, taking the light detection efficiency into account, that the average

emission/NP in the unheated NP ensemble was ~8700 photons/s at 125 W/cm^2 of 445 nm pump intensity. At least some of the NPs in this ensemble were aggregates, and for the purpose of estimating σ_{abs}, we will assume that the average aggregate size was 3 QDs. For the unheated NPs, we might expect that σ_{abs} for such a particle might lie between one and three times the cross section for a red QD monomer at 445 nm (*i.e.*, ~10^{-14} cm^2). Such NPs would absorb ~3 x 10^6 photons/sec/NP, thus the ~8700 photon/sec/NP emission level would imply a PL QY of only 0.3%. If, instead, we assume that QY = 1, then σ_{abs} would need to be ~0.3% of the solution phase value, or ~3 x 10^{-17} cm^2.

4.7 Thermal Balance in Gas-Phase QD NPs Under Visible Laser Excitation

Thermal considerations allow us to set a maximum on the magnitude of σ_{abs} for the as-trapped NPs. Consider the limit where the as-trapped QD NPs have σ_{abs} equivalent to those measured in solution, with small QY. The highest absorption cross section would be for red QD NPs pumped at 445 nm (solution $\sigma_{abs} \approx 1 \times 10^{-14}$ cm^2),[32] and for 125 W/cm^2 laser intensity (conditions of Figure 4.4A), the absorption rate would be ~2.8 x 10^6 photons/s, giving rise to a heating rate of ~8 x 10^6 eV/s = ~1.2 x 10^{-12} W. At the other extreme, yellow QD NPs under the conditions of Figure 4.3C, which were pumped by 180 W/cm^2 of 532 nm (solution σ_{abs} ~2x10^{-15} cm^2), would absorb ~1x10^6 photons/s, corresponding to a heating rate of 2.2 x 10^6 eV/s, or 3.6 x10^{-13} W.

The NP temperature is determined by the balance between the heating rate and the sum of all cooling processes, including photoluminescence, thermionic emission of electrons, evaporation, thermal emission of photons, and buffer gas collisions. Because

the emission QY is assumed to be low in this scenario, the photoluminescence cooling is negligible, and the fact that the charge/NP does not increase rapidly during the experiments shows that thermionic emission of electrons is also negligible from a cooling perspective. For any reasonable estimate of the enthalpy of sublimation (for example, ΔH_{subl}=321.7 kJ/mol for bulk CdSe = ~3.3 eV/atom)[33] many thousands of atoms would have to sublime *per* s to contribute significantly to cooling, but the actual sublimation rates under conditions used here are less than 1% of the NP mass per hour (Figure 4.6), corresponding to ≤ 0.1 atom/s. The only significant cooling mechanisms are buffer gas collisions and thermal photon emission.

The flux-weighted energy transfer per buffer gas collision is $2k(T_{surface}-T_{gas})\cdot c_A$, where $T_{surface}$ is the NP surface temperature, T_{gas} is 300 K, and c_A is the energy accommodation coefficient (a measure of inelasticity). Energy accommodation in collisions of argon with surfaces is expected to be reasonably efficient. For example, the accommodation coefficient for Ar colliding with a heated tungsten surface is ~0.25,[34] and it should be larger for collisions with ZnS because the surface atom masses are lower.[35] From the perspective of the as-trapped NPs, collisions would be with the ligand layer, and based on scattering measurements for Ar from organic surfaces,[36, 37] c_A for 300 K Ar should be close to unity. Accommodation for helium is expected to be lower; however, the collision rates for a given pressure are also higher. The total collision rate, and therefore, the cooling power is linear with buffer gas pressure. Figure 4.8A shows the collisional cooling power (W/NP) as a function of $T_{surface}$, calculated for a 7.5 nm diameter spherical NP in 6, 10 and 60 mTorr of Ar and He, assuming c_A = 1 and 0.2, respectively.

The cooling rate from thermal emission of photons can be estimated from the Stefan-Boltzmann law: $P(W/m^2) = \sigma\epsilon(T_{surface}^4 - T_{gas}^4)$, where σ is the Stefan-Boltzmann constant and ϵ is the emissivity. Subwavelength diameter particles have emissivities well below unity.[24-28] Figure 4.8B plots the cooling power as a function of $T_{surface}$ for $\epsilon = 0.01$, 0.05, and 0.1, covering the range expected for 5 – 10 nm NPs. It can be seen that for low temperatures, collisional cooling dominates, but for high temperatures, radiative cooling becomes increasingly important. Figure 4.8C gives the sum of the collisional and thermal photon cooling rates for Ar at 6 and 60 mTorr pressure, assuming $\epsilon = 0.01$ and 0.1, covering the ranges relevant to our experiments.

4.8 Thermal Constraints on σ_{abs} for QD NPs Before and After Heating

With this understanding of the thermal balance in QD NPs under laser irradiation, it is possible to put some limits on the magnitude of σ_{abs}. If we assume solution-like σ_{abs} for the as-trapped NPs, the heating rate for red QD NPs pumped by 125 W/cm^2 of 445 nm radiation in 20 mTorr of Ar (the conditions of Figure 4.4A) is 1.2×10^{-12} W. The total cooling rate only matches the heating rate at temperatures between ~1030 K (assuming $\epsilon = 0.1$) and ~1800 K ($\epsilon = 0.01$). For yellow QD NPs pumped with 180 W of 532 nm in 10 mTorr Ar pressure (conditions of Figure 4.3C – 3.6×10^{-13} W), the steady state temperature would be between 720 and 1170 K, depending on the value assumed for ϵ. As already noted, CdSe nanostructures were observed by TEM to sublime on a much faster time scale than ours, at temperatures as low as 773 K. Furthermore, the mercaptoundecenoic acid surface layer would desorb or pyrolyze at even lower temperatures. Therefore, the observation that as-trapped NPs have solution-like emission

spectra that are stable for at least 20 m of continuous excitation, and that the sublimation rates are less than 0.1 atom/s, indicates that the NPs are not reaching even the lower range of the predicted temperatures.

Therefore, we conclude that σ_{abs} for the as-trapped QD NPs must be significantly smaller than typical solution phase cross sections. Presumably this factor also at least partially accounts for the weak emission observed. The actual σ_{abs} value must be small enough that the NPs do not reach temperatures that result in creation of surface (or core) defects that would significantly change the absorption/emission properties. It is not clear what temperature might be required to damage a thiol ligand layer on ZnS, but there is considerable information on the analogous gold thiol systems, and there is a theoretical prediction[38] that the $S_{thiolate}$-Au and $S_{thiolate}$-ZnS bonds should have similar energies. Lavrich *et al.*[39] used thermal desorption in vacuum to study a variety of alkanethiols on Au(111), and found that chemisorbed molecules began to desorb around 450 K, with desorption peaking near 480 K, with corresponding desorption energies around 1.3 eV, independent of chain length. A similar study using mass spectrometric detection for cyclopentanethiol on Au(111) observed decomposition products starting ~400 K, peaking near 440 K,[40] with masses suggesting that the C-$S_{thiolate}$ bond had broken. These experiments used heating rates of 2 and 1 K/sec, and therefore observed changes only when the desorption/decomposition time scale was shorter than ~20 s. Our experiment requires that the NPs be stable on a ~1000 s time scale. Zhao *et al.*[11] reported a study of thermal effects on PL of CdSe/CdS/ZnS core/shell/shell QDs in solution and polymer matrices, and found that PL intensity was irreversibly lost by ~423 K in solution, but that the polymer matrix reduced the temperature effects by preventing ligand loss. Based on

these considerations, 450 K appears to be a safe estimate for the maximum temperature at which the as-trapped NPs might survive for 1000 s without desorption or damage to the ligand layer.

In order to keep red QD NPs below 450 K under the conditions of Figure 4.4A, σ_{abs} would have to be less than ~1.5 to 4 % of the solution cross section, for ϵ assumed to be in the 0.01 to 0.1 range. Similarly, for yellow QD NPs under the conditions for Figure 4.3C, σ_{abs} would have to be less than 16 to 35 % of the solution σ_{abs}, depending on the value assumed for ϵ. In fact, we will argue below that σ_{abs} for the as-trapped QD NPs must be even smaller than these upper limits.

4.9 Comparison of σ_{abs} Before and After Brightening

Further insight regarding the magnitudes of σ_{abs} before and after brightening can be obtained from the experiment shown in Figure 4.9. A small ensemble of red QD NPs was trapped in the dark at 7 mTorr pressure of Ar. The pressure was then raised to 60 mTorr, and the ensemble was exposed to 165 W/cm^2 of 532 nm laser, resulting in a stable, but very low level of emission. The pressure was then decreased slowly, until at ~6 mTorr, an abrupt onset of emission was observed. With the pressure held constant at 6 mTorr, the emission was observed to decay to baseline in ~10 s. At that point, the pressure was again decreased until at 5 mTorr, a second emission burst occurred, and before that had completely decayed, a third was observed while the pressure was still ~5 mTorr. Further decrease in the pressure lead to additional emission bursts at ~3 mTorr and ~2 mTorr, but then no further emission was observed as the pressure dropped to 5 x 10^{-7} Torr. At that point, the pressure was increased to 5 mTorr, and the CO_2 laser was

focused through the trap at ~1 kW/cm^2, leading to a final, short-lived burst of emission.

Our interpretation of this experiment is as follows. As discussed in conjunction with Figure 4.3C, emission from gas-phase QD NPs can be brightened by heating using either visible or CO_2 laser irradiation. As discussed above, however, as-trapped QD NPs have small σ_{abs}, such that at the high initial pressure, collisional cooling was sufficient to keep the NPs below the temperature required to drive the brightening process ($T_{brighten}$). As the pressure was decreased, the temperature of the NPs increased, but because the ensemble included QDs with a distribution of sizes and spectral properties, the temperature rise would have been different for each NP. At pressures down to 6 mTorr, collisional cooling was sufficient to prevent any of the NPs from reaching $T_{brighten}$. If, as discussed above, if we assume this temperature to be 450 K, then we can put an upper limit on σ_{abs} (for the NP that absorbed most strongly), of between 1 to 3 x 10^{-16} cm^2 (for ϵ = 0.01 and 0.1). That is less than a tenth of the estimated solution σ_{abs} for red QD NPs pumped at 532 nm (~4 x 10^{-15} cm^2).[32]

At this point one of the NPs reached $T_{brighten}$, leading to a sudden jump in emission, which then bleached within ~10 s. The process was repeated for additional NPs as the pressure continued to drop, as each NP's temperature reached $T_{brighten}$. The fact that there was an additional brightening event upon CO_2 laser irradiation indicates that a few NPs remained in the trap that had not brightened under the influence of the 532 nm laser. These presumably were QD NPs with absorption spectra shifted too far to the blue to significantly absorb at 532 nm, *i.e.*, QDs at the small end of the size distribution. The CO_2 laser is evidently able to heat such NPs, leading to brightening, and then very rapid bleaching.

The bleaching process for gas-phase QDs pumped at 532 nm has been studied previously.[5] In those experiments, a single green CdSe/ZnS QD was trapped, and its mass and emission intensity were monitored continuously as the particle was laser heated (at 532 nm) to drive slow sublimation over the course of several days. Periodically, the 532 nm power was lowered to allow measurement of emission intensity and spectra at a laser intensity where the particle mass was stable. It was found that the emission spectrum was quite stable even as the particle lost up to 85% of its initial mass, and that emission intensity varied roughly as $M^{2/3}$, *i.e.*, as the surface area. The conclusion was that visible laser bleaching is simply due to sublimation, and if QDs are kept below the sublimation point, they exhibit emission that is stable indefinitely. In Figure 4.9, the combination of low buffer pressure and high 532 nm intensity resulted in rapid sublimation.

Knowing this, we can interpret the abrupt increase in emission and rapid bleaching to learn about changes that must be occurring in the σ_{abs}. As already noted, the fact that modest buffer gas pressures are sufficient to keep the NP temperature below $T_{brighten}$, implies that σ_{abs} for the as-trapped NPs must be small – between 1 and 3 x 10^{-16} cm^2. The abrupt brightening of emission when the temperature reached $T_{brighten}$ could be due to an increase in σ_{abs}, an increase in the emission QY, or some combination of the two. If only the QY increased, that would cool the NPs by radiating away a larger fraction of the absorbed photon energy, and in that case the NPs would be stable. Instead, the brightened QD NPs rapidly sublime, indicating that the temperature must increase substantially when the NPs brighten, implying that σ_{abs} must increase substantially. We can roughly estimate how hot the NPs must get to sublime within 10 s,

based on the observation[23] that 40 nm CdSe/CdS octopods (with surface area/volume ratios similar to our QD NPs) sublime in ~500 s at 873 K. If we assume that the sublimation rate is exponential in temperature, then the temperature required to drive sublimation 50 times faster is:

$$T = (873^{-1} - k/E_{subl} \cdot \ln(50))^{-1} \quad (4.1)$$

where k is the Boltzmann constant, and E_{subl} is the sublimation energy per atom. If we assume the bulk heat of sublimation of CdSe (3.3 eV),[33] T would need to be ~950 K, and if a lower heat of sublimation is assumed for NPs, then the temperature would need to be higher (such as E_{subl} = 2.5 eV gives T = 990K). The value of σ_{abs} required to reach 950 K under these conditions (6 mTorr, 165 W, 532 nm) would be between ~0.85 and 5 x 10^{-15} cm^2, for ϵ between 0.01 and 0.1. 990K would require a cross section between ~1 and 7 x 10^{-15} cm^2, compared to the *upper limit* on σ_{abs} before brightening, of 1 to 3 x 10^{-16} cm^2. The increase is at least an order of magnitude.

This increase in σ_{abs} also explains why brightening is so abrupt. As the NP begins to brighten, σ_{abs} increases, which leads to further increase in temperature, which further increases σ_{abs}, *etc.*, until a new steady state is established with high σ_{abs}, brighter PL, and NP temperature high enough to drive rapid sublimation. As shown in Figure 4.3A, the total PL intensity in the wavelength range below 1000 nm increased by a factor of ~55 for red QD NPs at 532 nm, thus, it is possible that the brightening can be entirely attributed to an increase in σ_{abs}, although it is seems more likely that both absorption and emission would be affected by changes to the QD NPs.

4.10 Why σ_{abs} Is Small in the As-Trapped State

Thermal considerations indicate that σ_{abs} for as-trapped QD NPs is considerably smaller than for the same QDs in solution, and the question is why. Important evidence is provided by the dependence on QD size and pump laser wavelength, of the brightening factor, *i.e.*, the factor by which the emission brightens when the NPs are heated. The inset to Figure 4.10 shows the absorption spectra measured for green and red QD NPs diluted 1:100 in methanol (*i.e.*, our ESI solutions). The main figure shows the brightening factors, plotted as a function of the energy difference between the laser and absorption onset wavelengths, $\Delta E_{p\text{-}o}$. Brightening factors are shown for all QD/laser combinations in Figures 4.3 and 4.4, with the exception of green QD NPs pumped at 532 nm, where the unbrightened PL intensity was zero, corresponding to infinite brightening factor.

The near-exponential dependence of the brightening factor on $\Delta E_{p\text{-}o}$, as well as the smallness of σ_{abs} for unbrightened QD NPs, suggests that the low energy portion of the absorption spectra for the as-trapped NPs is bleached, such that the absorption onset energy is blue-shifted by ~0.2 to 0.3 eV compared to the solution phase onset. The onset wavelength for as-trapped green QD NPs would be shifted to ~520 nm (~580 nm in solution), explaining why the 532 nm laser could not excite PL (brightening factor = ∞). With increasing QD size, the absorption spectra shift to the red. For the yellow QDs, the solution phase absorption onset is at ~600 nm, but the proposed bleaching would shift this to 535 nm, such that the 532 nm laser would excite as-trapped yellow QD NPs, but very weakly (brightening factor = 1800). The orange QDs have an onset at ~630 nm in solution, shifting to ~560 in the gas phase, resulting in somewhat stronger excitation of the as-trapped QD NPs, and a brightening factor of 160. The red QDs would have an as-

trapped absorption onset at ~590 nm (650 nm in solution), and the expected stronger absorption at 532 nm explains why the brightening factor was only 55. The 445 nm pump laser would be well above the bleached spectral region for all the QDs, explaining why the brightening factors were only to 6 (green QD NPs) and 4 (red QD NPs).

The QDs examined in this study are capped with mercaptoundecenoic acid, in a Na^+-containing buffer solution with pH of ~8, *i.e.*, the acid groups should be mostly ionized, with the carboxylate negative charge balanced by Na^+. From typical ligand packing densities[41] we would expect ~50 ligands/QD. This solution was diluted in methanol and electrosprayed, producing QD NPs in the gas phase with positive charge of 5e to 15e per NP. Under these conditions, the positive charge should almost entirely be due to excess Na^+, which we might expect to be mostly on the exterior of the ligand layer, complexed to carboxylate groups. Na^+ cations (recombination energy 5.1 eV[42]) located on the exterior of the ligand layer, at some distance from the surface of ZnS (work function ≈ 7.0 eV[43]) are unlikely to extract electrons from the semiconductor NP. In essence, however, the shell of excess cations establishes a positive potential on the semiconductor NP, which may result in attraction of electrons during the ESI process (counterbalanced by more Na^+). Excess electrons on the semiconductor NP would be most stable in the CdSe core, and thus would tend to populate states at the bottom of the conduction band. These excess electrons would block photoexcitation to the bottom of the conduction band,[13, 15, 16, 44] bleaching the low energy portion of the absorption spectra.

This scenario also is consistent with the observation that the PL spectrum for the as-trapped NPs looks excitonic. There would always be electrons at the bottom of the conduction band, therefore whenever a hole is created in the valence band by

photoexcitation, emission at the band-gap energy can occur. Indeed, one might expect that the PL quantum yield should be quite high. In that case, the low PL intensities for as-trapped QD NPs would require that σ_{abs} must be even smaller than implied by thermal consideration – well below 1% of the solution σ_{abs} for 532 nm excitation.

4.11 The Nature of the Brightened State

After heating, the emission spectrum is broad, with most of the intensity in three main features peaking near 550 nm, near 650 - 750 nm, and in the near-IR. The thermally brightened emission is similar for QD monomers, small QD aggregates, and ensembles of QD NPs, and also similar for heating by irradiation in the IR or visible. The most easily created damage involves desorption/decomposition of the ligand layer, which creates a variety of surface defect sites.[10-12, 45] In the condensed phase, surface sites tend to act as carrier traps, reducing the QY, but also give rise to interband emissive states, some of which are at energies below the band gap. Further evidence suggesting that emission is from surface states was provided by a previous experiment in which a single small QD aggregate was monitored over ~100 h as it was heated to drive slow sublimation, resulting in ~80% mass loss.[5] Periodically during the sublimation process, heating was interrupted to allow measurement of emission spectra, which were found to be nearly independent of the mass loss, and similar to those observed here, and with intensity roughly proportional to the surface area of the NP.

For our Na^+-charged QDs, we cannot rule out the possibility of some charge loss during desorption/decomposition of the ligand layer, however, we know that the final, brightened QD NPs still have 5 to 15 charges. In this final state, without an intact ligand

layer isolating the charges from the surface, it may be that combination of positive charges on the surface and deep surface trap states is able to extract the extra electrons out of core and trap them, depopulating the conduction band, and leading to full or partial reversal of the absorption bleaching. If the conduction band is completely depopulated, then σ_{abs} might be expected to be similar to that for QDs in solution. If that is true, we can use the emission intensity measured for the QD monomers (Figure 4.7) to estimate the emission QY. For both those examples, the QY is ~9%, *i.e.*, well below unity as might be expected for emission from defect states.

Rowland and Shaller[10] reported a study which provides an interesting point of comparison for these results. They deposited octadecylamine-capped CdSe and CdSe/ZnS QDs on glass slides and then annealed them to various temperatures in a vacuum oven, examining the room temperature PL between each annealing step. For the CdSe QDs, irreversible changes (red shift, and loss of PL intensity) were observed at 400K, *i.e.*, in the range where ligand loss/decomposition is expected to become significant. For CdSe/ZnS QDs, however, irreversible loss of PL was not seen below ~700 K, which is well above the temperature where the ligand layer would have desorbed/decomposed. Their result shows that the ZnS shell effectively isolated the CdSe core from the effects of changes to the ZnS surface. The situation is clearly different in our experiment, however, because our QD NPs initially have extremely low PL intensity, due to bleaching of σ_{abs} due to electrons populating states near the conduction band minimum. After heating, the emission increases substantially due to the increase in σ_{abs}, but the QY is still well below unity.

4.12 Conclusion

The PL dynamics of charged QDs in the gas phase is complex, but by taking both the emission behavior, and the thermal considerations into account, we have been able to deduce the following:

1. From thermal considerations, it is clear that σ_{abs} must be no more than ~10% of the solution phase σ_{abs} in order that the QD NPs not heat to the point of damage.
2. The emission in the unheated state is excitonic, and if our explanation for the weakness of the emission (bleaching of the absorption) is correct, then the emission QY should be near unity, because there are excess electrons in the conduction band available to fill the valence band hole.
3. If the assumption of near-unit QY is correct, then this implies that σ_{abs} for the unheated QD NPs is, in fact, less than 1% of the solution σ_{abs}.
4. The emission after brightening is not excitonic, and includes states with energies both higher and lower than the band gap, suggesting that heating creates a wide variety of defect states, such as surface states, which have nonzero emission QY. Some of these emitting states have energies much smaller than the band gap energy.
5. The much brighter emission after heating suggests that the population of extra conduction band electrons, which bleached σ_{abs} for the unheated NPs, is trapped by lower energy surface states, depopulating the conduction band and reversing the bleaching of σ_{abs}.
6. If we assume that σ_{abs} after heating is equal to the solution phase σ_{abs}, we can estimate that the total QY for emission from the diverse range of emitting states

ranges from 0.5% to 9%, depending on QD size and excitation wavelength.

Our ultimate interest in QD NPs in the gas phase is for use as noncontact probe particles, allowing us to indirectly track the mass of a nonemitting particle cotrapped with the probe. The QD NPs appear to be excellent prospects for this purpose, because they have reasonably bright, nonblinking, nonbleaching emission that is stable for days of continuous monitoring,[5] provided only that the visible laser intensity be low enough to prevent sublimation. In addition, however, the gas phase experiments provide a unique perspective on the effects of charge and heating on the photophysics of QDs.

4.13 References

1. S. Schlemmer, J. Illemann, S. Wellert, and D. Gerlich, J. Appl. Phys. **90** (10), 5410-5418 (2001).
2. A. J. Trevitt, P. J. Wearne, and E. J. Bieske, Int. J. Mass Spectrom. **262** (3), 241-246 (2007).
3. W. P. Peng, Y. Cai, Y. T. Lee, and H. C. Chang, Int. J. Mass Spectrom. **229** (1-2), 67-76 (2003).
4. Y. Cai, W. P. Peng, and H. C. Chang, Anal. Chem. **75** (8), 1805-1811 (2003).
5. D. M. Bell, C. R. Howder, R. C. Johnson, and S. L. Anderson, ACS Nano **8**, 2387–2398 (2014).
6. V. Lesnyak, N. Gaponik, and A. Eychmuller, Chem. Soc. Rev. **42**, 2905--2929 (2013).
7. A. M. Smith and S. Nie, Acc. Chem. Res. **43** (2), 190 - 200 (2010).
8. M. Nirmal and L. Brus, Acc. Chem. Res. **32** (5), 407-414 (1999).
9. W. Xiong, D. D. Hickstein, K. J. Schnitzenbaumer, J. L. Ellis, B. B. Palm, K. E. Keister, C. Ding, L. Miaja-Avila, G. Dukovic, J. L. Jimenez, M. M. Murnane, and H. C. Kapteyn, Nano Lett. **13**, 2924−2930 (2013).
10. C. E. Rowland and R. D. Schaller, J. Phys. Chem. C **117** (33), 17337-17343 (2013).

11. Y. Zhao, C. Riemersma, F. Pietra, R. Koole, C. M. Donega, and A. Meijerink, ACS Nano **6** (10), 9058-9067 (2012).

12. C. Bullen and P. Mulvaney, Langmuir **22** (7), 3007 - 3013 (2006).

13. P. Guyot-Sionnest, Microchimica Acta **160** (3), 309-314 (2008).

14. C. Galland, Y. Ghosh, A. Steinbruck, M. Sykora, J. A. Hollingsworth, V. I. Klimov, and H. Htoon, Nature **479** (7372), 203 - 208 (2011).

15. J. D. Rinehart, A. M. Schimpf, A. L. Weaver, A. W. Cohn, and D. R. Gamelin, J. Amer. Chem. Soc. **135** (50), 18782−18785 (2013).

16. D. Mocatta, G. Cohen, J. Schattner, O. Millo, E. Rabani, and U. Banin, Science **332** (77), 77 - 81 (2011).

17. M. Shim, C. Wang, David J. Norris, and P. Guyot-Sionnest, MRS Bulletin **26** (12), 1005 - 1008 (2001).

18. S. Gupta, S. V. Kershaw, and A. L. Rogach, Adv. Materials **25** (48), 6923-6944 (2013).

19. S. E. Yalcin, J. A. Labastide, D. L. Sowle, and M. D. Barnes, Nano Lett. **11**, 4425–4430 (2011).

20. C. Kittel, *Introduction to Solid State Physics*. (John Wiley, New York, 1986).

21. Zinc Sulfide, Ipcs International Programme on Chemical Safety. http://www.inchem.org/documents/icsc/icsc/eics1627.htm.

22. Cadmium Selenide (CdSe) Debye Temperature, Heat Capacity, Density, Melting Point, Hardness. In II-VI and I-VII Compounds; Semimagnetic Compounds; O. Madelung, U. Rössler, M. Schulz, Eds. Springer: Berlin, 1999; Vol. 41B, pp 1-3.

23. B. Goris, M. A. Van Huis, S. Bals, H. W. Zandbergen, L. Manna and G. Van Tendeloo, Small **8**, 937-942 (2012).

24. H. C. van de Hulsst, *Light Scattering by Small Particles*. (Dover, New York, 1981).

25. C. F. Bohren and D. R. Huffman, *Absorption and Scattering of Light by Small Particles*. (Wiley, New York, 1983).

26. L. Landstrom, K. Elihn, M. Boman, C. G. Granqvist, and P. Heszler, Appl. Phys. A **81**, 827-833 (2005).

27. L. Landstrom and P. Heszler, J. Phys. Chem. B **108**, 6216-6221 (2004).

28. P. Roura and J. Costa, Eur. J. Phys. **23**, 191-203 (2002).

29. W. W. Yu, L. Qu, W. Guo, and X. Peng, Chem. Mater. **15**, 2854-2860 (2003).

30. J. Jasieniak, L. Smith, J. v. Embden, P. Mulvaney, and M. Califano, J. Phys. Chem. C **113**, 19468-19474 (2009).

31. J. Sun and E. M. Goldys, J. Phys. Chem. C **112**, 926109266 (2008).

32. C. A. Leatherdale, W. K. Woo, F. V. Mikulec, and M. G. Bawendi, J. Phys. Chem. B **106**, 7619-7622 (2002).

33. Cadmium Selenide (CdSe) Thermodynamical Properties, Phase Diagram. In II-VI and I-VII Compounds; Semimagnetic Compounds, O. Madelung, U. Rössler, M. Schulz, Eds. Springer: Berlin, 1999; Vol. 41B, pp 17-34.

34. W. Watt, R. Moreton, and L. G. Carpenter, Surf. Sci. **45**, 238-248 (1974).

35. E. K. Grimmelmann, J. C. Tully, and M. J. Cardillo, J. Chem. Phys. **72**, 1039-1043 (1980).

36. M. E. King, G. M. Nathanson, M. A. Hanning-Lee, and T. K. Minton, Phys. Rev. Letts. **70**, 1026-1029 (1993).

37. W. A. Alexander, J. Zhang, V. J. Murray, G. M. Nathanson, and T. K. Minton, Faraday Discussions **157**, 355-374 (2012).

38. B.-K. Pong, B. L. Trout, and J.Y. Lee, Langmuir **24** (10), 5270-5276 (2008).

39. D. J. Lavrich, S. M. Wetterer, S. L. Bernasek, and G. Scoles, J. Phys. Chem. B **102**, 3456-3465 (1998).

40. H. Kang, Y. Kim, T. Park, J. B. Park, E. Ito, M. Hara, and J. Noh, Bull. Korean Chem. Soc. **32**, 1253-1257 (2011).

41. Y. Zhang, A. M. Schnoes, and A. R. Clapp, Appl. Mat. and Inter. **2** (11), 3384–3395 (2010).

42. S. G. Lias, J. E. Bartmess, J. F. Liebman, J. L. Holmes, R. D. Levin, and W. G. Mallard, Ion Energetics Data.

43. X. Fang, Y. Bando, G. Shen, C. Ye, U. K. Gautam, P. M. F. J. Costa, C. Zhi, C. Tang, and D. Golberg, Adv. Materials **19**, 2593-2596 (2007).

44. M. Shim, C. Wang, and P. Guyot-Sionnest, J. Phys. Chem. B **105** (12), 2369-2373 (2001).

45. O. Voznyy, S. M. Thon, A. H. Ip, and E. H. Sargent, J. Phys. Chem. Lett. **4**, 987−992 (2013).

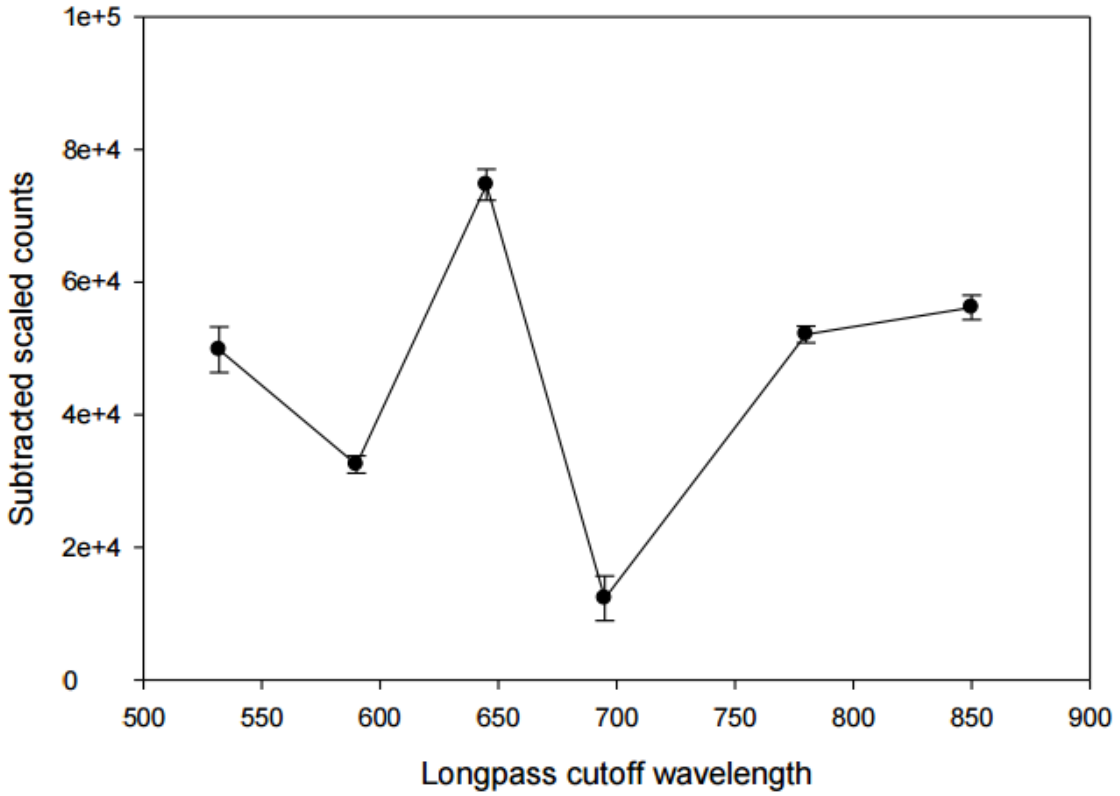

Figure 4.1 – Reproducibility of Emission Spectrum Recording Technique. Spectral reproducibility of the long pass cutoff filter method of measuring an emission spectrum. Three spectra of an ensemble of red QDs were measured in immediate succession. The error bars is the standard deviation of the three spectra.

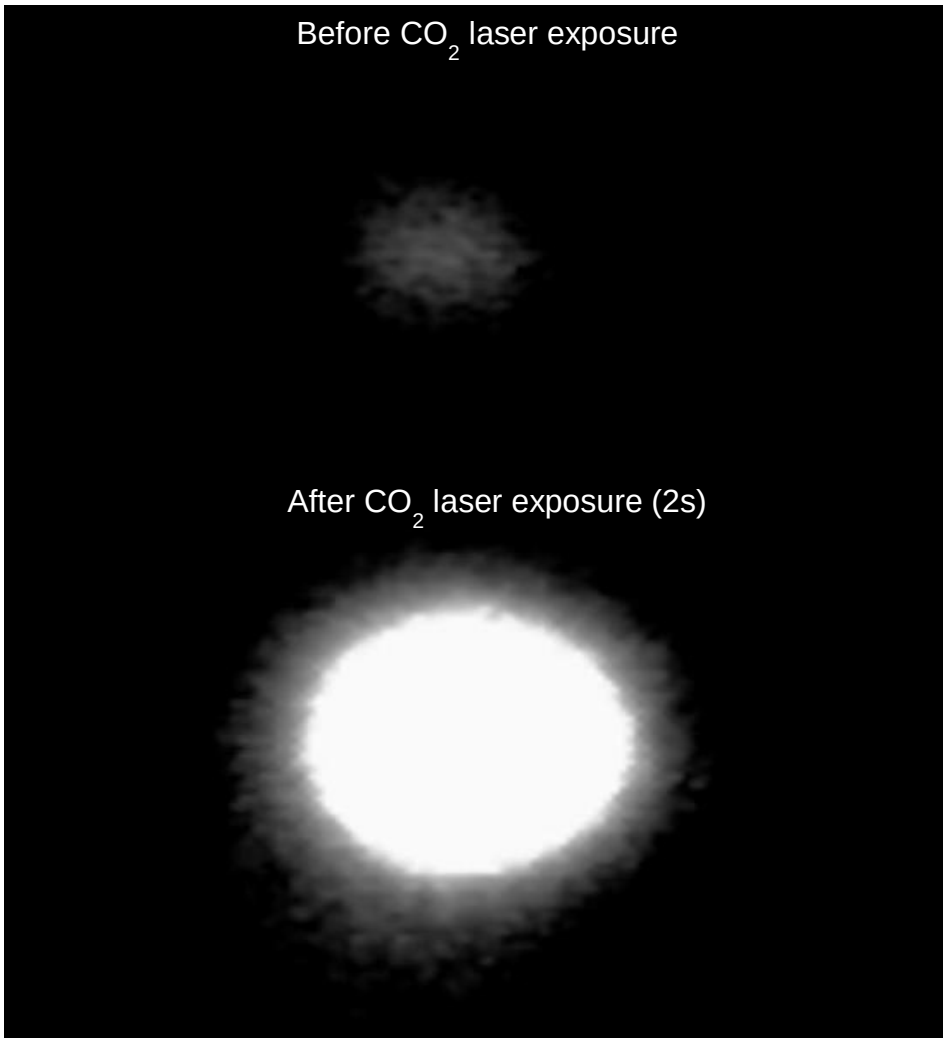

Figure 4.2 – Image of an Ensemble of Trapped QDs Before and After Heating. Images of an ensemble of trapped QD NPs taken before (top) and after (bottom) heating by CO_2 laser irradiation.

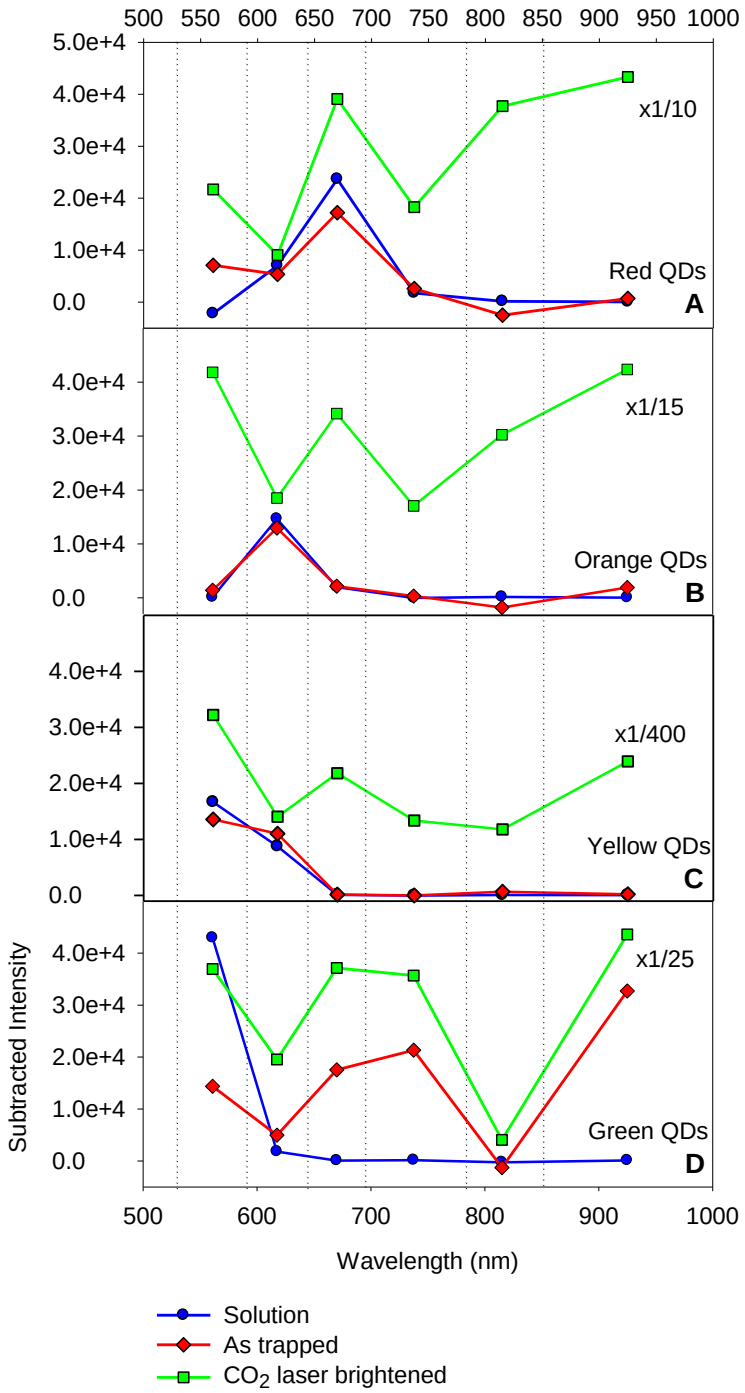

Figure 4.3 – Emission Spectra of QDs Pumped at 532 nm. Emission spectra of ensembles of red (solution λ_{max}=650 nm), orange (solution λ_{max}=605 nm), yellow (solution λ_{max}=575 nm), and green (solution λ_{max}=540 nm) trapped QD NPs pumped at 532 nm before (red) and after (green) heating by CO_2 laser irradiation. Dotted vertical lines are the cutoff wavelengths of the long pass filters used, and the points represent the PL intensity in each wavelength range. Solution phase spectra (blue) measured with the same optical setup are included for comparison.

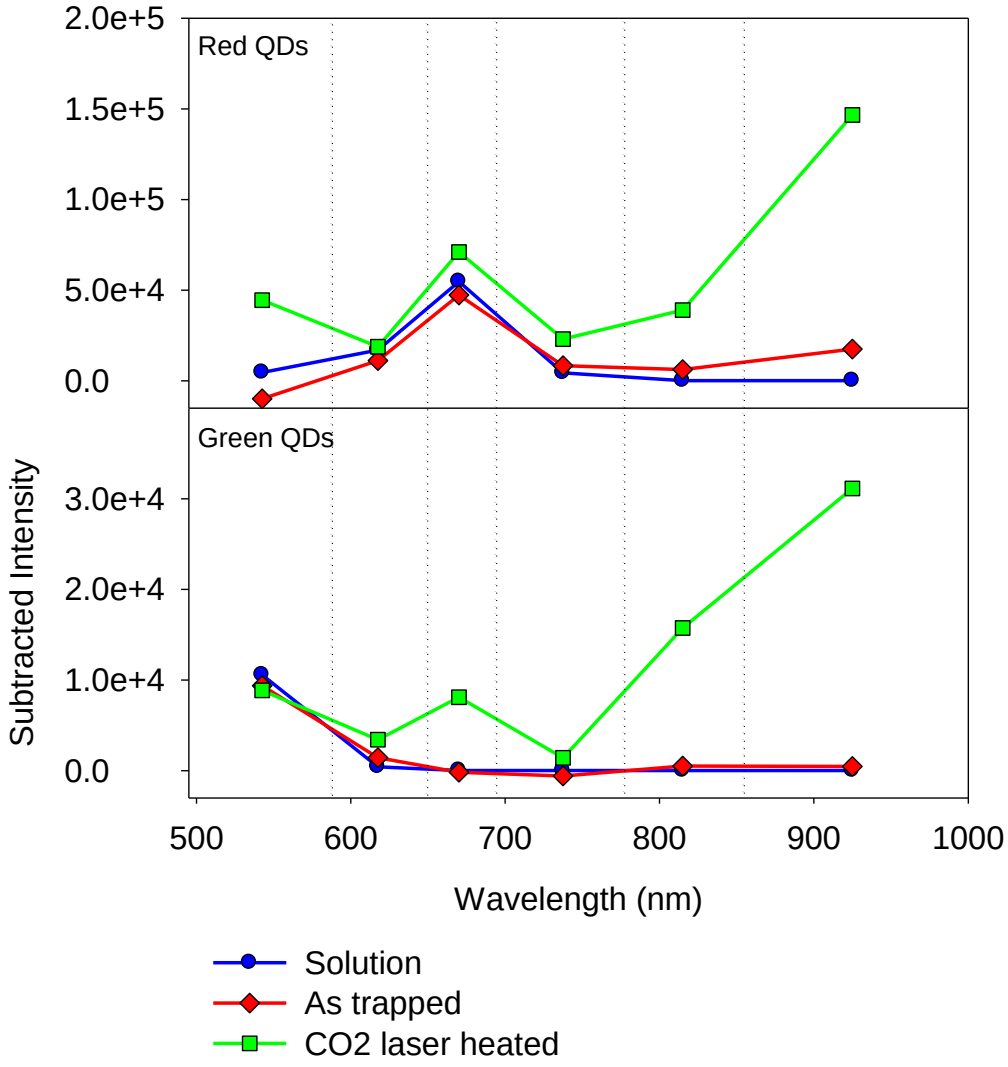

Figure 4.4 – Emission Spectra of QDs Pumped at 445 nm. Emission spectra of ensembles of red (solution λ_{max}=650 nm), and green (solution λ_{max}=540 nm) trapped QD NPs pumped at 532 nm before (red) and after (green) heating by CO_2 laser irradiation. Solution phase spectra (blue) measured with the same optical setup are included for comparison.

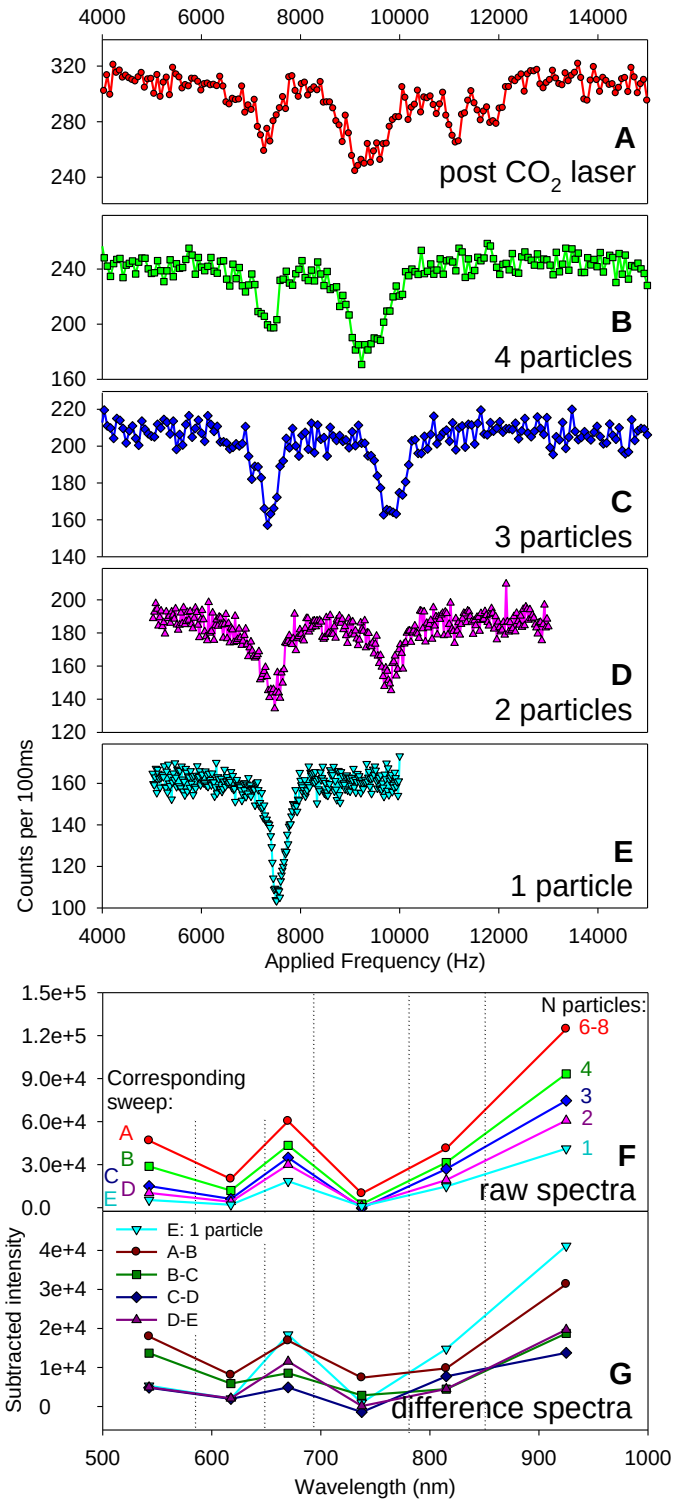

Figure 4.5 – Frequency and Emission Spectra as QDs Are Selectively Ejected. Frequency spectra for an ensemble of trapped red (solution λ_{max}=650 nm) QD NPs as NPs were ejected. A: Immediately after thermal brightening with 6-8 NPs in the trap, B: 4 NPs, C: 3 NPs, D: 2 NPs, E: 1 NP. Emission spectra corresponding with the sweeps are shown in F. Subtracted emission spectra, which approximate single NP spectra, are shown in G.

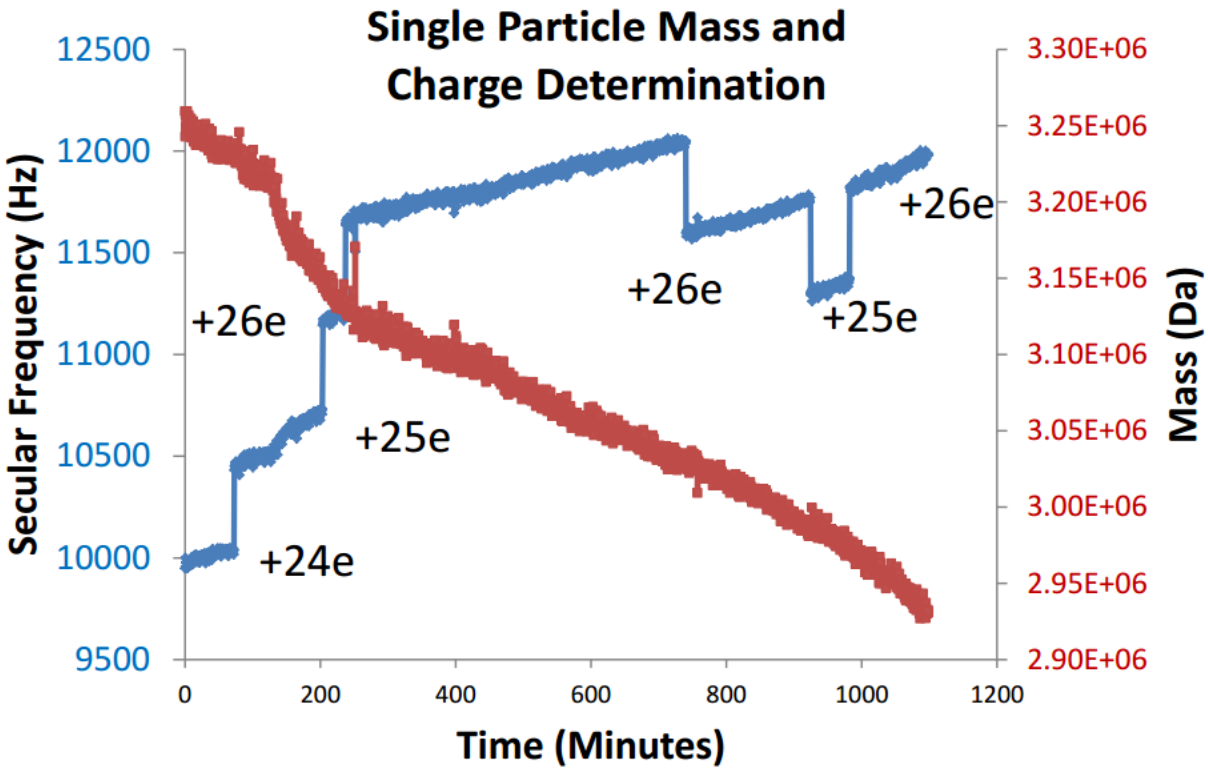

Figure 4.6 – Mass and Charge Determination of a Single QD. Tracking the mass and charge of a single QD aggregate NP that remained at the end of the experiment shown in Figure 4.5. Mass loss due to sublimation observed. Initial mass 3.25 MDa, initial charge +24 e.

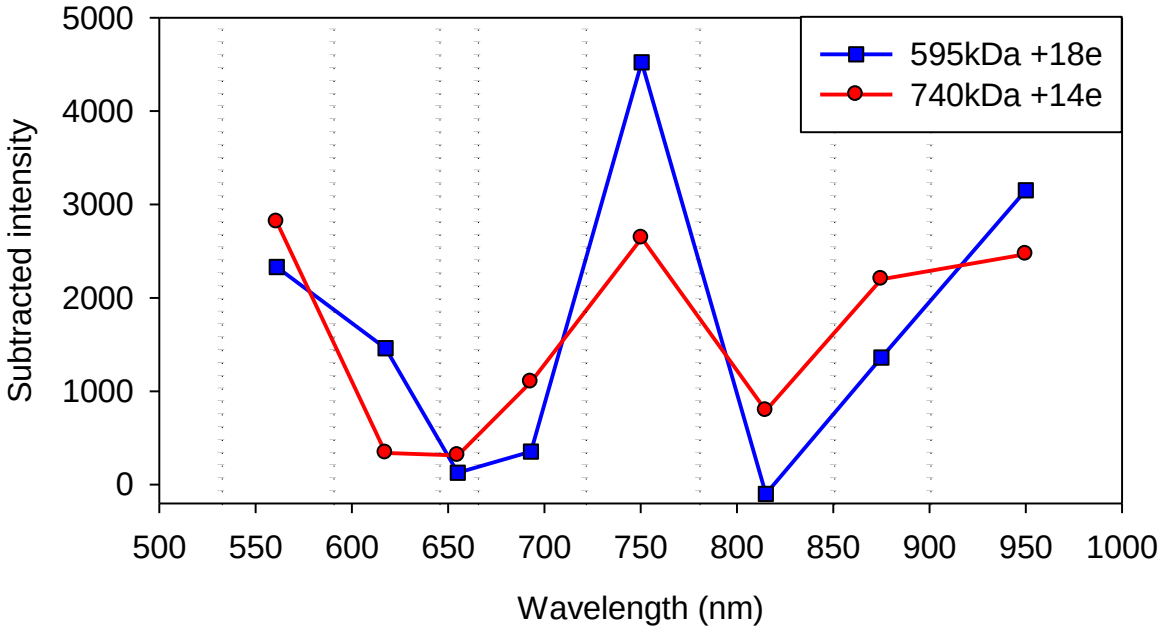

Figure 4.7 – Emission Spectra of Single Brightened QD Monomers. Single trapped red QD monomer emission spectra (solution λ_{max}=650 nm). No emission is observed at 650 nm indicating excitonic emission is totally bleached.

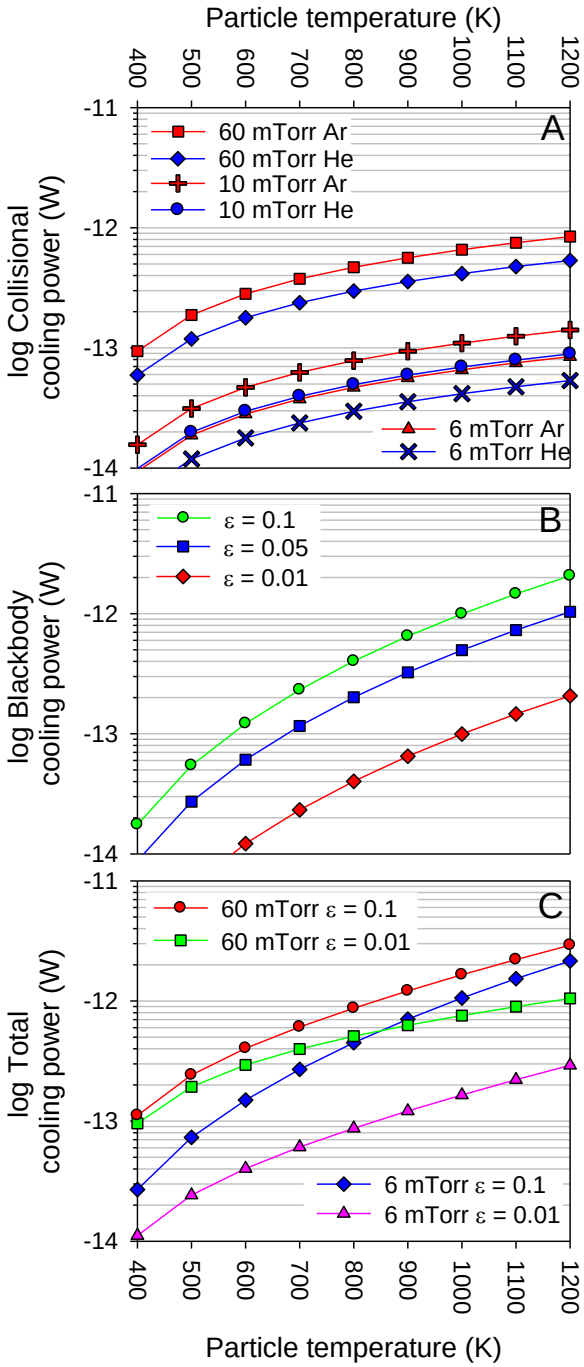

Figure 4.8 – Simulated Cooling Powers for a 7.5 nm QD. Simulations are under the range of conditions relevant to our experiments. Gas collisional cooling power is shown in A, blackbody cooling power in B, and the total cooling power in C.

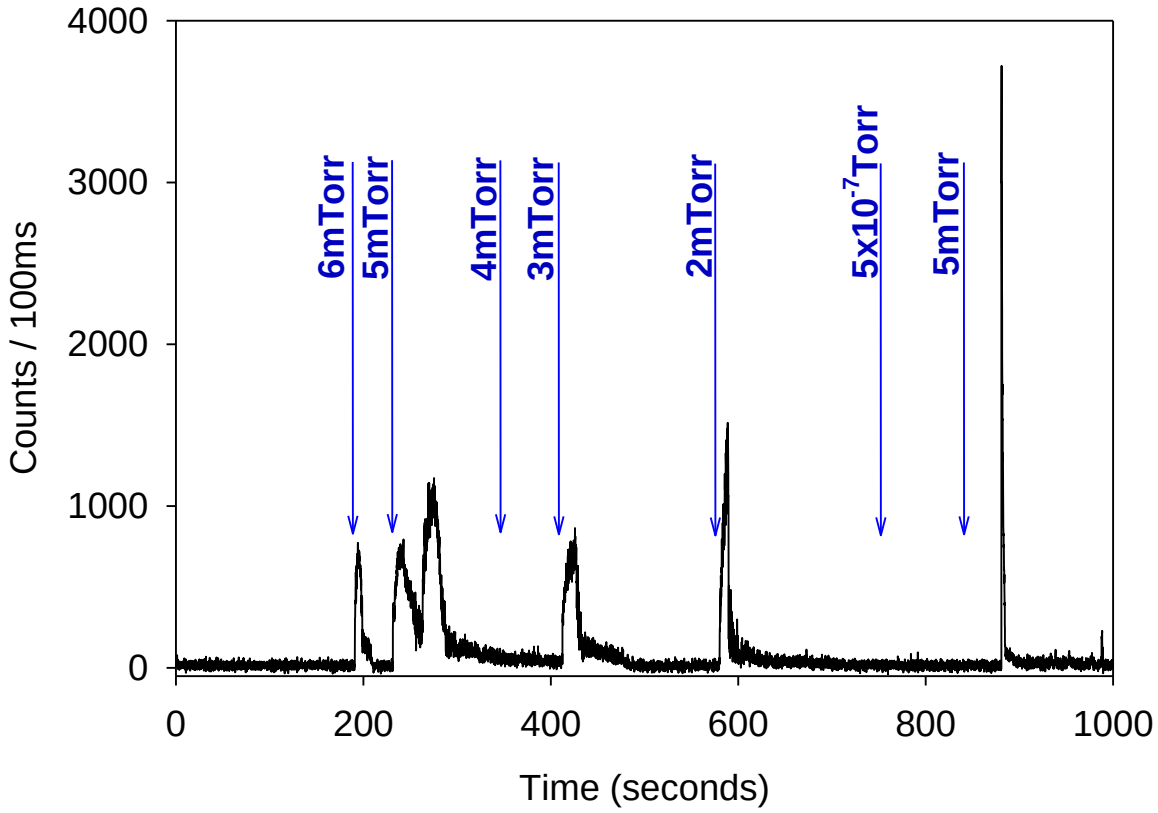

Figure 4.9 – Temperature Threshold of Thermal Activation. Thermal activation and rapid bleaching at high 532 nm laser intensity (165 W/cm^2) observed as a function of decreasing pressure. Visible irradiation brightened QD NPs in a narrow pressure range (6-2 mTorr). A certain set of NPs could not be brightened at pressures as low as 5 x 10^{-7} Torr, but were rapidly brightened as a result of CO_2 laser exposure at 5 mTorr.

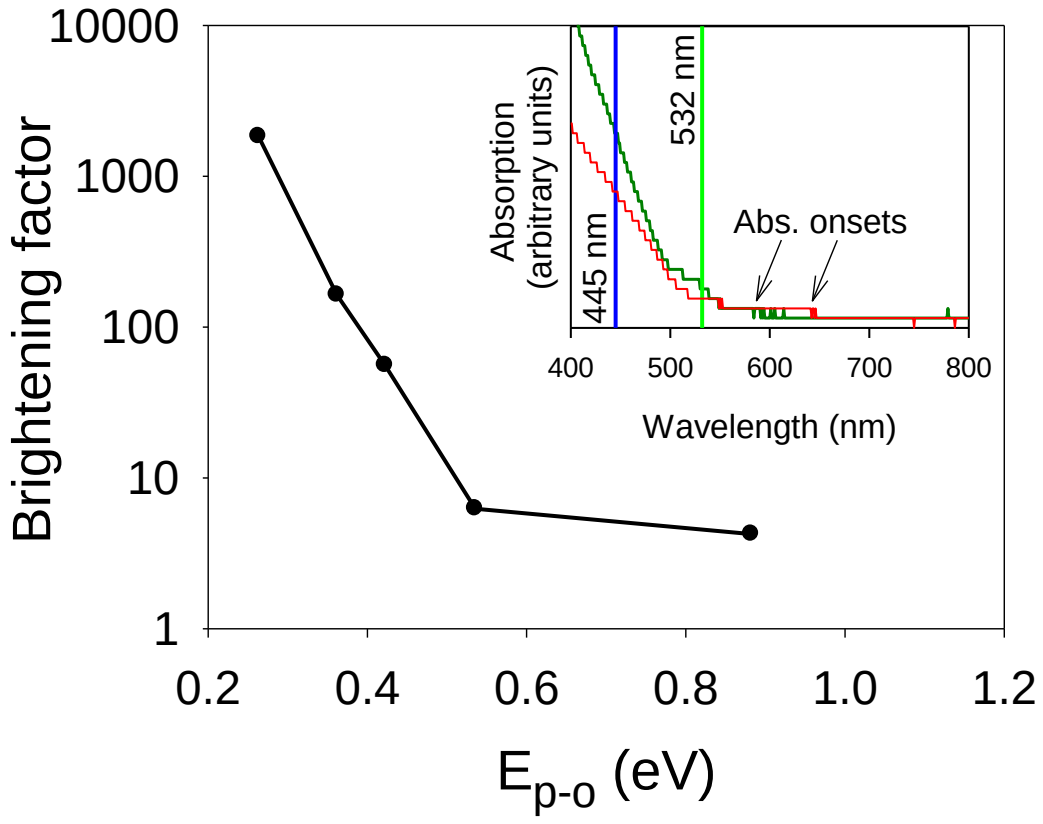

Figure 4.10 – Brightening Factor as a Function of Pump - Band Gap Difference. Brightening factor, the amount PL intensity increases as a result of thermal brightening, decreases as the difference between the pump energy and the absorption energy (E_{p-o}) increases. Sample absorption spectra are included as an inset.

CHAPTER 5

THERMALLY BRIGHTENED CdSe/ZnS QUANTUM DOTS AS NONCONTACT PROBES FOR SURFACE CHEMISTRY STUDIES OF DARK NANOPARTICLES TRAPPEDIN THE GAS PHASE

5.1 Introduction

Many nanoscience problems involve reactions of nanoparticles that are small enough (<10 nm) to have properties that differ significantly from the corresponding bulk values. For example, supported catalysts often have particles in this size range, and show strong variations in activity or selectivity if the size distribution is varied.[1-11] The size dependence may be influenced by quantum confinement, which tunes the electronic structure, and there may also be changes in the geometric structure of NPs with size.[12-19] In supported catalysts, understanding NP size effects is complicated by interactions with the support, and surface chemistry data for support-free NPs would be useful in understanding both size and support effects. Because a substantial fraction of the atoms in small NPs is in the surface layer, the NP mass is quite sensitive to surface reactions. Therefore, by monitoring NP mass as a function of time as processes such as absorption, desorption, or reactions occur, it is possible to measure surface kinetics.[20]

Advances in nanoparticle mass spectrometry (NPMS) over the past two decades have opened up new avenues for nanoparticle (NP) analysis, including high precision NP mass (M) and charge (Q) measurements for individual NPs,[21] single NP surface chemistry experiments,[20] and characterization of single bio-particles.[22-24] Several groups have used image charge detection schemes to detect nanoparticles for mass spectrometry,[25] [26-28] but this approach does not lend itself to experiments where NPs must be monitored over time to measure kinetics, or where NP emission spectra are measured as *M* and *Q* vary. Nondestructive optical detection of trapped NPs has been reported by several groups.[20, 21, 29-38] Large NPs (>100 nm) are easily detected by light scattering,[21] and laser-induced fluorescence/luminescence works for NPs such as dye-doped polymer

spheres[35, 39] or semiconductor nanocrystal quantum dots (QDs).[39, 40] Unfortunately, many NPs of interest from a surface chemistry perspective are too small for light scattering detection, and are nonluminescent. In principle, such NPs could be monitored by labeling them with one or more fluorescent probe molecules or NPs, however, the probes would tend to perturb the small dark particles, and might not remain bright under reaction conditions. Here we demonstrate a noncontact approach to optically probing dark NPs by cotrapping with a bright probe NP, and demonstrate that thermally brightened CdSe/ZnS quantum dots are near-ideal probe NPs.

Secular motion is detected by measuring variations in light scattering or photoluminescence signal as the NP oscillates in the trap, thus modulating its overlap with the detection volume. The envisioned noncontact probe approach involves trapping a dark NP of interest together with an optically bright probe NP with the same charge polarity, so that the two NPs repel each other. Coulomb repulsion also couples the motion of the two NPs, so that in principle, the motion and properties of the dark NP can be inferred from its effects on the motion of the bright NP. As demonstrated below, for the correct coupling strength, the method works and is quite straightforward to interpret.

The probe NP must obviously be optically bright under all the conditions of interest, but it also must have mass that is less than or comparable to that of the dark NPs of interest, so that the dark NP can scatter it out of the detection volume. The size range of greatest interest for NP surface chemistry is below ~10 nm, thus probe NPs with masses in the 10^5 Da range are needed. For NP surface chemistry experiments, it will be necessary to heat the dark NP by CO_2 laser irradiation (10.6μm) for cleaning/annealing, and the NPs will also be exposed to various gaseous reactants. Therefore, the probe NP

must survive intense CO_2 laser irradiation and reactant exposures, remaining luminescent and not undergoing large *M* or *Q* changes which would complicate analysis. CdSe/ZnS core/shell QDs are available with masses in the ~ 1 - 7 x 10^5 Da range and, as shown below, have properties that appear almost ideal for use as probe NPs.

Semiconductor QDs have been studied in detail in the condensed phase,[41-43] where they are often used as luminescent probes, however, few studies of QDs in the gas phase have been reported, with the notable exception of Xiong *et al.* who measured photoemission from gas-phase QDs.[44] We reported NPMS studies of gas-phase CdSe/ZnS core/shell QDs,[39, 40] demonstrating the possibility of monitoring a single QD for several days while continuously measuring *M,* Q, and the intensity and spectrum of photoluminescence (PL) from the QD. As-trapped QDs have low PL intensities, however, upon heating, the PL brightens dramatically and red shifts. In condensed phase measurements, thermal damage also leads to red-shifted emission attributed to creation of surface trap states,[45-47] however, trap state creation in the condensed phase is associated with decreased PL intensity.

This chapter has several goals. The thermal brightening process is explored in more detail, and then brightened QDs are examined with respect to their suitability for use as probe particles. The effects on *M,* Q, and PL intensity of both prolonged CO_2 laser irradiation and exposure to oxidizing environments at elevated temperatures are examined. Finally, the noncontact probe method is demonstrated, by measuring *M/Q* for a dark particle via its influence on the motion of a cotrapped probe QD, and simultaneous measurement of *M* and *Q* for three cotrapped QDs.

5.2 Experimental Methods

Mercaptoundecanoic acid-capped aqueous CdSe/ZnS core shell QDs (5.5nm CdSe core, 1 nm ZnS shell, solution emission λ_{max}=650 nm) were obtained from NN labs in concentrations of 1 mg/mL. The QD stock solution is a pH 8 Na^+-containing buffer solution, and is diluted 100:1 in methanol and electrosprayed, generating particles including QD monomers and small aggregates of 2-5 QDs with charges ranging from ~+3e to +20e *per* QD. Under these conditions, the acid groups should be largely ionized, and positive charge should be due to excess Na^+. The QDs were electrosprayed and trapped using the conditions outlined in Chapter 2. For the experiments discussed below, the hexapole, quadrupole, and trap were operated at a frequency of 145 kHz, with amplitude of 500 V.

Trapped QDs are detected optically, via PL. To prevent QD overheating and sublimation, the trap chamber is flooded with argon buffer gas to a pressure of 1 to 20 mTorr whenever the pump (532 or 405 nm) laser is on, and the pump beam was only loosely focused to keep pump intensities low (typically 50-150 W/cm^2). Spectra are determined by subtracting signals measured through the sequence of filters, as described in Chapter 4. For this purpose 10.6 μm light is generated from a duty-factor-modulated, quasi-cw, 10 W CO_2 laser. The CO_2 laser beam waist was measured by scanning a 1 mm diameter alumina rod, mounted on a precision manipulator, through the trap center, using visible emission from the rod to detect the beam. The beam waist diameter was estimated to be ~600μm.

.

5.3 Effects of Laser Heating on Photoluminescence, Mass, and Charge

Figure 5.1 illustrates several important aspects of the interaction of gas-phase QDs with visible and 10.6 μm radiation. The experiment started with the 532 nm laser focused through the empty trap at intensity of ~50 W/cm^2, allowing the background (scattered light + APD dark counts) to be measured (Figure 5.1A – green horizontal line labeled "532 nm"). There is also scattered light background from the CO_2 laser due to visible emission from the laser discharge, and this background level is indicated by the horizontal red line labeled "CO_2" in Figure 5.1A.

After ~20 s, a small ensemble of QDs was injected over the course of ~10 s, resulting in a signal rise of only ~120 counts/s relative to the 532 nm baseline (i.e., ~12 counts *per* 100 ms time bin). The QDs were trapped at ~10 mTorr, and the pressure was held constant for the duration of the experiment. After a few s, the emission spectrum for the as-trapped QDs was collected, as shown in Figure 5.1B. The vertical lines overlaying the spectra show the filter cutoff wavelengths, and the points centered between the cutoffs show the integrated intensity in each spectral region. As we have observed previously, the emission spectrum of the as-trapped QDs closely matches the spectrum for the same QDs in solution, but is much weaker (<1 %) than would be expected based on solution phase absorption cross sections and emission quantum yields.[40] Due to the spectral similarity, we presume the nature preheated gas phase QDs emission is excitonic.

After completion of the as-trapped emission spectrum, the 532 nm laser was blocked, and the signal dropped to the APD dark count baseline. Next, the CO_2 laser was focused through the trap for 90 s at an intensity of ~1 kW/cm^2. During this IR-only excitation period emission significantly above the "CO_2" baseline was observed. The

emission appears noisy, but this at least partly reflects the ±10% amplitude stability of our CO_2 laser. Since this experiment was performed on an ensemble of trapped QDs, this 'noise' cannot be attributed to a single particle moving in and out of the CO_2 laser beam or APD detection area. Figure 5.1C shows an emission spectrum for a different ensemble of the same QDs for 10.6 μm-only excitation. Significant emission is seen only between 900 nm and the APD cutoff. After 90 s of CO_2 laser irradiation, the CO_2 laser was turned off, dropping the signal back to the dark count baseline. The 532 nm laser was then unblocked, resulting in initial PL signal of ~25,000 counts/s (note scale change), i.e., CO_2 laser heating transformed the QDs such that their PL was brighten by a factor of ~200. During the first ~30 s of 532 nm irradiation, the PL underwent additional brightening to 32,000 counts/s before leveling off. Clearly CO_2 laser irradiation substantially brightened the QDs, but additional visible laser exposure was required to complete the brightening transformation.

Just before 200 s, the 532 nm laser was again blocked, and then the CO_2 laser was again focused through the trap at 1 kW/cm^2. Note that during this second IR-only exposure period, there was no emission in excess of the "CO_2" baseline. The absence of IR-driven emission suggests that once the brightening process was driven to completion by the visible laser, the QDs no longer absorbed enough CO_2 laser radiation to produce near-IR emission.

Finally, the CO_2 laser was switched off, and the 532 nm laser was unblocked, resulting in PL with intensity equal to that prior to the second period of CO_2 laser irradiation. During the middle of this final period of 532 nm irradiation, another emission spectrum was taken, which is plotted in Figure 5.1B, scaled by a factor of 1/150. The

integrated intensity is ~270 times higher after CO_2 laser irradiation, than for the as-trapped QDs. Note that the spectrum no longer resembles the as-trapped spectrum. Emission is observed from a variety of states, with intensity maxima at ~550nm (limited by pump wavelength), around 750 nm, and in a final feature extending into the near-IR, limited by the APD sensitivity cutoff. Similar post-heating PL spectra are seen for QDs with different diameters, for small aggregates of heated QDs, [40] and for QDs in the process of subliming.[39] Because the emission intensity is found to scale roughly as $M^{2/3}$, i.e., surface states appear to dominate the emission.[39] From the probe particle perspective, the important result from Figure 5.1 is that the PL intensity from CO_2-laser heated QDs is quite bright, and not changed by additional CO_2 laser exposure.

Figure 5.2 examines the effects of CO_2 laser irradiation over a much longer time scale. An ensemble of QDs was trapped with the 532 nm laser blocked and the CO_2 laser on at ~1kW/cm^2 with the pressure set at ~10 mTorr. During QD injection (100 – 110 s) the emission increased to ~2000 counts/s, and dropped to ~1200 counts/s by 200 s. After completion of injection, the emission continued for nearly 3000 s, dropping slowly, with fluctuations due to instability of the CO_2 laser. Clearly, under these conditions, a significant fraction of the trapped QDs continued to absorb at 10.6 μm, resulting in weak emission that presumably resembles that in Figure 5.1C. At ~3200s the pressure was lowered in several steps to <1 mTorr, leading to a decrease in emission intensity to baseline. To show that the signal loss was real, and not simply due to ejection of the QDs from the trap at low pressures, the final step was to turn the CO_2 laser off (at 3400 sec) and unblock the 532 nm laser, allowing it to pass through the trap ~130 W/cm^2, resulting in ~30,000 counts/s of PL signal – 300 times the signal generated by CO_2 laser irradiation

alone.

In Figure 5.1, after the QDs have been heated by visible laser exposure they no longer appear to absorb 10.6 μm radiation enough to cause significant near-IR emission. Figure 5.2 makes plain that this transformation can also be induced by exposure to the CO_2 laser alone, although the pressure must be lowered so that the QDs are not cooled as efficiently to achieve the same result.

Figure 5.3 shows an experiment where the QDs were exposed first to 532 nm radiation, and then to various combinations of 532 nm and 10.6 μm radiation, including some periods where the two lasers overlapped. For this figure, the scattered light and dark count baselines for the two lasers have been subtracted. QDs were injected into the trap between 0 and 10 s at ~10 mTorr. The green and red horizontal lines indicate times when the particles were then exposed to various combinations of the 532 nm pump laser (green line - 95 W/cm^2) and the CO_2 laser (red line – 1kW/cm^2). During injection, brightening occurred in two steps, indicating the combination of higher 532 nm laser intensity and lower argon pressure lead to enough heating to cause brightening of some of the QDs. After trap filling was complete, the baseline-subtracted PL intensity stabilized at ~ 450 counts/s. At 40 s, the visible laser was blocked and then at 50 s the CO_2 laser was tuned on at 1kW/cm^2. This resulted in increased noise due to visible light from the CO_2 laser discharge, but no increase in actual, background-subtracted PL signal. The visible light from the CO_2 laser is from the electrical discharge and is not very intense. While visible light can enter the trap, any UV light that might be emitted would be absorbed by the ZnS Cleartran entrance window. We therefore do not expect any changes in behavior as a result. At 80 s, the CO_2 laser was turned off again, leading to an

immediate return to the dark count baseline. At 100 s the 532 nm laser was unblocked and the PL signal was found to have brightened ~15% compared to the level before CO_2 laser heating. Additional periods of irradiation with the CO_2 laser, the visible laser, or both, resulted in significant emission only when the visible laser was on, with no further increase in intensity. This experiment indicates that once QDs are fully brightened by some combination of visible and IR laser heating, further 10.6 μm irradiation has no effect on 532 nm-pumped PL, even when both visible and IR lasers are present simultaneously.

Figures 5.1 and 5.3 show that the PL intensity from fully brightened QDs is insensitive to further CO_2 irradiation. For use as probe NPs, it is also important that *M* and *Q* for the QDs be stable. Figure 4.4 shows that this is the case. The approach to measuring *M* and *Q* for a single trapped particle is outlined above, and detailed elsewhere.[21, 39, 48] For this experiment we measured the axial frequency, $f_z = \omega_z/2\pi$, by applying a weak sinusoidal drive voltage at frequency f_{drive} to an electrode just outside the trap, resulting in a dip in measured PL intensity when f_{drive} is in resonance with f_z, as described in Chapter 3.

The main frame of the Figure 5.4 shows how *M/Q* (f_z) varies with time over 40 min. *M/Q* was initially ~45 kDa/e, and dropped by ~3% over the 40 min, due to slow sublimation driven by heating from the ~45 W/cm^2 visible pump laser.[39] In the middle of the experiment, the 532 nm laser was blocked, and the CO_2 laser was focused through the trap at 1 kW/cm^2 for 10 min. When the CO_2 laser was turned off, and the 532 nm laser was unblocked, it can be seen that there was essentially no change in *M/Q* during the period of CO_2 laser irradiation. Certainly the mass loss rate from 1 kW/cm^2 of CO_2 laser

irradiation was much slower than from 45 W/cm^2 of 532 nm irradiation.

After completion of the experiment, Q, and therefore M, was determined by turning on a weak discharge to generate Ar^+ and electrons to drive charge steps. The initial QD mass was determined to be 634 kDa, with Q = +14e. This experiment makes several points. There was clearly no change in Q induced by the period of CO_2 laser irradiation, and the mass change over that 10 min period was also much smaller than during an equivalent period of 532 nm irradiation, even though the CO_2 laser intensity was ~20 times higher. This figure also provides an example of the sensitivity of NPMS to small mass changes. The rate of mass change translates to ~8 Da/s, i.e., we are easily able to measure mass loss corresponding to a few atoms per minute from a particle that has more than 10^4 atoms.

5.4 Effects of Surface Chemistry on Probe Particle Photoluminescence

In order that QDs be useful as probe particles, it is important that they remain luminescent under conditions of interest, including conditions which might, for example, lead to oxidation of the particle surfaces. Given the likelihood of emission from surface states, oxidation might quench PL. To test this point, Figures 5.5, 5.6, and 5.7 show experiments probing the effects of particle heating and surface oxidation on PL intensity. In each experiment, a single QD-based NP was trapped, brightened by CO_2 laser irradiation, and heated to the point of slow sublimation in argon by 532 nm-pumped PL. After M and Q were measured, the argon buffer gas was replaced with oxygen, where the sublimation was continued. In two cases (Figures 5.5 and 5.6), large QDs (5.5 nm CdSe core, 1 nm ZnS shell = ~640 kDa) were used in an attempt to trap a single monomer in

the ~1 MDa range, but in Figure 5.7 small QDs (2.5 nm CdSe core, 1 nm ZnS shell = ~125 kDa) were used in an attempt to trap a larger aggregate in the ~1 MDa range. In one experiment (Figure 5.5) the initial mass of the particle was 892 kDa, which could be either a monomer or dimer. In the case of Figure 5.6, the trapped particle was clearly a monomer (M_0 = 377 kDa). In both cases switching to oxygen resulted in no change in Q or the PL intensity, and a slight decrease in the rate of mass loss. In both cases the particles were stable for more than an hour under oxidizing conditions, making them ideal as probe particles.

In Figure 5.7 the initial mass of a single QD NP was ~1.54 MDa, suggesting that the NP was an aggregate of ~12 QDs. Small QD aggregates formed in the electrospray process are easily trapped, and after brightening, they have PL properties similar to QD monomers.[40] Aggregates therefore provide a source of more massive probe particles as needed. In this experiment, the 532 nm pump laser intensity was ~100 W/cm^2, heating the NP to drive ~11%/hour mass loss. The noisier secular frequency and mass traces reflect use of faster f_{drive} scans in order to track the faster mass loss. The figure also plots the PL intensity, which shows two kinds of changes in the experiment. There are steps in PL intensity correlated with the steps in Q. This correlation simply reflects the fact that the effective potential[21] confining the NP varies like Q^2, thus, the amplitude of the secular oscillations decreases with increasing Q, such that the NP spends more time in the detection volume, and therefore appears brighter. In addition, PL changes with the NP surface chemistry.

At ~70 minutes, the background gas was switched from Ar to O_2, and it can be seen that the rate of mass loss increased significantly, presumably due to some oxidation

reaction that volatilized some component of the NP. There was no obvious change in PL during the oxidation process, beyond what would be expected from the continuing charge steps. Note, however, that at ~125 min the rate of mass loss slowed dramatically, suggesting that the oxidative volatilization process was nearing completion. At this point, PL intensity suddenly dropped by ~50%, even though there was no change in *Q*. It is not clear what reaction(s) were responsible for the oxidative volatilization, however, two reasonable candidates are SO_2 loss from the ZnS shell: $ZnS_{(s)} + O_{2(g)} \rightarrow ZnO_{(s)} + SO_{2(g)}$, and combustion of residual ligand constituents remaining on the surface. The mass loss during the oxidative volatilization process was ~19 %. Even if we assumed that the ligand layer remained intact after the initial CO_2 laser heating, and during the initial monitoring period before O_2 was introduced, complete loss of the ligands would decrease the NP mass by only ~3%. Complete conversion of the ZnS shell to ZnO would result in a ~12.5% mass loss. There is considerable uncertainty in this number, however, due to QD-to-QD variation in the actual thickness of the ZnS shell, the mass already lost before O_2 introduction, and the possibility that the Zn left behind is not fully oxidized.

Just before 200 min, the NP was subjected to 2 s of CO_2 laser irradiation, which substantially restored the PL intensity, but as might be expected from Figure 5.4, had no effect on *M* or *Q*. Again, it is not clear what process caused the CO_2 laser rebrightening, but from the perspective of use as a probe particle, the important point is that even though the PL intensity varied during surface oxidation and subsequent 10.6 μm irradiation, it remained high enough throughout for NP detection and secular frequency measurement. Since the PL intensity of monomers does not decrease upon O_2 exposure we conclude that monomers are superior as probes, but aggregates appear to be adequate if the desired

mass range is >1.5 MDa.

5.5 Noncontact Probe Determination of Dark NP *M/Q*

To test whether the noncontact probe method works, we took advantage of the fact that as-trapped, unheated QDs have PL intensities far too low for secular frequency measurements, but that once brightened, the PL intensities are high. Figure 5.8 shows a proof-of-principle experiment. A single QD-based NP was trapped and brightened by brief exposure to the CO_2 laser, and then probed by PL at low 532 nm pump intensity (~50 W/cm^2) at a pressure of ~5 mTorr. The secular frequency spectrum was measured by scanning the frequency (f_{Drive}) of a weak AC drive potential, as described above. The result is shown as the black spectrum labeled "probe QD", with a single peak at f_z = 21.5 kHz, corresponding to *M/Q* of 628 kDa/e. A second QD-based NP was then injected, but not exposed to the CO_2 laser. As expected, the PL intensity did not change significantly after injection of this QD since it was only exposed to the pump laser at low power and was never exposed to the CO_2 laser, i.e., the second NP was dark.

To prevent the dark particle from brightening due to 532 nm laser exposure the frequency spectrum was measured again immediately after injection of the dark particle, and a new peak at 5 kHz, corresponding to *M/Q* ~ 3 MDa/e was observed. There is also a weak peak at ~17 kHz which is tentatively assigned to the difference frequency f_{zNP1} - f_{zNP2}. In essence, as the f_{Drive} was scanned, secular oscillations of each NP were excited when f_{Drive} was resonant with either f_{zNP1} or f_{zNP2}. In the case of NP_1, the secular motion was directly detected because the oscillations caused this bright probe NP to spend less time in the detection volume. The secular oscillations of the dark NP_2 were detected

because NP_2 had some probability of scattering the probe NP_1 out of the detection volume. Critically, there was *no significant shift* in f_z for the probe NP due to the presence of NP_2, demonstrating that while the interparticle coupling is strong enough to allow noncontact probe detection, it is not so strong that it significantly perturbs f_z for the individual NPs. After the frequency spectrum was measured the trapped particles were exposed to the CO_2 laser, but unfortunately this resulted in the ejection of the dark particle form the trap.

5.6 Tracking *M* and *Q* for Multiple Particles Simultaneously

The final question is whether multiple NPs can be tracked for *M* and *Q* determination simultaneously, or whether charge stepping or mass changes might make it difficult to interpret multiparticle secular frequency spectra. Figure 5.9 shows that for small NPs with low *Q,* at least, interpretation is straightforward. This experiment was done with three cotrapped NPs, whereas in the anticipated noncontact probe experiments we would normally use two, in order to keep the analysis as simple as possible. For this experiment, three QD-based NPs were trapped, and all were brightened by brief CO_2 laser heating. The inset to the top frame of the figure shows the secular frequency spectrum, and the top frame tracks the three frequency peaks for four h as the NPs were heated by two different 532 nm pump laser intensities. The three NPs underwent independent charge stepping, allowing the masses to be extracted, as plotted in the lower frame of the figure. Because all three NPs were CO_2 laser-brightened, it was possibly to observe them directly, demonstrating that there is no significant perturbation of the frequency for cotrapped NPs when one of the NPs undergoes a charge step.

These NPs were composed of QDs with nominal monomer mass of 650 kDa, thus particles 1, 2, and 3 can be seen to be a monomer, a dimer, and either a trimer or tetramer of the QDs. The inset to the lower frame shows one of the frequency peak shapes in more detail. The frequency spectra were scanned from high to low frequency, and it can be seen that the onset of the dip is sharp, while the signal recovery is much slower, although this can be changed by changing the pressure of Ar used to damp the secular oscillations. The secular frequency is determined with precision limited by the sharpness of the onset. In this case, the frequency, hence *M/Q*, is determined to precision of ~0.1 %.

5.7 Brightening Mechanism

The results presented above show the following about the nature of the brightening transformation:

1. PL from as-trapped NPs at low visible laser intensity is weak, but solution-like excitonic in nature. Previous work showed that the weakness results, at least in part, from bleaching of the absorption cross section due to the presence of the charges needed to trap the particles.[40]
2. During CO_2 laser-only excitation, there is weak emission for $\lambda > \sim 850$ nm. This near-IR emission is stable on the hour time scale if the Ar pressure is high enough, but at low Ar pressures the near-IR emission quickly vanishes.
3. After the QDs are transformed by CO_2 laser heating, PL is hundreds of times brighter most likely due to an increase in surface states. Also the excitonic-like emission is gone. If the CO_2 laser heating is done at high Ar pressures, the

brightening transformation is only partial, and additional brightening may occur from visible laser heating (Figure 5.1). If the QDs are heated at low pressures, the brightening transformation can be driven to completion by CO_2 laser heating alone (Figure 5.2).

4. The brightening transformation can also be driven by visible laser excitation (Figure 5.3).
5. Fully brightened QDs show no near-IR emission during subsequent CO_2 laser exposure (Figs. 5.1 and 5.2).
6. PL from fully brightened QDs is not affected if the CO_2 laser is turned on at the same time as the 532 nm PL pump laser (Figure 5.3).
7. After brightening, *M* and *Q* of trapped QD are also unaffected by CO_2 laser irradiation (Figure 5.4).

Bulk ZnS and CdSe absorb weakly at 10.6 μm (absorption coefficient 0.016 cm^{-1},[49] and 0.2 cm^{-1},[50] respectively), and ZnS is a common CO_2 laser window material. On the other hand, the as-trapped, ligand-capped CdSe/ZnS particles obviously do absorb at 10.6 μm, strongly enough to result in detectable emission in the near-IR, and transformation of the QDs. The 10.6 μm radiation should be absorbed with moderate efficiency by the mercaptoundecenoic acid ligand layer,[51] and there may also be states at the ligand-ZnS or ZnS-CdSe interfaces that absorb at 10.6 μm. The observation that near-IR emission is no longer observed during CO_2 laser irradiation if the QDs are fully transformed, and that 532 nm-pumped PL is unaffected by simultaneous CO_2 irradiation, suggests that the transformation process involves loss or destruction of the 10.6 μm chromophores. As a result, CO_2 laser heating is self-limiting, and the fully transformed

QDs are stable with respect to prolonged, intense CO_2 laser irradiation, with no further change in *M,* Q, or PL characteristics. In addition to stability under reactive conditions (Figures 5.5, 5.6, and 5.7), these are exactly the properties needed for the bright NPs for use in noncontact probe experiments.

It is not entirely clear what the brightening transformation involves, although the observation of near-IR emission during CO_2 laser heating suggests that the QDs are reaching high temperatures (T_{QD}), and a thermal mechanism is also supported by the observations that increased buffer gas pressure moderates brightening, and that heating by visible laser excitation also can drive the transformation. In a recent report on the thermal properties of QDs, Zhao *et al.* demonstrate ligand desorption from solution-phase CdSe/ZnS QDs at ~432 K.[45] Similarly, Rowland and Schaller [46] observed irreversible PL loss upon heating ligand-capped CdSe/ZnS QDs above 400 K, attributed to damage to the ligand layer. Pong *et al.* predict theoretically that $S_{thiolate}$-ZnS bonds should be similar in energy to $S_{thiolate}$-Au bonds, and desorption of thiolate ligands from gold surfaces has been observed at temperatures of 480 K[52] and 440 K. [53] These results suggest that ligand desorption or damage is likely to occur for QD temperatures above ~450 K. If the ligand layer is the main 10.6 μm chromophore, then desorption or pyrolysis of the ligand layer would account for the self-limiting nature of CO_2 laser heating.

The near-IR emission intensity provides additional insight into the temperatures that might be reached during CO_2 laser irradiation. After brightening, the PL signal from a single QD under the conditions used here is typically ~500 counts/s, while the small ensemble in Figure 5.1 gave ~30,000 counts/s after brightening, suggesting that it contained ~60 particles. The raw near-IR signal observed during CO_2 laser heating was

~1020 counts/s, corresponding to detection of ~17 photons/s/QD in the range between ~850 nm and the APD cutoff at ~1100 nm.

One possibility is that the near-IR emission is simply the high energy tail of a blackbody-like thermal radiation spectrum. Taking the optical detector's efficiency (~35% at 900 nm, ~13% at 1000 nm, ~ 6% at 1100) into account, detecting 17 photons/s from a single 7.5 nm QD would require $T_{QD} \approx 800$ K, assuming unit emissivity ($\epsilon = 1$). In fact, ϵ for subwavelength diameter particles is expected to be well below unity,[54-58] thus T_{QD} would need to be significantly higher to account for the observed signal (e.g., ~915 K for $\epsilon = 0.1$). $T_{sublimation}$ is 1450 K for bulk ZnS[59] and CdSe decomposes at ~1540 K,[60] however, sublimation of CdSe nanostructures has been observed at temperatures as low as 773K,[61] which is clearly inconsistent with our observation of stable near-IR emission on the hour time scale during CO_2 laser irradiation. Therefore, we conclude that the near-IR emission is not strictly blackbody-like. It is not clear what the emission mechanism is, but as shown in Figure 5.1B, the heated QDs have states that emit strongly in the near IR, and these may have enough oscillator strength to give rise to detectable emission even at significantly lower T_{QD}.

We conclude, therefore, that the brightening transformation involves QD temperatures (T_{QD}) between ~450 K (minimum required for ligand loss/pyrolysis) and ~750 K (limited by QD sublimation), with the observation of near-IR emission strongly suggesting that T_{QD} is nearer the upper end of this range. We recently discussed cooling processes relevant to trapped QDs,[40] of which only collisions with the Ar buffer gas and radiative cooling are significant under these conditions. The flux-weighted energy transfer *per* collision is $2k(T_{QD} - T_{gas}) \cdot c_A$, where T_{gas} is 300 K, and c_A, the energy

accommodation coefficient (a measure of inelasticity), is expected to be close to unity for collisions between argon and ZnS or argon and the ligand layer. At 10mTorr, a 7.5 nm particle has 5.7 x 10^6 collisions/s with background argon atoms, resulting in a cooling power of ~2.3 x 10^{-14} W at 450 K, and ~7 x 10^{-14} W at 750 K, assuming $c_A = 1$. The weak near-IR emission observed during CO_2 laser heating is, itself, far too weak to significantly cool the QDs, however, there would still be significant cooling by radiation at longer wavelengths. To estimate the total radiated power, we assume that the radiated power follows the Stephan-Boltzmann law: $P(W/m^2) = \sigma\epsilon(T_{QD}^4 - T_{trap}^4)$, where σ is the Stephan-Boltzmann constant, ϵ is the emissivity, and T_{trap} is the trap temperature (≈300K). For ϵ in the range that might be expected for particles of this size (~0.01 – 0.05),[54-58] the radiative cooling power would be between 0.3 and 1.6 x 10^{-14} W at 450 K, rising by a factor of 9 at 750 K. The total cooling power would, therefore, be between 3 and 4 x 10^{-14} W at 450 K, and between 1 and 2 x 10^{-13} W at 750 K. Given the 1 kW/cm^2 laser intensity, we can, therefore, estimate that the 10.6 μm absorption cross section for as-trapped QDs would need to be ~3 x 10^{-17} cm^2 to drive T_{QD} to 450 K, or 2 x 10^{-16} cm^2 to reach 750 K.

5.8 Noncontact Probe Detection of Cotrapped Dark NPs

Figure 5.8 shows that it is possible to detect the presence of a dark NP via its effect on the motion of a cotrapped QD. More importantly, secular frequency spectrum of the cotrapped particles is simple, with no evidence of any significant perturbation of the frequencies by the presence of the cotrapped particle. Figure 5.9 shows that *M/Q* for several cotrapped particles can be measured simultaneously, and that charge stepping,

i.e., changes in secular frequency of one particle has no significant effect on the secular frequency of the cotrapped particles. As a result, the secular frequency spectra are trivial to analyze to extract *M/Q*, *M,* and *Q* of the individual particles.

The simplicity of the secular frequency spectrum reflects the fact that *Q* for these particles was low (~10e), so that the Coulomb interaction was small compared to the energies associated with thermal or secular motion, except in the very small fraction of time when the particles approach to within ~5 μm separation. This situation is very different from "sympathetic detection" as used to study trapped atomic ions at mK temperatures,[62-64] where the Coulomb interaction is large compared to the thermal energy, resulting in strong coupling and collective motion. The same is true for trapped NPs with high *Q*. Collective phenomena like Coulomb lattice formation can be seen for large, highly charged NPs, as first demonstrated by Wuerker *et al*. in 1959.[65]

5.9 Conclusion

We have shown that 10.6 μm radiation interacts with as-trapped QDs in the gas phase, increasing the photoluminescence brightness, and changing the spectrum from excitonic-like emission to emission over a wide wavelength range extending into the near IR. The brightening mechanism is shown to be thermal, and most likely involves desorption or pyrolysis of the ligand layer. Once the brightening transformation is complete, the QDs no longer absorb at 10.6 μm strongly enough to have any observable effect on PL intensity or on physical properties such as mass or charge. The brightening process can also be initiated by visible laser irradiation, however, the advantage of CO_2 heating is that it is self-limiting. In contrast, if brightening is done using a visible laser

that pumps exciton creation in the semiconductor core of the particle, the QDs vaporize rapidly unless the laser intensity and buffer gas pressure is carefully controlled.

Thermally brightened CdSe/ZnS core shell QDs appear near ideal as noncontact probe particles, and the experiments in Figures 5.8 and 5.9 make it clear that it is possible to use cotrapping as a way to monitor *M* and *Q* of a dark particle over time. QDs are bright, and remain bright indefinitely under low visible pump laser intensities. Indeed, we have shown that they remain bright even if they are heated to the point of subliming a significant portion of their mass.[39] In addition, while there is some effect of surface chemistry on PL intensity, it remains high enough for secular frequency measurement even after reactions as extreme as oxidative volatilization of a significant fraction of the ZnS shell. Finally, it is desirable that the mass of the probe particle (M_p) should be comparable to the mass of the test particle (M_t), so that the test particle is able to scatter the probe particle out of the detection volume. On the other hand, if $M_p \ll M_t$ it may be difficult to trap both particles under the same conditions. QDs with masses ranging from ~ 1 - 7 x 10^5 Da are readily available, and we have demonstrated (Figure 5.8) that it is possible to generate aggregates with masses of at least 2 x 10^6 Da. This makes QDs appropriate test particles with masses between 1 x 10^5 and at least 1 x 10^7 Da. For example, this would enable noncontact probe detection of platinum particles in the 2 – 12 nm range.

Co-trapping experiments in which *M* and *Q* are monitored for three cotrapped particles (Figure 5.9) and in which *M/Q* of a dark particle is measured by observing perturbations to a bright probe particle (Figure 5.8) have been presented. Together, these experiments show that co-trapping should allow *M* and *Q* measurements by the

noncontact probe method, with mass precision of at least 0.1 %. Currently, our instrument has only a single NP source, making experiments in which two different types of NPs are cotrapped difficult. The next step is to add a second NP source, allowing co-trapping experiments where QDs are used to probe dark NPs with interesting surface chemistry.

5.10 References

1. C. T. Campbell, A. W. Grant, D. E. Starr, S. C. Parker, and V. A. Bondzie, Topics in Catalysis **14** (1-4), 43-51 (2001).
2. M. Che and C. O. Bennet, Adv. Catal. **36**, 55-172 (1989).
3. G. A. Ferguson, F. Mehmood, R. B. Rankin, J. P. Greeley, S. Vajda, and L. A. Curtiss, Topics in Catalysis **55** (5-6), 353-365 (2012).
4. H. J. Freund, Angew. Chem., Int. Ed. Engl. **36** (5), 453-475 (1997).
5. B. C. Gates, J. Mol. Catal. A: Chem. **163** (1-2), 55-65 (2000).
6. D. W. Goodman, Surf. Rev. Lett. **2** (1), 9-24 (1995).
7. J. F. Hamilton and R. C. Baetzold, Science **205**, 1213 -1220 (1979).
8. D. R. Rainer, C. Xu, and D. W. Goodman, J. Mol. Catal. A: Chem. **119** (1-3), 307-325 (1997).
9. M. Haruta, Catalysis Today **36** (1), 153-166 (1997).
10. C. R. Henry, Appl. Surf. Sci. **164**, 252-259 (2000).
11. M. Ichikawa, NATO ASI Ser., Ser. E **331** (Chemisorption and Reactivity on Supported Clusters and Thin Films), 153-192 (1997).
12. S. R. Plant, L. Cao, and R. E. Palmer, J. Am. Chem. Soc. **136**, 7559-7562.
13. K. Koga and K. Sugawara, Surf. Sci. **529** (1-2), 23-35 (2003).
14. D. Reinhard, B. D. Hall, P. Berthoud, S. Valkealahti, and R. Monot, Phys. Rev. Lett. **79** (8), 1459-1462 (1997).
15. S. Illy, O. Tillement, F. Machizaud, J. M. Dubois, F. Massicot, Y. Fort, and J.

Ghanbaja, Philosophical Magazine A: Physics of Condensed Matter: Structure, Defects and Mechanical Properties **79** (5), 1021-1031 (1999).

16. G. A. Somorjai, R. L. York, D. Butcher, and J. Y. Park, Phys. Chem. Chem. Phys. **9** (27), 3500-3513 (2007).

17. C. Barreteau, M. C. Desjonqueres, and D. Spanjaard, European Physical Journal D: Atomic, Molecular, Optical and Plasma Physics **11** (3), 395-402 (2000).

18. A. Wurl, M. Hyslop, S. A. Brown, B. D. Hall, and R. Monot, European Physical Journal D: Atomic, Molecular, Optical and Plasma Physics **16** (1-3), 205-208 (2001).

19. J. Yang, W. Hu, S. Chen, and J. Tang, J. Phys. Chem. C **113** (52), 21501-21505 (2009).

20. S. Schlemmer, S. Wellert, F. Windisch, M. Grimm, S. Barth, and D. Gerlich, Appl. Phys. A: Mater. Sci. Process. **78** (5), 629-636 (2004).

21. S. Schlemmer, J. Illemann, S. Wellert, and D. Gerlich, J. Appl. Phys. **90** (10), 5410-5418 (2001).

22. W. P. Peng, Y. C. Yang, M. W. Kang, Y. T. Lee, and H. C. Chang, J. Am. Chem. Soc. **126**, 11766-11767 (2004).

23. E. E. Pierson, D. Z. Keifer, L. Selzer, L. S. Lee, N. C. Contino, J. C. Y. Wang, A. Zlotnick, and M. F. Jarrold, J. Amer. Chem. Soc. **136** (9), 3536−3541 (2014).

24. S. Martin, C. Ortega, L. Chen, R. Bredy, A. Vernier, P. Dugourd, R. Antoine, J. Bernard, G. Reitsma, O. Gonzalez-Magana, R. Hoekstra and T. Schlatholter, Phys. Rev. A **89** (1), 0127071 - 0127078 (2014).

25. D. Z. Keifer, E. E. Pierson, J. A. Hogan, G. Bedwell, P. E. Prevelige, and M. F. Jarrold, Rapid Commu. Mass Spectrom. **28** (5), 483-488 (2014).

26. H. Hernández and C. V. Robinson, Nat. Protoc. **2**, 715 - 726 (2007).

27. T. Doussineau, P. Dugourd, and R. Antoine, Spectrosc. Eur. **24** (4), 16-20 (2012).

28. W. P. Peng, Y. T. Lee, J. W. Ting, and H.-C. Chang, Rev. Sci. Instrum. **76**, 023108-023105 (2005).

29. D. M. Bell, C. R. Howder, D. Gerlich, D. K. Lewis, and S. L. Anderson, Int. J. of Mass Spectrom. **(submitted)** (2014).

30. Y. Cai, W. P. Peng, and H. C. Chang, Anal. Chem. **75** (8), 1805-1811 (2003).

31. Y. Cai, W. P. Peng, S. J. Kuo, Y. T. Lee, and H. C. Chang, Anal. Chem. **74** (1),

232-238 (2002).

32. C. Graf, R. Lewinski, S. Dembski, B. Langer, and E. Ruehl, Phys. Status Solidi C **4** (9), 3244-3259 (2007).

33. M. Grimm, B. Langer, S. Schlemmer, T. Lischke, U. Becker, W. Widdra, D. Gerlich, R. Flesch, and E. Ruehl, Phys. Rev. Lett. **96** (6), 066801/066801-066801/066804 (2006).

34. G. Hars and Z. Tass, J. Appl. Phys. **77** (9), 4245-4250 (1995).

35. W. P. Peng, Y. Cai, Y. T. Lee, and H. C. Chang, Int. J. Mass Spectrom. **229** (1-2), 67-76 (2003).

36. S. C. Seo, S. K. Hong, and D. W. Boo, Bull. Korean Chem. Soc. **24**, 552-554 (2003).

37. A. J. Trevitt, P. J. Wearne, and E. J. Bieske, Int. J. Mass Spectrom. **262** (3), 241-246 (2007).

38. A. J. Trevitt, P. J. Wearne, E. J. Bieske, and M. D. Schuder, Opt. Lett. **31** (14), 2211-2213 (2006).

39. D. M. Bell, C. R. Howder, R. C. Johnson, and S. L. Anderson, ACS Nano **8**, 2387–2398 (2014).

40. C. R. Howder, B. A. Long, D. M. Bell, K. H. Furakawa, R. C. Johnson, and S. L. Anderson, ACS Nano **8** (12), 12534-12548 (2014).

41. A. M. Smith and S. Nie, Acc. Chem. Res. **43** (2), 190 - 200 (2010).

42. V. Lesnyak, N. Gaponik and A. Eychmuller, Chem. Soc. Rev **42**, 2905--2929 (2013).

43. M. Nirmal and L. Brus, Acc. Chem. Res. **32** (5), 407-414 (1999).

44. W. Xiong, D. D. Hickstein, K. J. Schnitzenbaumer, J. L. Ellis, B. B. Palm, K. E. Keister, C. Ding, L. Miaja-Avila, G. Dukovic, J. L. Jimenez, M. M. Murnane, and H. C. Kapteyn, Nano Lett. **13**, 2924−2930 (2013).

45. Y. Zhao, C. Riemersma, F. Pietra, R. Koole, C. d. M. Donega, and A. Meijerink, ACS Nano **6** (10), 9058-9067 (2012).

46. C. E. Rowland and R. D. Schaller, J. Phys. Chem. C **117** (33), 17337-17343 (2013).

47. C. Bullen and P. Mulvaney, Langmuir **22** (7), 3007 - 3013 (2006).

48. C. R. Howder, D. M. Bell, and S. L. Anderson, Rev. Sci. Instrum. **85**, 014104 - 014110 (2014).

49. Cadmium Selenide (Cdse) Absorption, Reflection, Luminescence. In Ii-Vi and I-Vii Compounds; Semimagnetic Compounds, O. Madelung, U. Rössler, and M. Schulz, Eds. Springer Berlin Heidelberg: 1999; Vol. 41B, pp 1-7.

50. Zinc Sulfide – Zns and Zns Clear. In http://www.schott.com/advanced_optics/english/download/schott_zinc_sulfide_may_2011_eng.pdf

51. S. E. Stein, director, in *NIST Chemistry WebBook, NIST Standard Reference Database Number 69*, edited by W. G. Mallard and P. J. Linstrom (NIST Mass Spec Data Center, National Institute of Standards and Technology, Gaithersburg MD 20899 (http://webbook.nist.gov). 2000).

52. D. J. Lavrich, S. M. Wetterer, S. L. Bernasek, and G. Scoles, J. Phys. Chem. B **102**, 3456-3465 (1998).

53. H. Kang, Y. Kim, T. Park, J. B. Park, E. Ito, M. Hara, and J. Noh, Bull. Korean Chem. Soc. **32**, 1253-1257 (2011).

54. H. C. van de Hulsst, *Light Scattering by Small Particles*. (Dover, New York, 1981).

55. C. F. Bohren and D. R. Huffman, *Absorption and Scattering of Light by Small Particles*. (Wiley, New York, 1983).

56. L. Landstrom, K. Elihn, M. Boman, C. G. Granqvist, and P. Heszler, Appl. Phys. A **81**, 827-833 (2005).

57. L. Landstrom and P. Heszler, J. Phys. Chem. B **108**, 6216-6221 (2004).

58. P. Roura and J. Costa, Eur. J. Phys. **23**, 191-203 (2002).

59. Zinc Sulfide, Ipcs International Programme on Chemical Safety. http://www.inchem.org/documents/icsc/icsc/eics1627.htm.

60. Cadmium Selenide (Cdse) Debye Temperature, Heat Capacity, Density, Melting Point, Hardness.In II-VI and I-VII Compounds; Semimagnetic Compounds, O. Madelung, U. Rössler, and M. Schulz, Eds. Springer Berlin Heidelberg: 1999; Vol. 41B, pp 1-3.

61. B. Goris, M. A. Van Huis, S. Bals, H. W. Zandbergen, L. Manna, and G. Van Tendeloo, Small **8**, 937-942 (2012).

62. M. Drewsen, I. Jensen, J. Lindballe, N. Nissen, R. Martinussen, A. Mortensen, P. Staanum, and D. Voigt, Int. J. Mass Spectrom. **229** (1-2), 83-91 (2003).

63. B. Roth, P. Blythe, and S. Schiller, Physical Review A: Atomic, Molecular, and Optical Physics **75** (2, Pt. B), 023402/023401-023402/023408 (2007).

64. S. Willitsch, M. T. Bell, A. D. Gingell, and T. P. Softley, Physical Chemistry Chemical Physics **10** (48), 7200-7210 (2008).

65. R. F. Wuerker, H. H. Shelton, and R. V. Langmuir, J. Appl. Phys. **30** (3), 342-350 (1959).

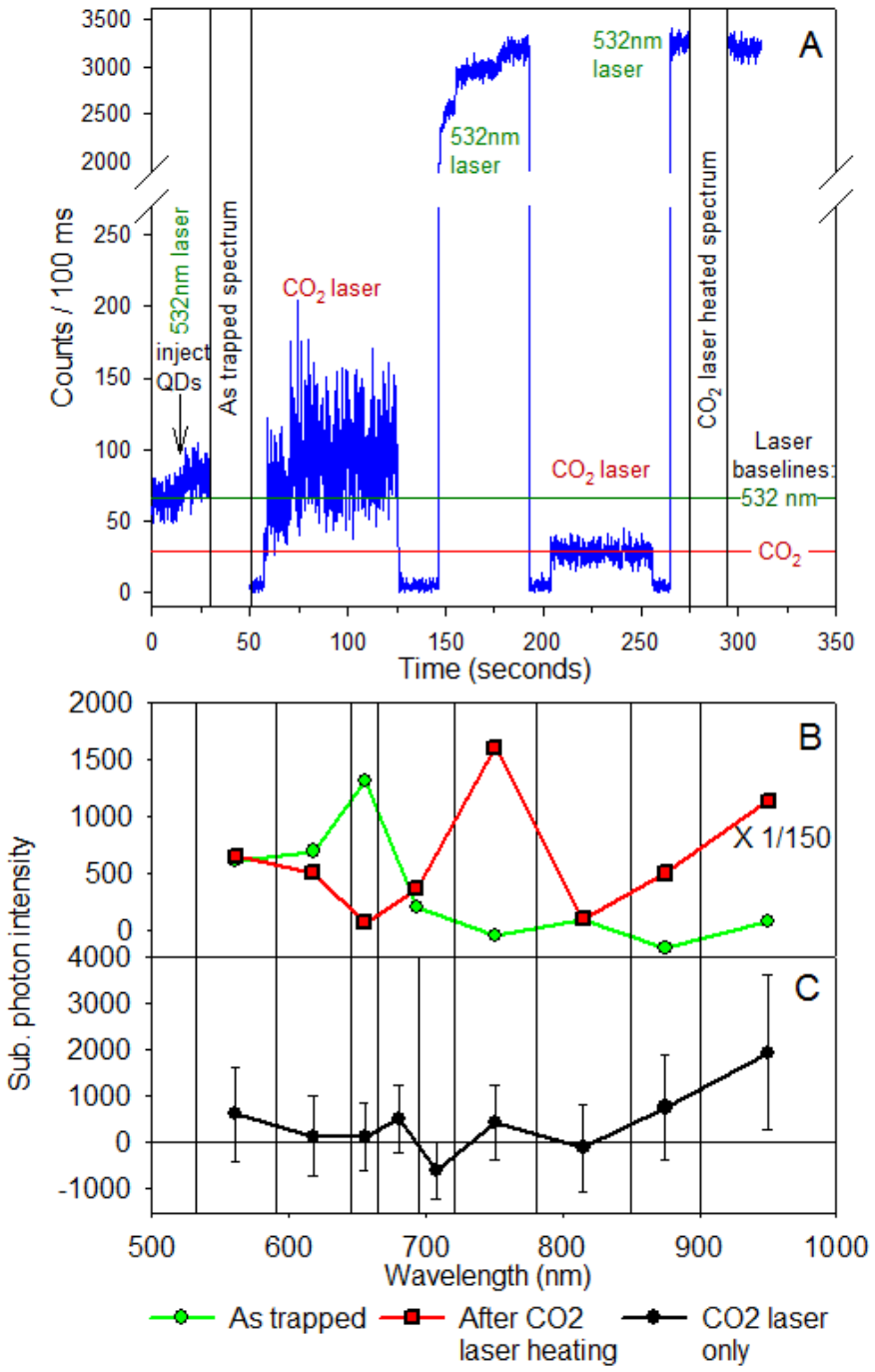

Figure 5.1. A: Photoluminescence of Trapped QDs as a Function of Alternating Exposure to Visible and Infrared Radiation. PL intensity from an ensemble of trapped QDs as a function of time. QDs are alternately exposed to 532 nm and 10.6μm light. B: emission spectra of the ensemble as trapped and after CO_2 laser exposure. C: Emission spectrum of a separate ensemble of the same QDs exposed only to the CO_2 laser.

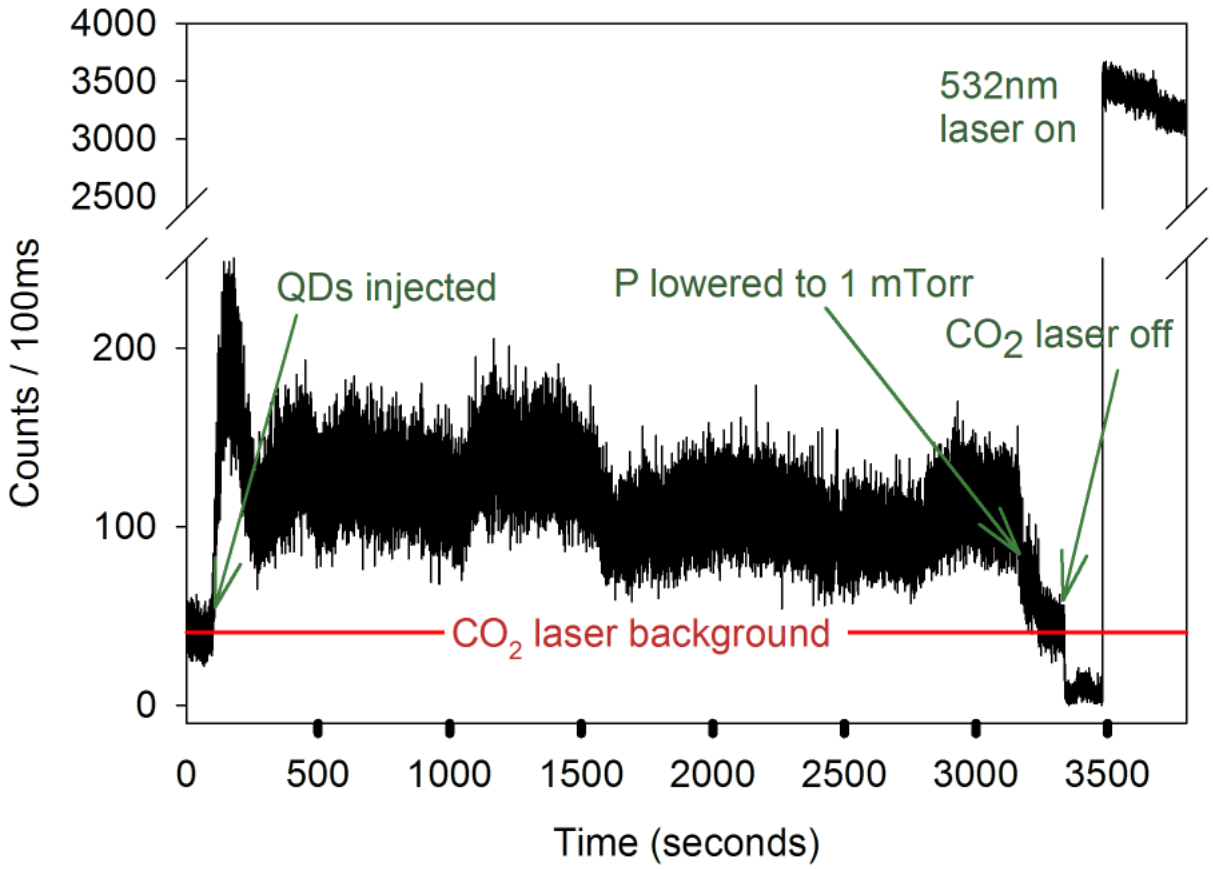

Figure 5.2. Emission From and Ensemble of QDs Pumped at 10.6 μm Radiation. Emission drops to zero when the pressure was lowered from 10 to 1 mTorr. Visible laser exposure confirms QDs were still in the trap.

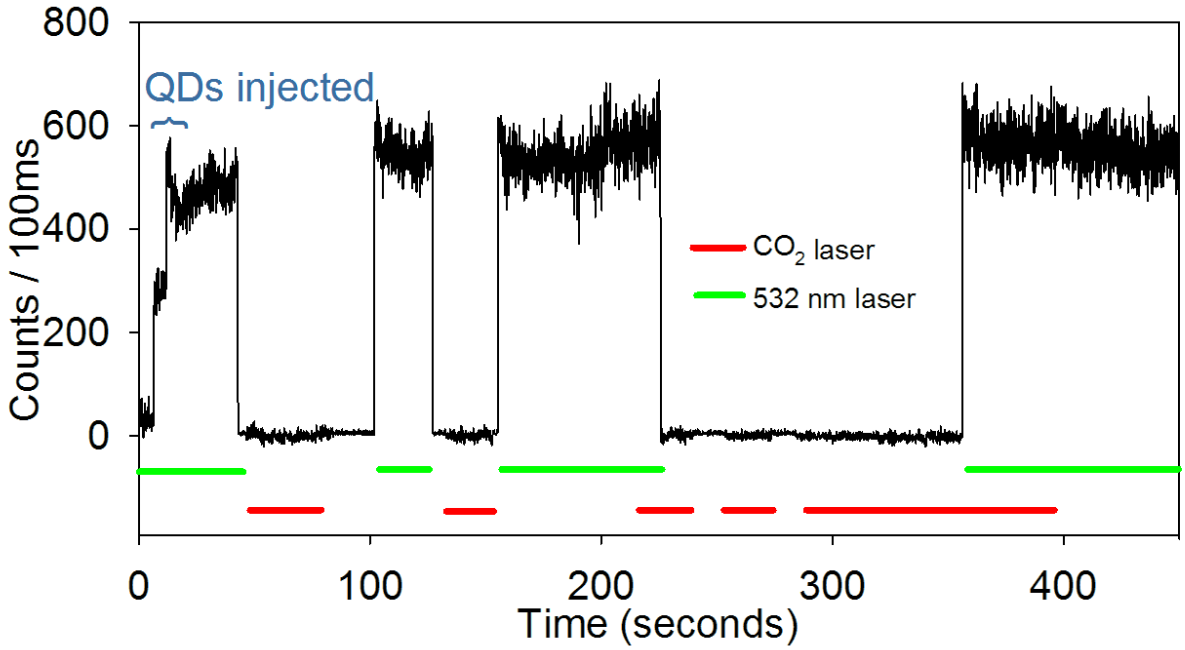

Figure 5.3. Emission From and Ensemble of QDs Exposed to Visible and IR Radiation. Emission intensity for a small ensemble of QDs exposed to various combinations of 532 nm and CO_2 laser irradiation, as described in the text. Both the CO_2 and 532 nm laser backgrounds have been subtracted out.

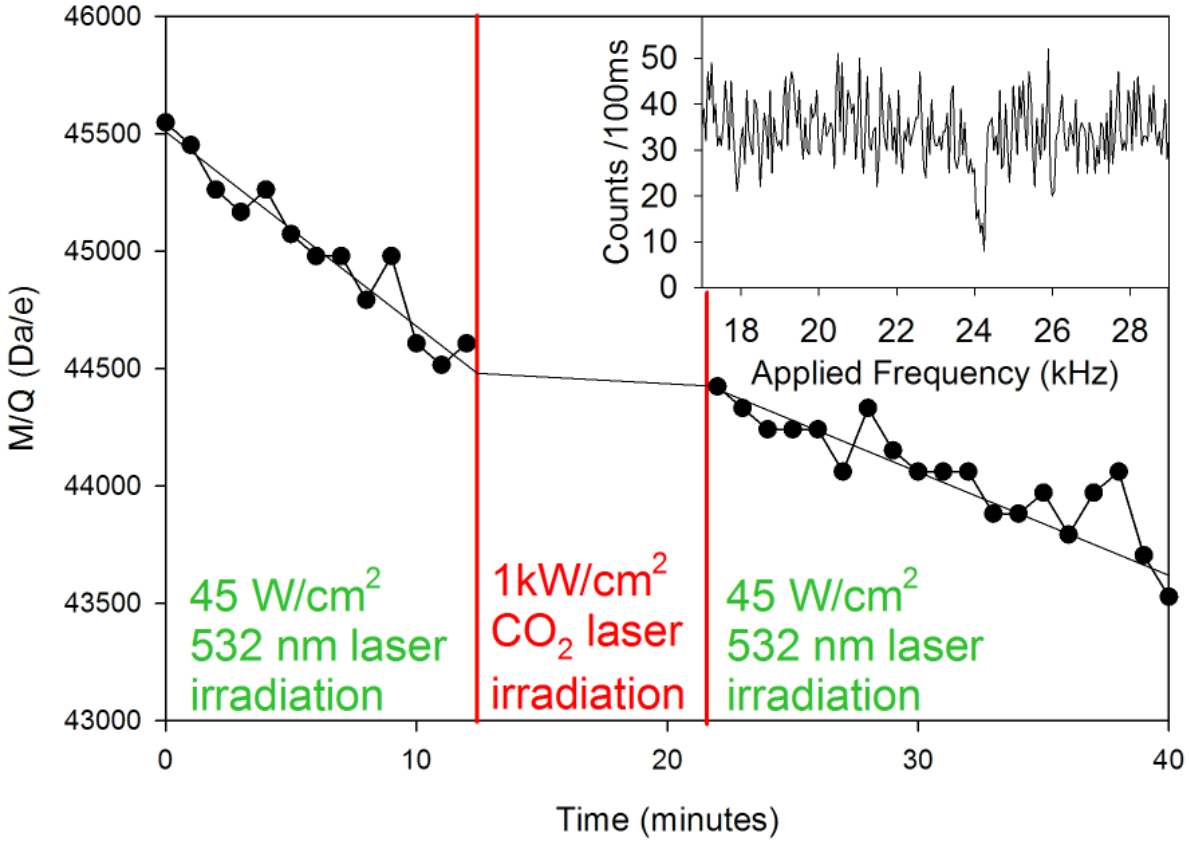

Figure 5.4. *M/Q* Measurements of a Single QD Before and After Exposure to High Intensity IR Radiation. *M/Q* measurements by frequency sweep of a single QD before and after CO_2 laser exposure shows that CO_2 laser does not change *M* or Q. A single frequency sweep is shown as inset.

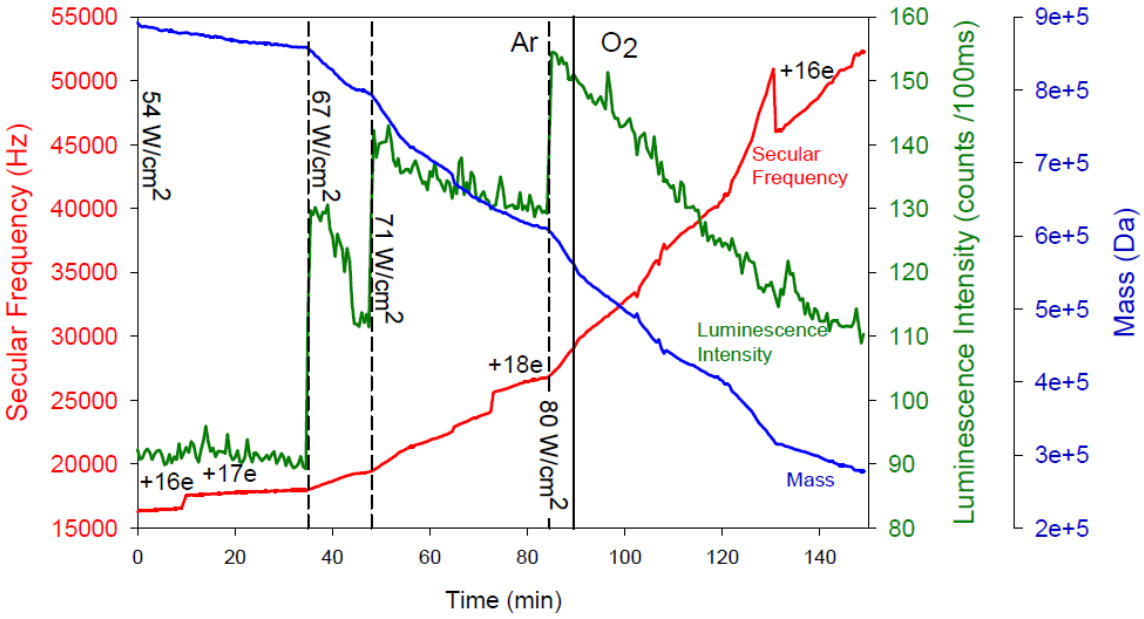

Figure 5.5. Photoluminescence of a Single QD Aggregate When Heated in Oxygen. A single particle composed of 7.5 nm nominal diameter CdSe/ZnS core/shell QDs was trapped and CO_2 laser heated in 5 mTorr argon. The initial mass was determined to be 892 kDa, indicating that the particle was either a monomer or a dimer. The initial 532 nm pump intensity was 54 W/cm^2, increased to vary the sublimation rate of the particle. Note that for constant laser intensity, the photoluminescence (PL) intensity generally decreased as the mass decreased. At 89 minutes the buffer gas was switched from argon to oxygen, resulting in a small decrease in the rate of mass loss, possibly due to better cooling from O_2, due to its additional degrees of freedom. From the perspective of use of QDs as probe particles, the important point is that the PL intensity remained high throughout the entire 2.5 h experiment.

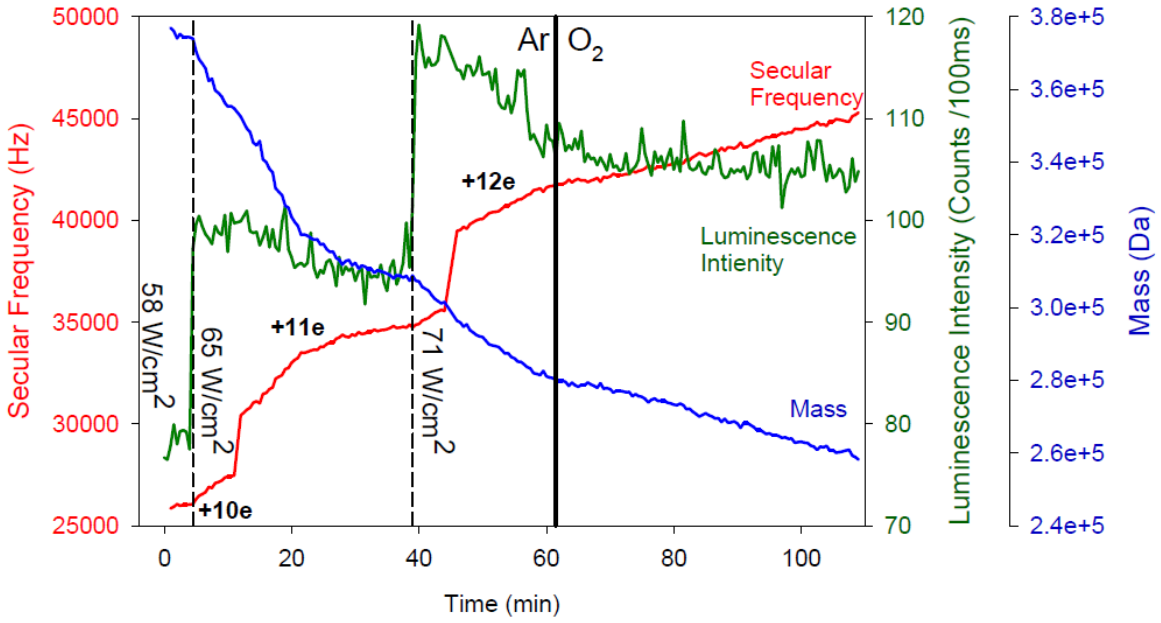

Figure 5.6. Photoluminescence of a Single QD Monomer When Heated in Oxygen. A single particle composed of 7.5 nm nominal diameter CdSe/ZnS core/shell QDs was trapped and CO_2 laser heated in 5 mTorr argon. Here, the particle had initial mass of only 377 kDa, and was therefore clearly a monomer, with mass near the low end of the stock QD size distribution. Again, while the PL intensity varied with pump laser intensity and generally declined as the particle sublimated, it remained high enough for use as a probe particle for the entire experimental time.

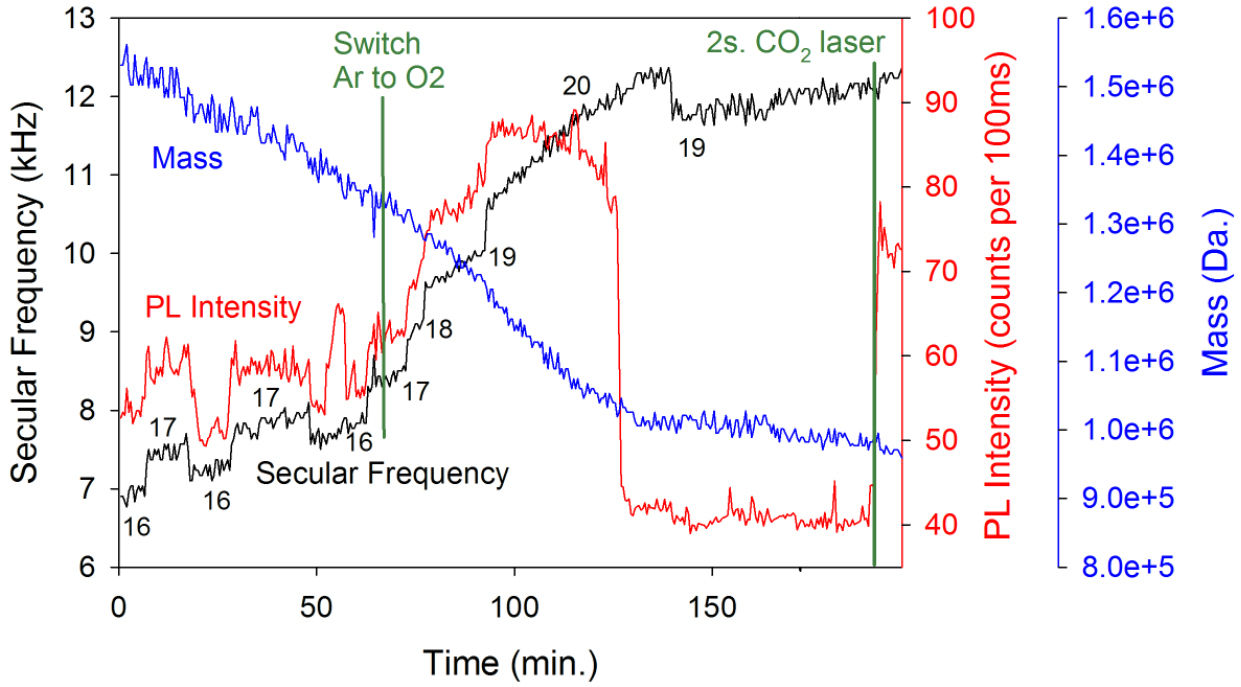

Figure 5.7. Photoluminescence of a Single QD Monomer When Heated in Oxygen. PL intensity, secular frequency, and mass for a single QD-based NP measured over 200 min, as the NP was heated and exposed to both inert and oxidizing environments.

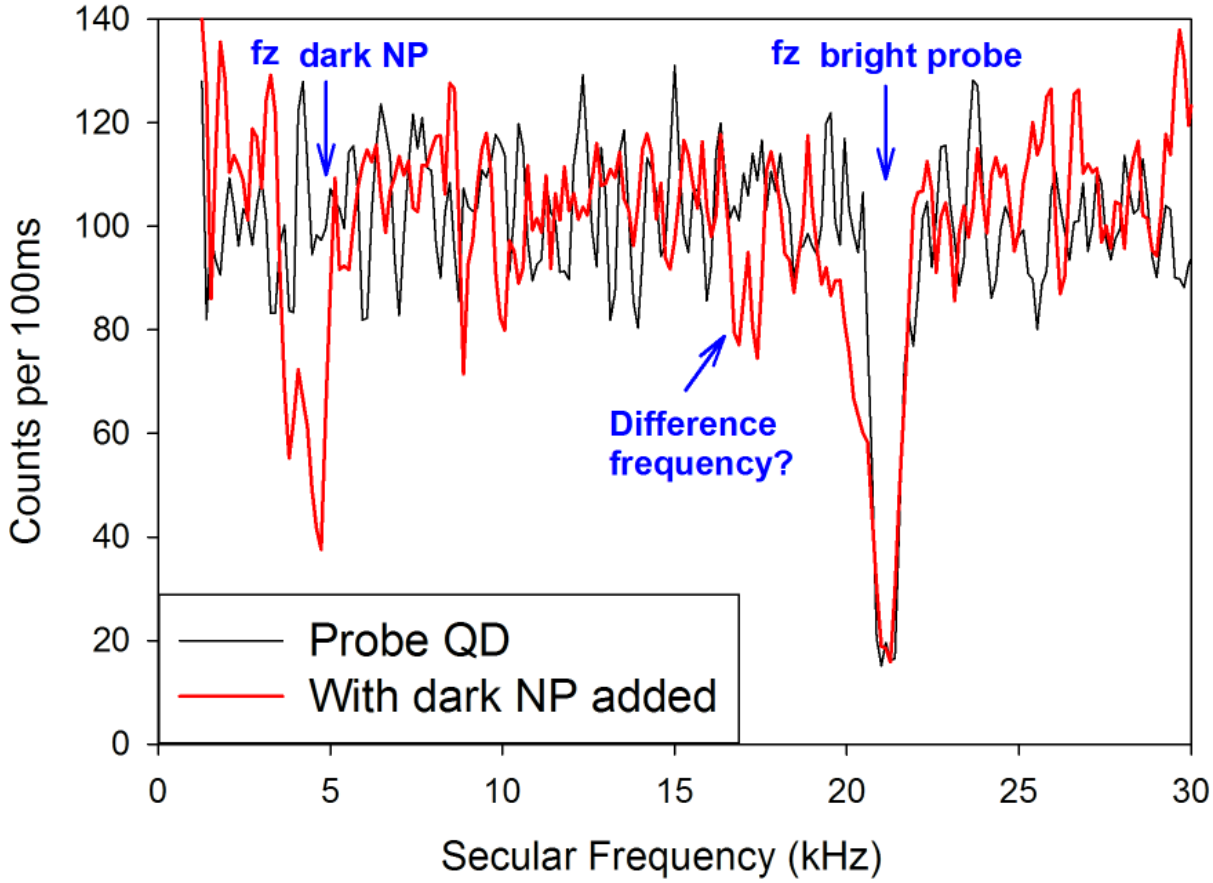

Figure 5.8. Noncontact Probe Detection of a Dark Nanoparticle.

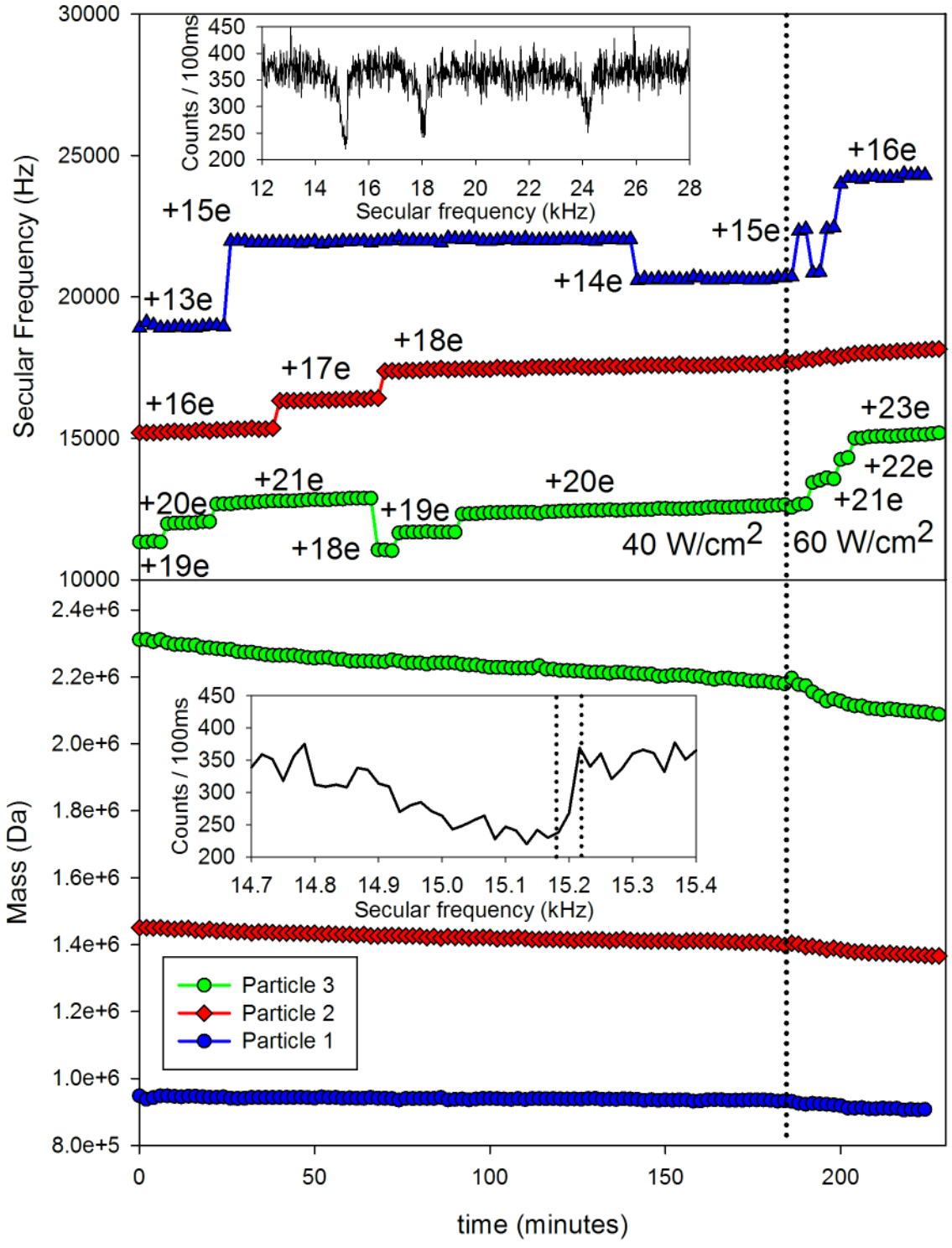

Figure 5.9. Simultaneous *M* and *Q* Determination for Three Cotrapped Nanoparticles. Top: Secular frequencies (f_z) for three cotrapped NPs, showing charge steps with charges shown. Top inset: Example raw f_z spectrum. Bottom: Mass vs. time for the three NPs at 40 W/cm^2 and 60 W/cm^2. Bottom inset: Shape of f_z resonance.

CHAPTER 6

ION TRAP NANOPARTICLE MASS SPECTROMETRY AS A PLATFORM FOR ULTRA-HIGH TEMPERATURE SURFACE CMEHISTRY

6.1 Introduction

One of the difficulties in studying NPs trapped in the gas phase by optical detection is controlling the temperature of NPs that absorb the pump wavelength. It is possible to heat NPs to sublimation temperatures even under fairly low laser power simply because there is no better heat sink than buffer gas in the milliTorr range. However, if the goal is to heat a particle to very high temperatures it is an advantage to levitate the particle in the gas phase. Under these conditions it is conceivable that any particle could be heated to sublimation using only a pump laser of only moderate power, provided the pressure is low enough, without damaging the ion trap.

For applications in hypersonic flight, materials that can resist temperatures in excess of 3000^{o} C may be needed.[1] There are only about 15 known materials with melting points above 3000^{o} C, including tungsten, rhenium, carbon, and several borides, carbides, nitrides, and oxides, but to be useful in an aerospace application the material must resist oxidation, be lightweight, and be fairly mechanically rugged. There are only a handful of materials that fit these qualifications. Where there is a healthy literature on the performance of these materials and their composites, especially ZrB_2/SiC materials,[1-7] little is known of their behavior above 2000 ^{o} C simply because it is challenging to study ultra-high temperature chemistry using conventional laboratory equipment. For example, K type thermocouples and conventional furnaces have an upper temperature limit of ~2000 ^{o} C. Lack of kinetic information above 2000 ^{o} C limits the design of next generation heat shield ceramics. The goal of this chapter is to present an experimental approach that can be used to study the surface reaction kinetics of ceramic materials in excess of 2000 K.

6.2 Ion Trap Ultra-High Temperature Approach

Our approach to this experiment is to trap a ceramic nanoparticle and detect it by thermal photon emission, analogous to blackbody radiation. Once trapped we can measure *M* and *Q* using the NPMS methods discussed in previous chapters, control T by changing the pressure and the pump laser intensity, measure an emission spectrum to estimate T, and monitor *M* as the particle is exposed to a reactant gas, such as O_2. In previous works[8, 9] we have demonstrated that it is possible to heat trapped NPs in a controlled manner, track changes in *M* as NPs sublime or react with gasses, and collect emission spectra from trapped NPs.

A proof of concept experiment is presented in Figure 6.1 where a graphite NP was trapped and detected by thermal emission while laser heating the particle in argon. Graphite was chosen because of its availability, high temperature stability, and it absorbs across the visible and IR. Thermal emission can be detected when pumping at 532 nm or at 10.6 μm. Radiation at 10.6 μm was used for the figure, but when the 532 nm pump is used scattered light is blocked using a 532 nm notch filter placed in the optical detection setup. We attempted to collect an emission spectrum from this particle while pumping at both wavelengths, but the emission intensity varied significantly over the course of a few minutes, making spectra impossible to collect by our long pass filter approach (see Chapter 4).

Without an emission spectrum it is impossible to estimate a particle temperature. Still, mass loss is temperature dependent, as is evident from the correlation between pump laser power and the rate of mass loss. While it is possible that mass loss is due to the sublimation of graphite, it is more likely that mass loss is due to desorption of water,

adventitious carbon, or other contaminants. Initially, the laser power density is 350 W/cm^2, and mass is stable. When the pump power is increased to 530 W/cm^2 the mass decreased at a rate of ~ 200 kDa/min. The rate of mass loss slowly decreases until the power was increased again to 700 W/cm^2. At this point the mass decrease, now 280 kDa/min, is accompanied by rapid charge increase, presumably due to thermionic emission. At 34 min the pump power was lowered back down to 530 W/cm^2, halting mass loss, until the power was set back to 700 W/cm^2, causing mass loss to resume. The rate of mass loss at a given pump power intensity decreases with time. By t = 50 min, the rate of mass loss was essentially zero, even though the pump power remained at 700 W/cm^2. The most obvious explanation for this behavior is that the rate of desorption of adventitious carbon and other surface contaminants decreases as the amount of material decreases. However, we also expect that the absorption cross-section of this NP will decrease as the particle diameter decreases. The initial mass of the NP is 94.5 MDa, and at t = 50 the mass has decreased to 50.0 MDa, corresponding to diameters of 37.5 and 30.4 nm, assuming a spherical particle. A 19% reduction in diameter may have a significant influence on the absorption cross section, and therefore, the temperature of the NP.

Another explanation is that as the *M/Q* ratio changed from 2.1 MDa/e to 8.8 MDa/e from the beginning to the end of the experiment the NP moved out of the hottest part of the pump laser focus. This seems reasonable in light of a pervious observation when working with trapped quantum dots where the luminescence intensity of a trapped quantum dot would sometimes decrease by ~25% when *M/Q* changed by 14%.[8] In that case, the luminescence intensity decrease was determined to be caused by the particle

moving out of the most intense part of the pump laser focus as *M/Q* changed, although no change in the rate of mass loss by sublimation was observed.

In future experiments it is essential to have a way to estimate the particle temperature. Subwavelength particles do not behave like blackbodies, but it may be possible to estimate the temperature from an emission spectrum. We propose to deposit a sample of the NPs on a temperature controlled stage outfitted with a thermocouple and record their emission spectrum in vacuum as a function of temperature up to 2000^{o} C. From this data we can extrapolate and predict what the emission spectrum for a single NP from that sample would look like above 2000^{o} C. Such emission spectra could be taken with our current Si APD optical detection setup, but it would be advantageous to have a detector whose cutoff wavelength extends beyond 1100 nm, the upper limit for Si APDs. We propose to use an InGaAs detector or similar, which are sensitive out to ~1700 nm.

6.3 References

1. E. Wuchina, E. Opila, M. Opeka, W. Fahrenholtz, and I. Talmy, Electrochem. Soc. Interface **16**, 30-36 (2007).
2. W. C. Tripp and H. C. Graham, J. Electrochem. Soc. **118**, 1195-1199 (1971).
3. E. V. Clougherty, R. L. Pober, and L. Kaufman, Trans. Met. Soc. AIME (Amer. Inst. Mining, Met., Petrol. Eng.) **242**, 1077-1082 (1968).
4. G. Zhao, X. Zhang, Z. Shen, D. Zhang, C. Hong, J. Li, and Z. Zhang, J. Amer. Ceram. Soc. **97**, 2360–2363 (2014).
5. F. Wang, L. Cheng, Y. Xie, J. Jian, and L. Zhang, J. Alloys Compd. **625**, 1-7 (2015).
6. R. E. Tressler, Composites A: Applied Science and Manufacturing **30**, 429–437 (1999).
7. E. Eakins, D. D. Jayaseelan, and W. E. Lee, Metall. Mater. Trans. A **42**, 878-887

(2011).

8. D. M. Bell, C. R. Howder, R. C. Johnson, and S. L. Anderson, ACS Nano **8** (3), 2387-2398 (2014).

9. C. R. Howder, B. A. Long, D. M. Bell, K. H. Furakawa, R. C. Johnson, Z. Fang, and S. L. Anderson, ACS Nano **8**, 12534-12548 (2014).

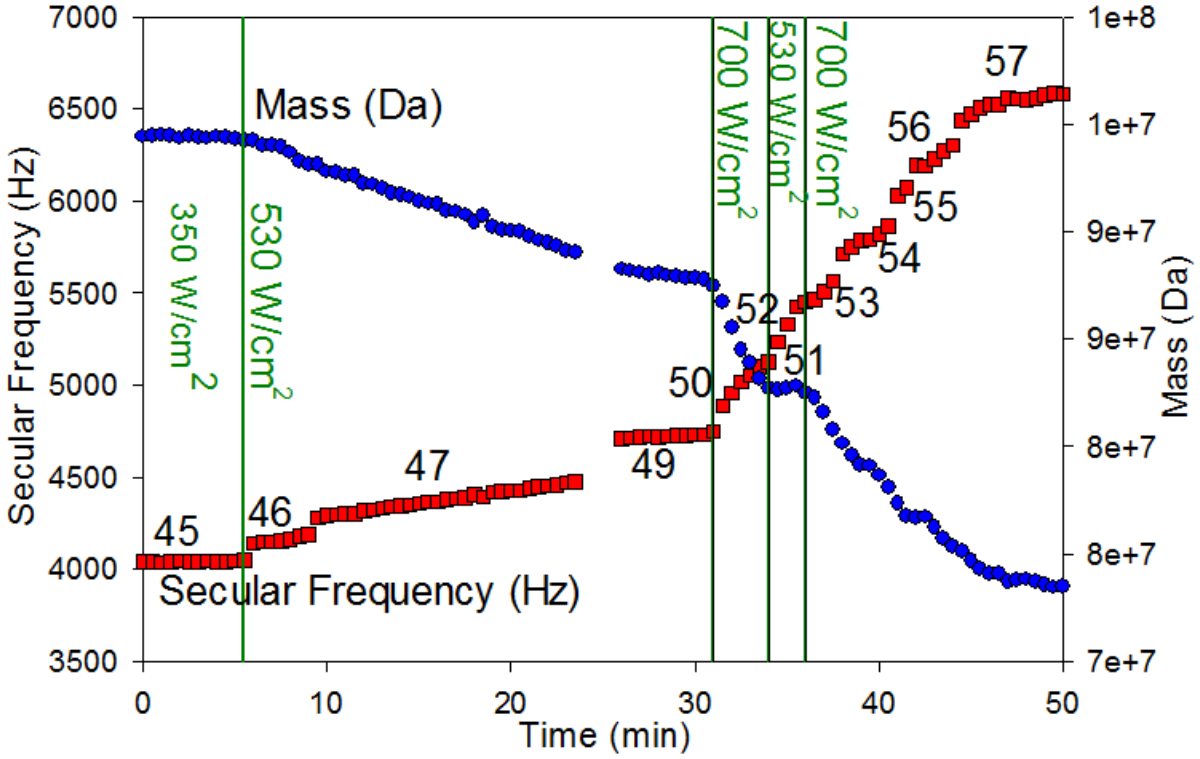

Figure 6.1 – Mass and Charge of a Graphite NP Detected by Thermal Photon Emission. The mass and charge of the particle are monitored as the particle is heated in argon by varying the power of the 532 nm pump laser.